Research Highlights

Investigating Shape-Memory Alloys and Composites with Neutron-Diffraction Techniques

R. Vaidyanathan (University of Central Florida), M.A.M. Bourke (MST Division), D.C. Dunand (Northwestern University)

As the name suggests, the shape-memory effect refers to a phenomenon wherein a material when mechanically deformed and then heated "remembers" and returns to its preset shape. Associated with this behavior is the superelastic/pseudoelastic effect whereby large and completely recoverable strains are generated (i.e., the strains are generated and recovered mechanically rather than thermally). Both of these effects are associated with "martensite" transformation, a first-order displacive transformation usually related to the hardening of steel. When a nickel-titanium (NiTi) shape-memory alloy is mechanically loaded, a stress-induced cubic (austenite) phase to monoclinic (martensite) phase transformation can result in macroscopic strains as high as 8%. On unloading, the martensite becomes unstable and transforms back to austenite with a concomitant macroscopic strain recovery. This phenomenon is called the superelastic/pseudoelastic effect and finds application in, for example, mobile phone antennae, cardiovascular stents, and guidewires.[1] By recording neutron-diffraction spectra during external loading, we can investigate this reversible stress-induced austenite-to-martensite transformation in situ. Such data can provide quantitative phase-specific information on the elastic strain, texture, and volume-fraction evolution. The basic principle of such measurements for strain determination involves using the lattice-plane spacing of grains within the crystal structure as internal strain gauges. For texture, the relative intensities of the diffraction peaks are considered and for phase volume fraction, an integrated intensity of peaks corresponding to a specific phase is used.

Investigating Superelasticity in NiTi and NiTi-TiC

We summarize and synthesize here a systematic study[2,3] of superelasticity in NiTi subjected to monotonic and cyclic loading and in NiTi-TiC subjected to monotonic, quasi-static loading by the simultaneous acquisition of neutron-diffraction spectra in both samples. The advantage of using neutrons over x-rays is that the bulk behavior can be investigated in polycrystalline samples (i.e., the 50% transmission thickness in NiTi for Cu-K_α x-rays is approximately 9 μm as compared to about 3 cm for thermal neutrons). The spectra were recorded while interrupting the loading and unloading parts of the cycle at the stresses shown in Figs. 2 through 4. The diffraction experiments allowed for the micostructural texture, phase-volume-fraction, and strain changes that were produced during the stress-induced austenite to martensite transformation to be compared to the macroscopic stress-strain response.

Our neutron-diffraction measurements were performed with the Neutron Powder Diffractometer at the Lujan Neutron Scattering Center (Lujan Center) at the Los Alamos Neutron Science Center (LANSCE) (Fig. 1).
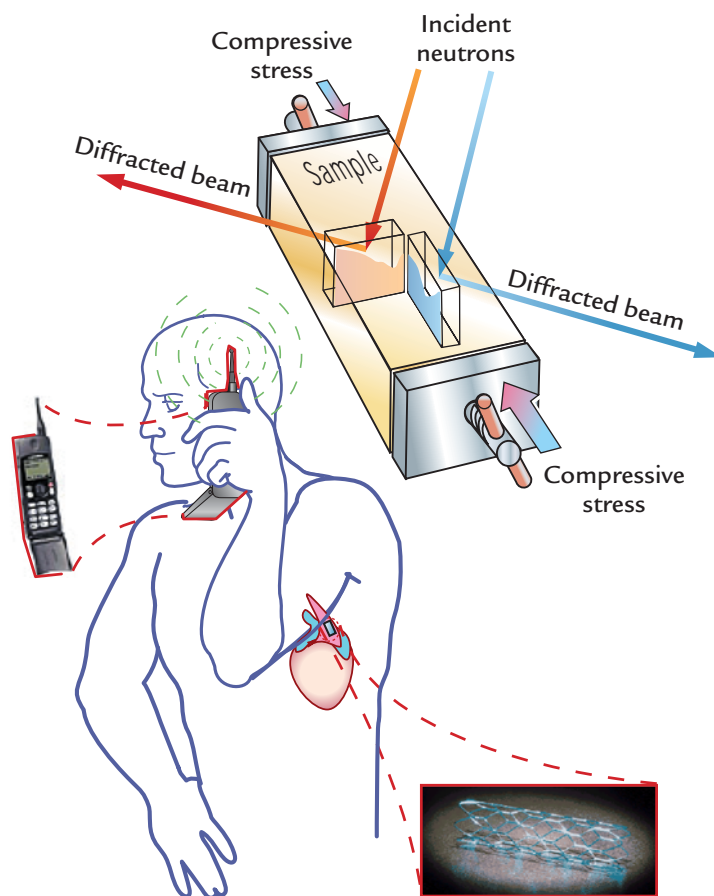
↑ Fig. 1. *Schematic of the experimental setup at the Lujan Center at LANSCE, showing the incident neutron beam and two of the three diffracted beams with respect to the loading direction. The irradiation volume is about 1 cm³. The setup was used to study superelastic NiTi, which is used in vascular stents in the human body and in the flexible antennae of mobile telephones. The strain induced by the compressive stress is measured along the scattering vector, which is either parallel to the load axis (i.e., the diffracted beam in red) or perpendicular to the load axis (i.e., the diffracted beam in blue).*

Three series of experiments[2,3] on hot isostatically processed samples were performed:

(1) uniaxial compressive loading of NiTi up to 975 MPa and subsequent unloading (Fig. 2),
(2) cyclic compressive loading and unloading (100 cycles) of NiTi up to 975 MPa (Fig. 3), and
(3) uniaxial compressive loading of NiTi-TiC up to 975 MPa and subsequent unloading (Fig. 2).

Samples were loaded in compression while neutron-diffraction spectra were simultaneously acquired at three diffraction angles. The loading axis formed an angle of 45° with the incident polychromatic neutron beam, allowing measurements for which the scattering vector was parallel and perpendicular to the loading axis. A third detector was used in backscattering geometry. An extensometer (i.e., a devise that measures the change in length of a sample subjected to different loads) was attached to the samples to record macroscopic strain during the experiments. The Rietveld refinement technique, implemented in the Los Alamos National Laboratory code General Structure Analysis System (GSAS),[4] was used to analyze the neutron-diffraction spectra. In the Rietveld method, the diffraction intensity at every point in the spectrum was determined by adding the calculated background and Bragg scattering intensities corresponding to diffraction peaks. The refinement procedure varied selected parameters (e.g., phase volume fractions, atom positions, and phase texture) until the calculated and measured spectra matched in a least-squares fit. In particular, the procedure incorporated changes in diffraction peak intensities due to texture. A generalized spherical-harmonic-texture description was used to account for the evolving texture from the austenite to martensite phase transformation.

In Situ Observation of Microstructural Changes During Transformation

The generalized spherical-harmonic-texture formulation in Rietveld refinements helped us determine the volume fractions of the austenite and martensite phases that coexisted under an applied stress in NiTi and NiTi-TiC. We observed a linear relationship between the volume of
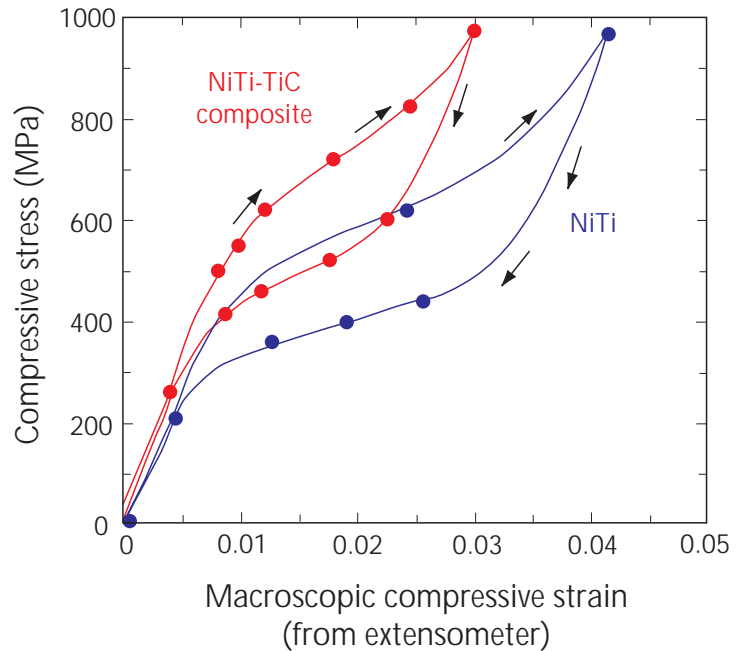
↑ Fig. 2. *Representative macroscopic compressive stress-strain responses of superelastic NiTi and NiTi-TiC samples during loading and unloading, which were tested in the neutron beam. The symbols on the curves indicated the stresses at which loading was interrupted and neutron-diffraction spectra recorded.*
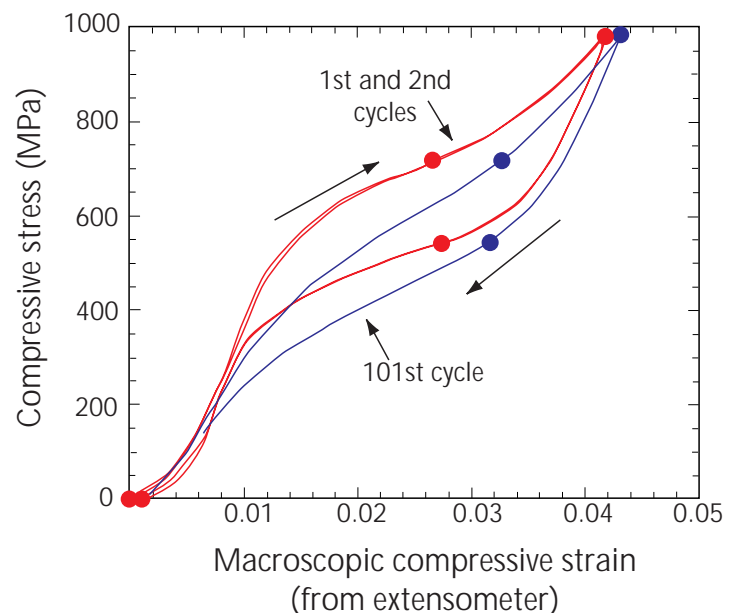
↑ Fig. 3. *Representative macroscopic compressive stress-strain response of a superelastic NiTi sample during cyclic loading. The symbols on the curves indicate the stresses at which loading was interrupted and neutron-diffraction spectra were recorded.*

stress-induced martensite and the macroscopic strain generated by the transformation for both NiTi and NiTi-TiC. Both the volume fraction of martensite, which formed at any given applied stress, and the recoverable strain decreased in the presence of TiC particles. This is understandable given that the most favorable variant, in terms of the macroscopic strain, may not be compatible with a non-transforming TiC particle in its proximity and may thus not form.

In the NiTi and NiTi-TiC samples, the overall texture (i.e., preferred orientation of grains) of the martensite decreased with increasing stress. This finding was attributed to favorable orientations of austenite transforming first to martensite and the need for the newly formed martensite to be compatible with the already transformed martensite (and TiC). Upon comparing the texture of martensite formed in the presence and absence of TiC at the same superelastic strain, we discovered that martensite in the presence of TiC was less textured. This is understandable since there are more spatial constraints for the formation of martensite when TiC is present. This situation is analogous to martensite forming at lower strains (where fewer constraints exist) being more textured than the martensite forming at higher stresses (where other martensite plates preclude certain orientations).

Significant discrepancies were observed between the Young's moduli (i.e., the linear relationship between stress and strain in the initial part of the stress-strain curve) for NiTi and NiTi-TiC measured with an extensometer and predictions using single-crystal data and the Eshelby elastic theory.[5] The differences were attributed to small amounts of austenite transforming to martensite at low stresses, which reduce the apparent Young's moduli. In contrast to the above macroscopic data, the modulus of austenite in NiTi measured by neutron diffraction (from the slope of applied stress versus elastic strain response) compared well to moduli predicted using single-crystal data. The applied stress at which austenite transforms to martensite and back to austenite increased in the presence of TiC particles. For both NiTi and NiTi-TiC, the elastic lattice strain in the austenite remained linear with respect to the applied stress even when significant volume fractions of austenite had transformed to martensite, but showed some nonlinearity at higher applied stress. This load transfer coupled with the stress hysteresis results in strains in the austenite during unloading being somewhat larger than strains during loading for the same stress. For the NiTi-TiC composite, we observed good agreement in the phase strains predicted by the Eshelby elastic theory and those measured with neutron diffraction. In general, the self-accommodating nature of

the stress-induced martensite almost eliminated the mismatch with the TiC particles and the transforming austenite. Additional anisotropy introduced by strain redistribution caused by the transformation was reflected in changes in the anisotropic component of the strain of the austenite phase in NiTi-TiC.

For the case of cyclic loading, the change in macroscopic stress-strain behavior at intermediate stresses where martensite and austenite coexist was found to result from an increase in both volume fraction and texture in the stress-induced martensite. The average elastic strain in austenite remained mostly unchanged at intermediate stresses, but the isotropic and anisotropic components of the strain in austenite redistributed themselves. The residual elastic strain present after unloading in austenite also evolved during cycling. These phenomenological observations shed light on the materials evolution occurring during repeated reversible stress-induced transformation in superelastic NiTi, which is important both during mechanical training (i.e., process of stabilization prior to actual use) of NiTi devices and during their subsequent use.

Ongoing Work

The martensite phase in NiTi consists of 24 "variants" with varying crystallographic orientations and can deform by twinning, producing macroscopic tensile strains as high as 8%. (Twinning is an imperfection in polycrystals involving the intergrowth of two or more polycrystal grains so that each grain in a twinned system is a reflected image of its neighbor. In essence, twinning is a special type of grain boundary defect where a polycrystal grain is joined to its mirror image.) Heating results in a phase transformation to the austenite phase and recovery of all the macroscopic strain accumulated by twinning, a phenomenon known as shape-memory. Due to their ability to work against large forces during this strain recovery, shape-memory alloys are widely used as actuators in engineering applications. In 2001, we performed *in situ* neutron diffraction during tensile and compressive loading of shape-memory martensitic NiTi. Our objective was to follow deformation twinning as a function of the applied external load and to relate the texture and internal strain evolution (from diffraction data) with macroscopic strain data (obtained from an extensometer). Fig. 4 shows the typical stress-strain response of shape-memory NiTi. The various numbers indicate the stress levels at which loading was interrupted and neutron-diffraction spectra obtained. A holding period of about 6 hours was used at each stress level. Numbers 1 and 2 represent elastic loading, 3 and 4 represent twinning deformation, and 5 and 6 represent elastic
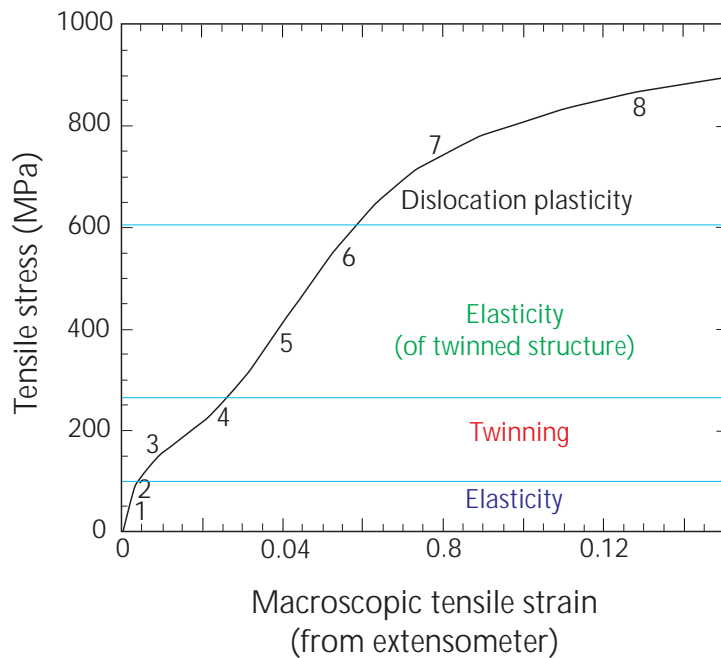
↑ **Fig. 4.** *Tensile stress-strain curve of shape-memory NiTi. The numbers indicate the stress levels at which loading was interrupted and neutron-diffraction spectra were obtained. The associated dominant deformation mechanisms are also indicated.*

deformation of the twinned martensite. This is followed by yielding due to dislocation plasticity and strain-hardening (7 and 8). Because of the asymmetric nature of the stress-strain curve with respect to tension and compression, we performed two series of experiments using compressive and tensile loads. We do not fully understand the deformation mechanisms indicated in Fig. 4, and a comprehensive thermomechanical model describing constitutive behavior (i.e., the material response to stress and strain) is still unavailable. The ability to follow the texture and strain evolution during these stages and examine the micromechanical and microstructural changes using neutrons will therefore be of significant scientific and engineering interest. The results obtained at LANSCE are currently being evaluated using the methodology developed in Reference 6.

References

1. *Shape Memory Materials*, K. Otsuka and C.M. Wayman, Eds. (Cambridge University Press, Cambridge, 1998).
2. R. Vaidyanathan, M.A.M. Bourke, and D.C. Dunand, "Phase Fraction, Texture and Strain Evolution in Superelastic NiTi and NiTi-TiC Composites Investigated by Neutron Diffraction," *Acta Materialia* **47** (12), 3353 (1999).
3. R. Vaidyanathan, M.A.M. Bourke, and D.C. Dunand, "Texture, Strain and Phase Fraction Measurements During Mechanical Cycling in Superelastic NiTi," *Metallurgical and Materials Transactions A* **32**, 777 (2001).
4. A.C. Larson and R.B. Von Dreele, "General Structure Analysis System (GSAS)," Los Alamos National Laboratory report LAUR-8-748 (1986).
5. T.W. Clyne and P.J. Withers, *An Introduction to Metal Matrix Composites* (Cambridge University Press, Cambridge, 1993).
6. R. Vaidyanathan, M.A.M. Bourke, and D.C. Dunand, "Analysis of Neutron Diffraction Spectra Acquired *In Situ* During Stress-Induced Transformations in Superelastic NiTi," *Journal of Applied Physics* **86** (6), 3020 (1999).

## Diffuse Scattering in Powder Diffraction from the Delta Phase of Plutonium

A.C. Lawson (MST Division), J.A. Roberts, R.B. Von Dreele (LANSCE Division), B. Martinez, R.I. Sheldon (NMT Division)

In powder-diffraction measurements made by elastic scattering of thermal neutrons, diffuse scattering shows up as a weak, oscillating component in the scattering data. For years, we observed such diffuse scattering from plutonium (Pu) and its alloys, but we did not know how to analyze it. This analysis is important for any material to account for all scattering, and it is especially important for Pu because of its role in the nuclear weapons program. We used neutron powder diffraction at Los Alamos Neutron Science Center (LANSCE) to help us discover the cause of diffuse scattering in our experiments. We analyzed the data with tools recently incorporated into the General Structure Analysis System (GSAS)—a powder-diffraction data-analysis package used to refine and determine crystal structure. We found that the observed diffuse scattering comes from lattice vibrations (not from some other exotic mechanism) and is quite an ordinary, non-Pu-specific phenomenon.

Data and Interpretation

Fig. 1 shows a neutron-diffraction pattern from a mostly ^{242}Pu sample taken at room temperature on the Neutron Powder Diffractometer (NPD) at LANSCE. The Pu sample was alloyed with 2% gallium (Ga) atoms, which stabilizes its delta (δ) phase to low temperatures. The sharp peaks in the intensity of scattered neutrons are produced by Bragg reflection of neutrons by the regular planes of the crystal lattice. They reveal the crystal structure of the alloyed Pu sample: a simple face-centered-cubic (fcc) lattice resulting from the close packing of Pu and Ga atoms. The information required to specify this structure (or any other structure) includes the peak positions, or "d-spacings," and the intensities, or "peak-heights," of the reflections. The scattered neutron intensity is shown in red. Verification of the fcc structure of δ-phase Pu is accomplished by fitting the observed data to a computer model of the fcc structure using Rietveld refinement. The intensities predicted by the model are shown in green.

The Rietveld model requires specifications of crystal structure, peak widths, and the vibrational amplitude of the atoms (which affect the peak height). The vibrational amplitude of the atoms depends on the temperature, mass, and the Debye temperature, which is the property of crystals that characterizes the elastic stiffness of their structures.[1-3] The sample is surrounded by a containment vessel constructed from vanadium to prevent radiological contamination of equipment and experimenters. Vanadium contributes a rather high constant background but only a few tiny peaks on the diffraction pattern. There is another subtler signal in these diffraction patterns: a weak "wiggly" signal known as diffuse scattering. The cause of this diffuse scattering was unknown when we first observed it, but we have now identified it as "temperature diffuse scattering," or TDS.[4] TDS is caused by the coupling of the vibrations of individual atoms to form sound waves, or phonons. These waves break the strict periodic crystallographic symmetry of the material, so that a fraction of the Bragg intensity is transferred to an undulatory
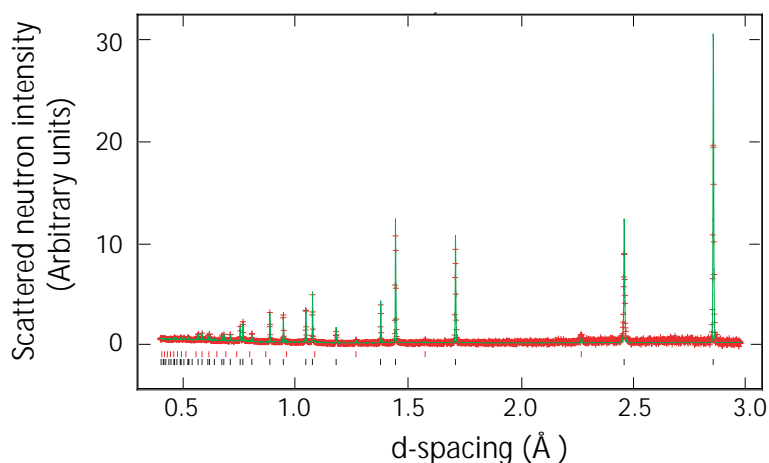
↑ Fig. 1. *Neutron-diffraction data for a Pu sample alloyed with 2% Ga atoms to stabilize its δ-phase. Crystal structures are determined by scattering experiments using a portion of the crystal as the target. Neutrons impinge on the target and on impact scatter from the crystal planes, ricocheting in various directions. Measuring the scattered particles provides raw data that are then computer processed to give a picture of the atomic arrangements. The positions of the atoms are then inferred from the computer-analyzed data. These data were taken on the NPD at LANSCE. The graph shows the scattered neutron intensity plotted against crystal lattice d-spacing, which is closely related to neutron wavelength. The data have been fit to a crystal model using Rietveld analysis. The red points are the data and the green line is the pattern calculated from an fcc crystal model. The black tick marks indicate Bragg reflections of δ-phase Pu, and the red ones indicate reflections of the vanadium radiological containment surrounding the Pu sample.*

pattern known as diffuse scattering. If the vibrational coupling were not present, the background would be perfectly flat. The diffuse scattering signal is proportional to the correlation of the atomic vibrations—that is, the influence that the vibration of one atom has on the vibrations of others in a crystal lattice.

Debye first exploited the role of diffuse scattering in x-ray diffraction from materials in 1930,[5] when he and Menke showed that the diffraction pattern of liquid mercury could be explained as a series of simple oscillatory terms of the form

$$S_{Debye}(k,R) = \frac{\sin(kR)}{kR} ,$$

where k is the wave vector of the scattered x-ray. (This is true for neutrons, too, but neutron diffraction had not been invented yet; in fact, the neutron had not even been discovered until two years later in 1932!) Each term $S_{Debye}(k,R)$ represents a tendency for atoms to be separated by a distance R. This tendency, called a "correlation," is a compromise reached collectively by the atoms as they balance their response to the attractive interatomic forces with the necessity of staying out of each other's way. $S_{Debye}(k,R)$ is the scattering as a function of wave vector produced by the correlation of atoms at distance R. The scattering from a liquid is a sum of such terms, one for each interatomic distance R that is characteristic of the liquid structure. The diffuse scattering found in Pu differs from that found in a liquid: it arises from the coupling of atomic vibrations into waves. The diffuse scattering from vibrational correlation can be distinguished from the diffuse scattering of atomic correlations by an extra factor of k^2 that multiplies the scattering terms S_{Debye}. We were thus able to associate the diffuse scattering actually observed in Pu with vibrations rather than with more liquid-like effects, such as a hypothetical ordering of vacancies at high temperatures.

Like scattering in a liquid, the observed vibrational scattering in Pu is a sum of components associated with various values of R derived from the crystal structure. Because the scattering functions are known, the amplitudes of these components can be determined directly from the neutron-diffraction pattern using Rietveld analysis, which is how we fit the backgrounds of Figs. 1 and 2. We were able to show that the vibrational amplitudes of these various components increase strongly with temperature in a roughly linear fashion for the alloyed Pu sample.[6]

A satisfactory account of the behavior of the vibrational scattering can be derived from the Debye continuum
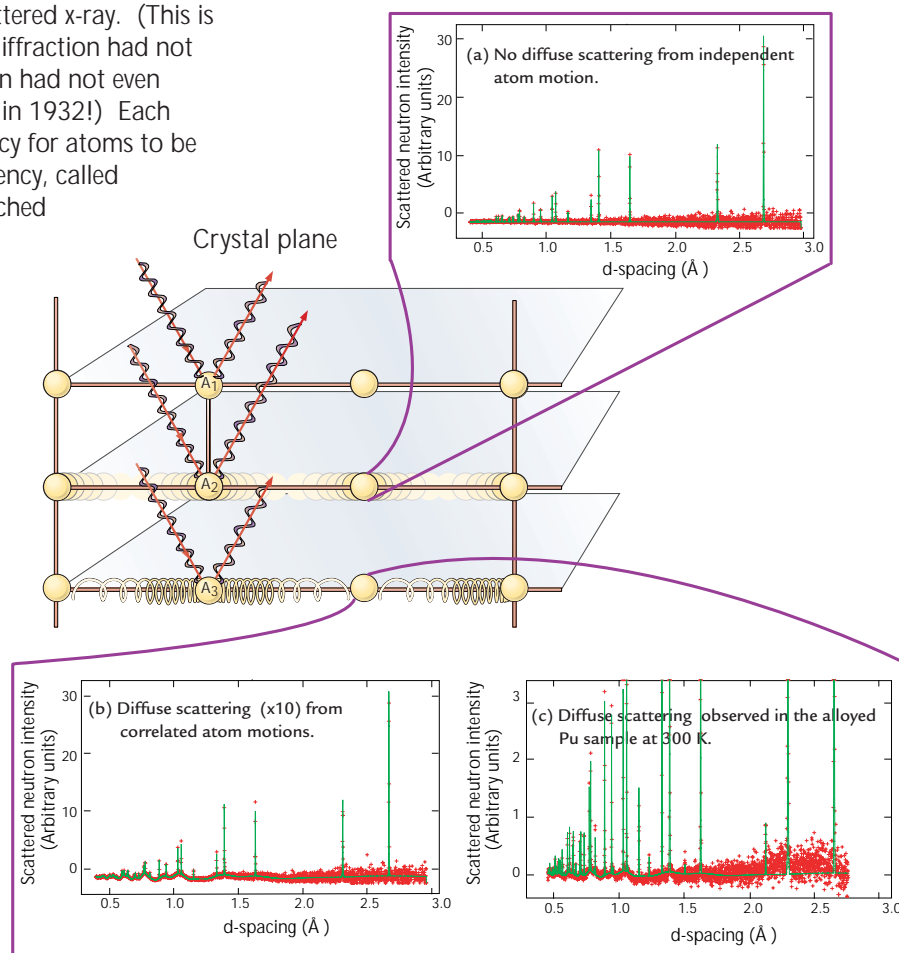
Fig. 2. *Diffraction pattern for the alloyed Pu sample at room temperature. Vibrational diffuse scattering is caused by the coupling of the vibrations of independent atoms. If the vibrations are independent, as shown in the middle row of atoms, then there is no diffuse scattering, and the diffraction pattern appears as in panel **a**. Diffuse scattering caused by coupling vibrations according to the Debye model, as shown in the lower row of atoms, appears in the background of panel **b**, when the amplitude is artificially increased by a factor of 10, but the diffraction peaks remain the same. The actual observed diffuse scattering is shown in panel **c**, where the intensity scale has been enlarged by a factor of 10 for comparison with panel **b**.*
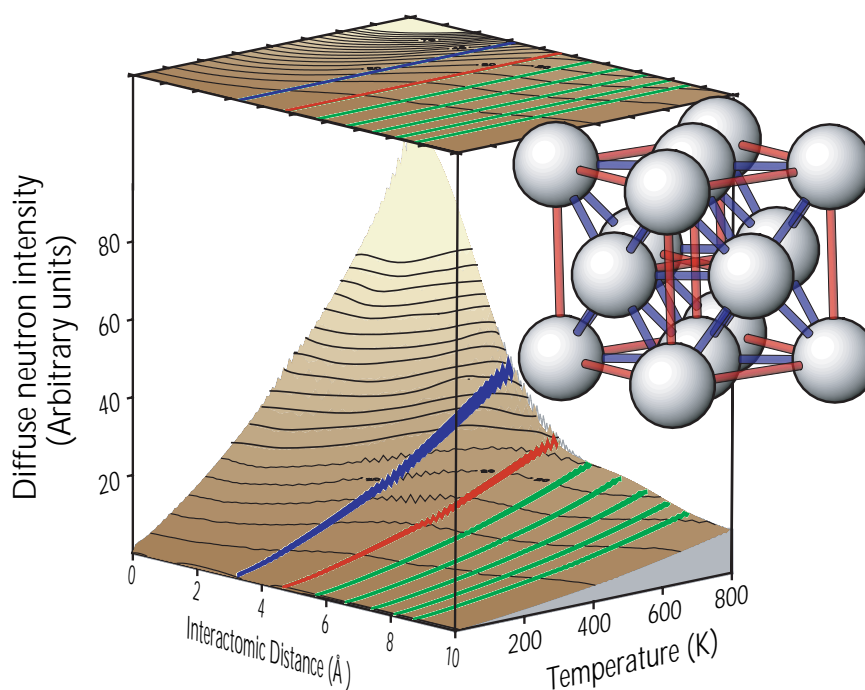
model of a solid that treats the crystal as a continuous elastic medium, much like Jell-O™. In an actual material, the distance between atoms is not continuous, but discrete, as determined by the crystal structure. In a sense, the Debye model is a spatial average of the crystal structure. As explained in Warren's book,[4] the temperature-dependent amplitude of diffuse scattering associated with interatomic distance R is proportional to the vibrational correlation at that distance, and it depends only on the strengths of the interatomic forces that hold the structure together. Only specific values of R are relevant—that is, those determined by the actual crystal structure of the solid. The signal for Pu is larger than that observed for most materials because of its weak interatomic forces. The expected signal is shown in Fig. 3, and the measured results[6] for the alloyed Pu sample are in agreement with this expectation.

For a while some people thought[7] that measurement of the diffuse scattering would suffice to determine the complete vibrational spectrum of the solid. Some effort was expended to obtain such data for δ-phase Pu via a new technique based on the established pair distribution function (PDF),[8] which is a mathematical function that predicts the probability that two atoms will be at a certain distance from each other. This would have been an important advance because the vibrational spectrum contains much more information that is usually obtained from diffraction experiments (like ours) made on polycrystalline samples, and measurement of the vibrational spectrum traditionally requires the growth of a large single crystal. Extraction of the vibrational spectrum failed for three reasons.[9] Most importantly, although the model of a Debye solid satisfactorily explains most of the powder-averaged signal in our experiments, this signal contains information about the continuum aspects (Debye model) of the solid, not the dynamics of the discrete lattice itself. Second, the PDF method does not (and cannot) include corrections for

significant lattice dynamic effects in the analysis.[10] Finally, the PDF method advocated by Dimitrov *et al.*[7] requires that the diffraction pattern be processed by Fourier transformation to obtain the PDF before subsequent analysis. (Fourier transformation is a mathematical operation that sorts the diffraction pattern according to the rapidity of the "wiggles" that comprise it.) As it happens, the ^{242}Pu available for these experiments contains ^{239}Pu impurities that contribute a neutron-absorption dip to the diffraction pattern. (We used ^{242}Pu precisely to avoid this resonance!) It is off scale in Figs. 1 and 2, but it is shown in detail in Fig. 4. The shape of this resonance can be modeled, but the accompanying attenuation introduces an unacceptable level of noise into the Fourier transform. Even if the resonance problem could be solved, the limitations imposed by the first two issues would be insurmountable.

Conclusion

The conclusion drawn from this powder-diffraction experiment is that δ-phase Pu is a Debye solid. As far as

↑ Fig. 3. *The dependence of the intensity of the diffuse scattering on interatomic distance and temperature is shown in this three-dimensional plot. This plot is based on the Debye model of a solid that treats the crystal as a continuous elastic medium, much like Jell-O™. In an actual material, the distance between atoms is not continuous but discrete as determined by the crystal structure. The nearest-neighbor interatomic distance is shown in blue, the next nearest-neighbor distance is shown in red, and successive near-neighbor distances are shown in green. The first two interatomic distances (the blue and red) are indicated also in the inset, which shows the crystal structure. The diffuse scattering increases strongly with temperature.*
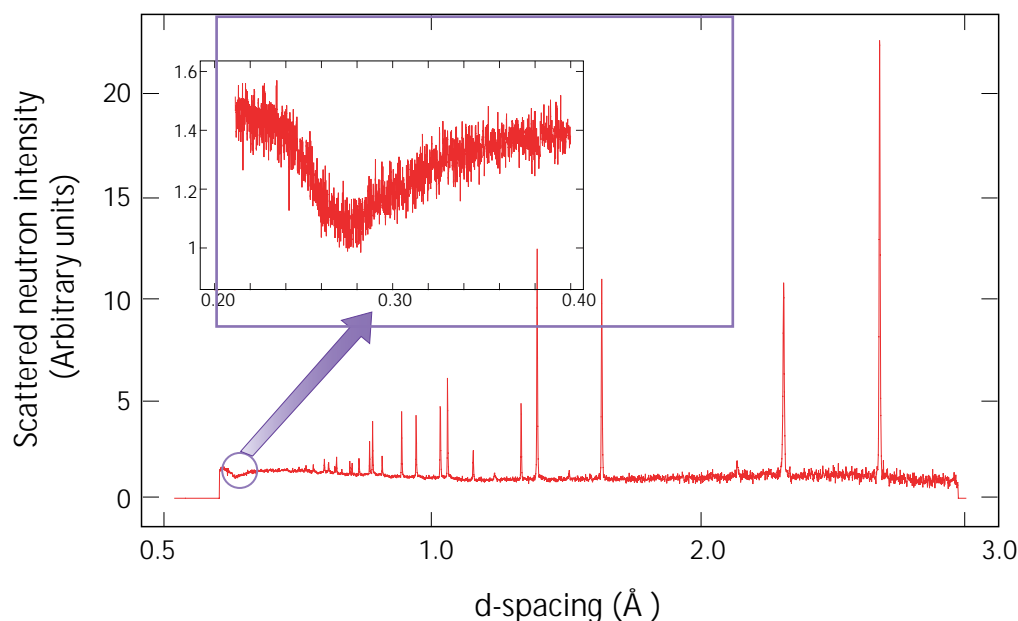
↑ Fig. 4. *The effect of a nuclear-absorption resonance, mostly from isotopic impurities of ^{239}Pu in a sample that is primarily ^{242}Pu, is clearly evident in the dip observed at the lowest d-spacings. This resonance has nothing to do with the material properties of Pu; it is just a extraneous effect that discourages the calculation of the PDF directly from the diffraction data by Fourier transformation. ^{242}Pu is used for these experiments to avoid the resonance effect.*

the vibrations are concerned, it appears to be a rather ordinary material, and a simple continuum model can explain most of the observed diffuse scattering, which happens to be strong because of the weak interatomic forces that are characteristic of Pu. Further details of the vibrational spectrum, especially those associated with differences in different crystal directions, will have to come from more discriminating inelastic-scattering experiments now under way at the Lujan Neutron Scattering Center. It is important to continue with this challenging effort.

References

1. A.C. Lawson, B. Martinez, J.A. Roberts, J.W. Richardson, and B.I. Bennett, "Melting of the Light Actinides," *Philosophical Magazine B* **80**, 53 (2000).
2. A.C. Lawson, B. Martinez, J.A. Roberts, J.W. Richardson, and B.I. Bennett, "Atomic Vibrations and Melting in Plutonium," in *Challenges in Plutonium Science, Los Alamos Science*, Los Alamos National Laboratory report LA-UR-00-4100 (2000); http://lib-www.lanl.gov/la-pubs/00818022.pdf.
3. A.C. Lawson, B. Martinez, J.A. Roberts, B.I. Bennett, and J.W. Richardson, Jr., "Neutron Diffraction and the Anomalous Melting Point of Plutonium," at http://lansce.lanl.gov/research/condmatter/lawson.htm.
4. B.E. Warren, *X-Ray Diffraction* (Addison-Wesley, Reading, Massachusetts, 1969); (reprint, Dover Publications, Mineola, New York); http://www.iucr.org/iucr-top/people/warren.htm.
5. P. Debye and H. Menke, *Physikalische Zeitschrift* **31** 797 (1930); (English reprint, Ox Bow Press, Woodbridge, Connecticut); http://www.nobel.se/chemistry/laureates/1936/debye-bio.html.
6. A.C. Lawson, B. Martinez, R.B. Von Dreele, J.A. Roberts, R.I. Sheldon, and J.W. Richardson, Jr., "Vibrational Order in Pu$_{0.98}$Ga$_{0.02}$," *Philosophical Magazine B* **80**, 1169 (2000).
7. D. A. Dmitrov, D. Louca, and H. Röder, "Phonons from Neutron Powder Diffraction," *Physical Review B* **60**, 6204 (1999).
8. *Local Structure from Diffraction*, S.J.L. Billinge and M.F. Thorpe, Eds. (Plenum Press, New York, 1998).
9. A.C. Lawson, J.A. Roberts, B. Martinez, and J.W. Richardson, Jr., "Electron Correlation and Plutonium Phase Diagrams," in *Electron Correlation and Materials Properties*, A. Gonis, N. Kioussis, and M. Ciftan, Eds. (Kluwer Academi Publishers/Plenum Press, New York, submitted 2001); http://lib-www.lanl.gov/la-pubs/00796114.pdf.
10. W. Reichardt and L. Pintschovius, "Influence of Phonons of the Pair Distribution Function Deduced from Neutron Powder Diffraction," *Physical Review B* **63**, 174302 (2001).

Research Highlights

Small-Angle Neutron-Scattering Study of a Thermally Aged, Segmented Poly(ester urethane) Binder

J.T. Mang, P.D. Peterson (DX Division), E.B. Orler, D.A. Wrobleski, D.A. Langlois (MST Division), L.I. Espada, R.P. Hjelm (LANSCE Division)

Small-angle-neutron-scattering (SANS) measurements have been performed on a thermally aged polymeric binder to understand the effects of aging on its microstructure. The binder is a 50%-50% (by weight) mixture of a segmented poly(ester urethane), known as Estane® 5703, and a nitroplasticizer (NP). This compound is of interest because it is used in the high-explosive (HE) PBX9501. The addition of the polymeric binder to the crystalline HE imparts both structural integrity and plasticity to the HE, allowing it to be readily machined and pressed to specific densities. In addition, the binder significantly affects the performance and the sensitivity of the HE, due in part to its influence on the propagation of microstresses between crystalline grains under shock or loading conditions. So changes in the binder over time can influence the behavior of the HE system as a whole.

In addition to the application discussed here, segmented polyurethanes[1,2] belong to a well-studied class of thermoplastic elastomers that have important commercial applications. The backbone of segmented polyurethanes is composed of alternating hard and soft segments. The thermodynamic incompatibility between these segments causes segregation into hard and soft segment-rich domains that provide the material with unique mechanical and thermal properties. A number of parameters influence this segregation process (and hence the mechanical properties), including molecular weight distribution, hard-segment content, thermal history, and annealing temperature.[1,2] For the binder described in this research highlight, the introduction of NP further complicates the phase-separation process. Previous studies have shown that the NP prefers to associate with the soft segments.[3] A change in this distribution over time may affect the mechanical properties of the binder and thus the behavior of the HE system.

Our goal for this work is to understand the influence that polymer/plasticizer interactions have on the structure and properties of polyurethanes. This understanding will help aid in the development of predictive models for the safety, performance, and lifetime of HE systems. Mechanical-properties testing has shown

a monotonic decrease in the Young's modulus of the binder with increased thermal aging, whereas thermal analysis has revealed irreversible changes in the endotherm associated with disruption of the hard-segment domains.[4]

Previously, we have studied the effect of hydrolytic aging of deuterated model Estane and found that the structure of the polyurethane coarsens and phase separates at 70°C over a period of several weeks. Here we discuss SANS studies of the morphological changes in the thermally aged binder in the presence of deuterated plasticizer.

Experiment

We performed SANS measurements on the Low-Q Diffractometer[5] (LQD) at the Lujan Neutron Scattering Center. The LQD can provide detailed structural information over length scales from 10 to 1,000 Å. In a SANS experiment, neutrons will scatter from fluctuations in the scattering length density, $\rho(r)$, which reflects microscale structure.[6] The intensity of the scattered radiation, $I(Q)$, is measured as a function of the scattering vector, Q, of magnitude $Q = (4\pi/\lambda)\sin\theta$, where λ is the wavelength of the incident radiation and θ is half of the scattering angle. The scattering for the binder under study depends both on the structure of the domains, through the form factor, $P(Q)$, and on the domain packing through the structure factor, $S(Q)$, as $I(Q) \propto N \overline{\Delta\rho}^2 <P(Q)S(Q)>$. Here, $<>$ indicates an average in structure and orientation, N is the number of domains, and $\Delta\rho$ is the scattering-length-density contrast between the average scattering length density of the hard segment-rich domains and that of the surrounding soft segment-rich regions. SANS takes advantage of the large difference in scattering length between hydrogen and deuterium. We can change $\Delta\rho$ by selectively deuterating one of the components of the system and thus obtain more detailed structural information. To this end, the current experiments were performed with a deuterated NP.

Samples for this study were prepared by mixing 3.0 g of deuterated NP with 3.0 g of Estane® 5703 (which contains 23% hard segment) dissolved in a 10 w/v solution of methyl ethyl ketone. No stabilizer was used. The solution was mixed for several hours and then cast in a

petri dish. The solvent was allowed to slowly evaporate and dry in air for several days. The samples were then removed from the petri dish and placed under vacuum for 48 hours. At this time the samples were cut into disks ~ 13 mm in diameter and 0.5 mm thick. The disks were placed in scintillation vials and then placed in convection ovens, under ambient humidity, set at 40°C, 50°C, 60°C and 70°C for periods of 1.5, 3.0, and 6.0 months.

Results and Discussion

Fig. 1 shows SANS data for binder samples thermally aged for 1.5 months at temperatures ranging from 40° to 70°C. The data are characterized by the appearance of a broad peak, which is centered at Q ~0.025 Å^{-1}. The peak arises from the segregation of the plasticizer into the soft segments,[3] which results in enhanced contrast between the hard segment-rich domains and the soft segment-rich matrix in which they are dispersed. The position of the peak corresponds to an average domain size of ~ 100 Å. With increasing aging temperature, the intensity of the peak decreases, indicating changes in the binder microstructure. At 70°C the peak remains, though with reduced intensity, suggesting that significant structure is still present. The peak center appears to have shifted to a smaller Q-value, which would indicate an increase in the domain size. However, the apparent shift could be caused by the reduced contribution of the peak relative to the total scattering signal. The same trend is seen in the samples that were aged for 3.0 months (Fig. 2), but at 70°C the peak intensity is more significantly reduced. Fig. 3 shows the SANS data after aging for 6 months. We again see that the peak intensity decreases with increasing temperature and disappears after 6.0 months at 70°C. Fig. 4 shows a plot of the peak intensity, which was normalized to the peak intensity measured at 40°C, as a function of temperature for all three sets of samples. From the rate of decrease of the peak intensity with increasing temperature, we see that the most significant microstructural changes occurred after 6.0 months, as might be anticipated. For all three aging times, however, the most significant decrease in intensity occurs above 60°C.
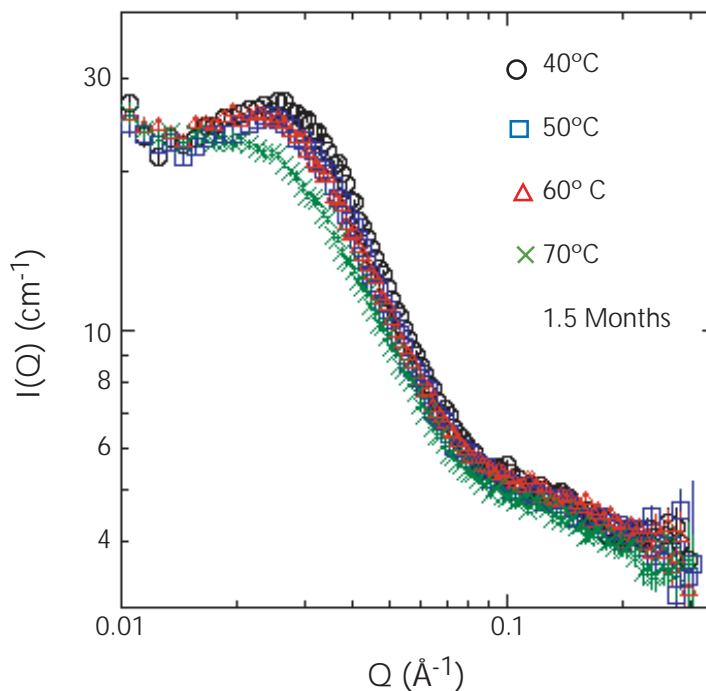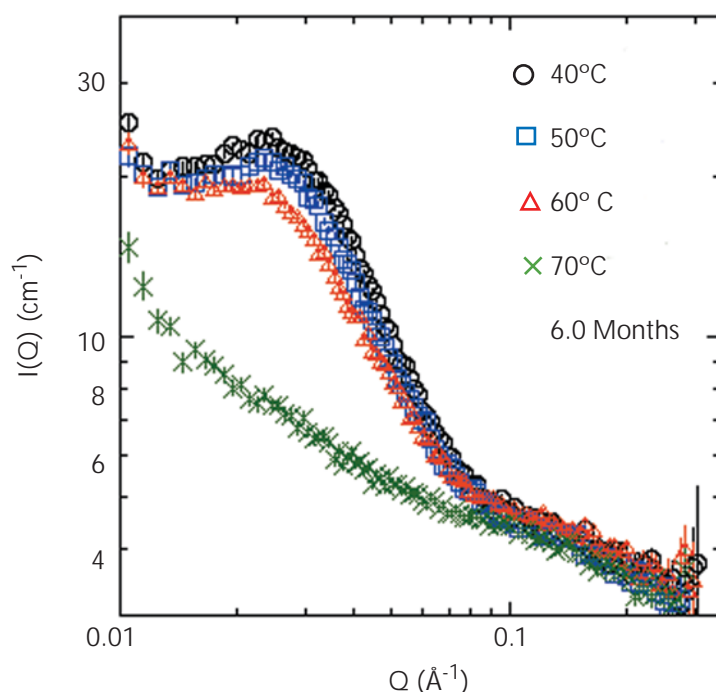

↑ Fig. 1. *SANS data of binder thermally aged for 1.5 months. A decrease in the peak intensity indicates changes in the binder microstructure.*
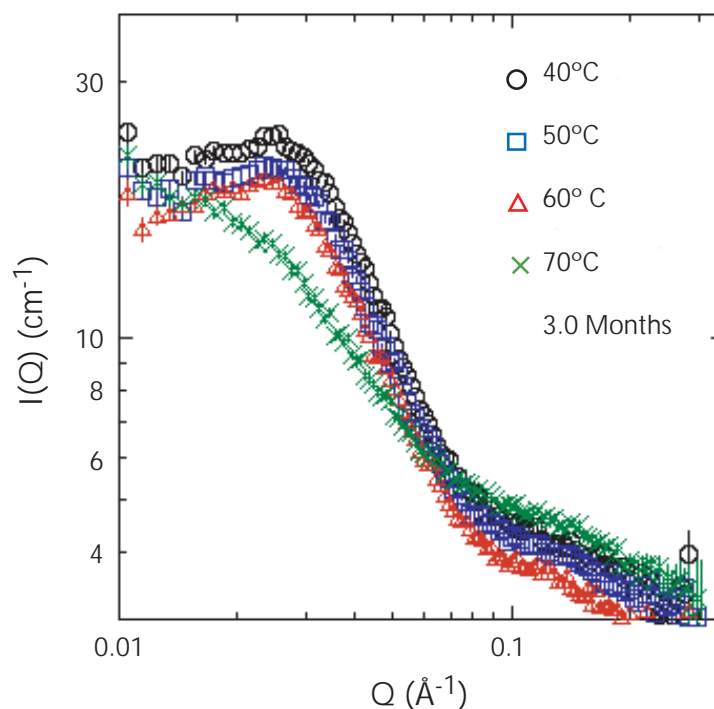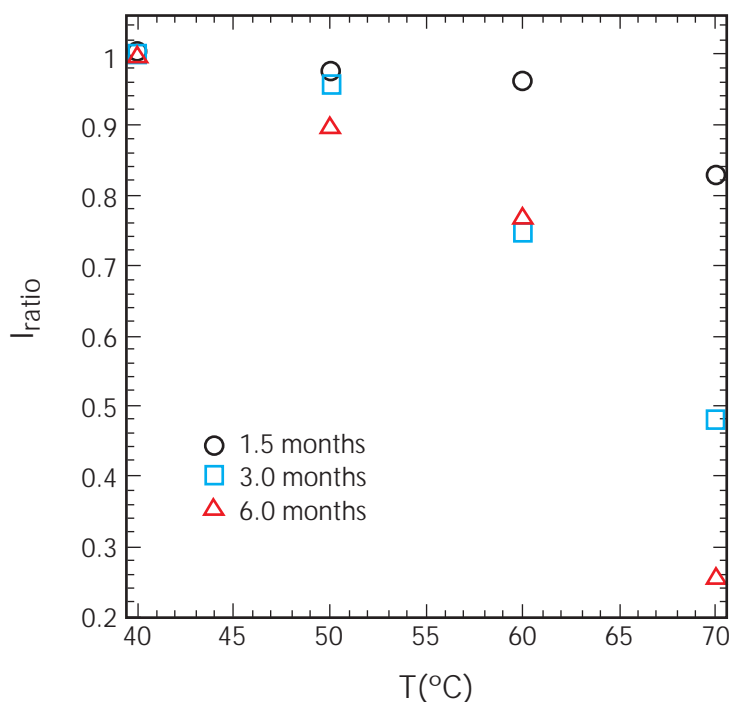

↑ Fig. 2. *SANS data of binder thermally aged for 3.0 months.*

↑ Fig. 3. *SANS data of binder thermally aged for 6.0 months. At an aging temperature of 70°C, the scattering peak disappears, which indicates significant disruption of the binder microstructure.*

↑ Fig. 4. *Peak-intensity ratio as a function of aging temperature. The more rapid decrease of the intensity after 6.0 months indicates more significant alteration of the microstructure.*

As mentioned previously, the decrease in peak intensity with increasing temperature and time is indicative of microstructural changes. From the above relationship for I(Q), we see that two different microstructural changes can account for this loss of intensity. The first change is a redistribution of the NP. We know that the NP tends to segregate into the soft segment-rich regions.[3] This segregation of the NP causes the contrast ($\Delta\rho$) between the soft and hard segment-rich domains to increase. If the domain structure remains unchanged with aging and the NP becomes more uniformly distributed throughout the sample (or segregates to the hard segment-rich domains), then $\Delta\rho$ will decrease, and the overall intensity will decrease as $\Delta\rho^2$. The second possible change is a remixing of the hard and soft segments, or "limited-phase segregation," caused by cross-linking or branching reactions. This remixing process results in a loss of the domain structure. This second type of effect is anticipated from the known thermodynamics of segmented polyurethanes[1,2] and from thermal analysis performed on the aged binder.[4] A combination of these two effects is probable as the samples are heated to a high enough temperature to cause a remixing of the hard and soft segments, and a redistribution of the NP would coincide with the remixing process.

The data discussed here were measured about one year after the samples were removed from the convection ovens. During this time, the samples were stored in scintillation vials at room temperature. Our current results match those obtained soon after removing the samples from the oven, indicating that the aging-induced morphological changes are stable. This finding is in contrast to morphological changes seen in SANS studies of direct heating and cooling of the binder.[7] Similar to the current results, these studies show a loss of structure at ~ 70°C, but they reveal a recovery of the structure upon cooling.

Conclusion

We have performed SANS experiments on thermally aged poly(ester urethane) binder. We have found, that with increasing aging time and temperature, the scattering peak

that corresponds to the formation of hard segment-rich domains disappears, indicating homogenization of the microstructure. These changes show qualitative agreement with results of mechanical testing and thermal analysis. The microstructural changes are stable; SANS measurements made a year apart yield the same results. The disappearance of the scattering peak might be caused by a redistribution of the NP, a remixing of the hard and soft segments, or a combination of the two. This is in strong contrast to the results of hydrolytic aging of model Estane without plasticizer, which shows increased hard and soft segment-rich phase separation with soft segment-rich chain scission. We are currently planning additional experiments and a more detailed analysis of the data to clarify the observed changes.

References

1. J.W. Van Bogart, P.E. Gibson, and S.L. Cooper, *Journal of Polymer Science, Polymer Physics*, **21**, 65 (1983).
2. J.T. Koberstein, A.F. Galambos, and L.M. Leung, *Macromolecules*, **25**, 6195 (1992), and references therein.
3. L.I. Espada, J.T. Mang, E.B. Orler, D.A. Wrobleski, D.A. Langlois, and R.P. Hjelm, *Polymer Preprints* **42** (2001).
4. E.B. Orler *et al.*, to be published.
5. P. Seeger and R.P. Hjelm, *Journal of Applied Crystallography* **24**, 467 (1991).
6. O. Glatter and O. Kratky, *Small Angle X-ray Scattering* (Academic Press, London, 1982).
7. J.T. Mang, E.B. Orler, and R.P. Hjelm, unpublished results.

Research Highlights

Investigating Confined Complex Fluids with Neutron Reflectivity

T.L. Kuhl (University of California at Davis), G.S. Smith, J. Majewski (LANSCE Division), W. Hamilton (Oak Ridge National Laboratory), N. Alcantar (University of California at Santa Barbara)

Polymer molecules at solid or fluid interfaces have an enormous spectrum of applications in a wide variety of technologies, including lubrication, adhesion, and protective surface coatings. Over the past decade, neutron reflectivity has become a powerful tool for measuring the properties of ultra-thin polymer layers at interfaces. In this research highlight, we describe how the penetrating power of neutrons can be harnessed to probe the structure of ultra-thin polymer coatings trapped between two surfaces as a function of confinement. Fig. 1 schematically depicts the fundamental question we are trying to answer—that is, what happens when two surfaces come into contact. In the case of two polymer "brush" layers in solution (Fig. 1), two possible scenarios are shown: (1) the polymer layers compress but remain separate from each other or (2) the polymer layers interpenetrate.
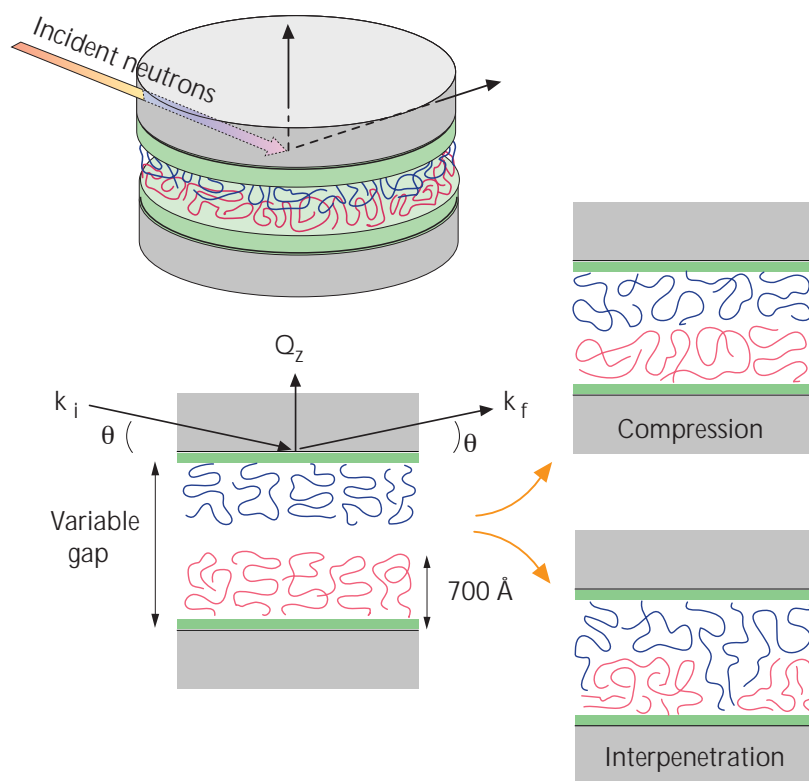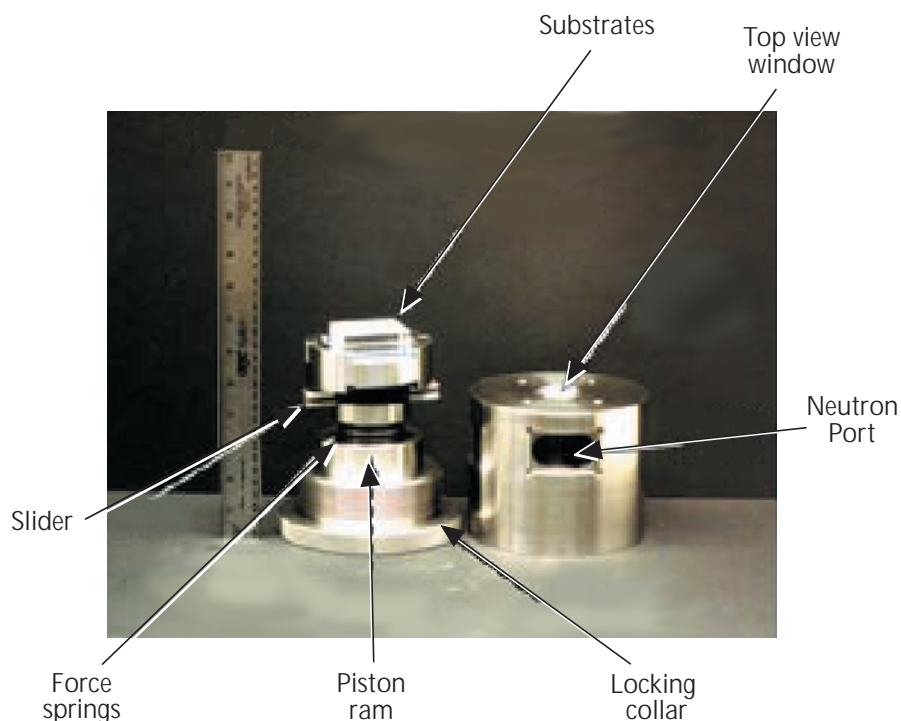
Depending on the outcome, the adhesion, lubrication, or shear behavior of the surfaces can be greatly altered. Our goal is to understand what happens when polymer layers are brought together, using a unique device that we developed and successfully tested (i.e., the Neutron Confinement Shear Cell).

Understanding Surface Behavior of Polymer Layers with Neutron Reflectometry

Neutron reflectometry is a surface-sensitive neutron-scattering method that takes advantage of the wave properties of the neutron probe reflected from the sample. The reflection of neutrons from the surface of a polymer film allows us to characterize the surface structure at the nanometer level. With this level of resolution, we can determine the thickness, roughness, uniformity, and density profile of the layers normal to the surface. Neutron-scattering techniques (e.g., compared to x-ray techniques) have a number of advantages compared to other techniques: (1) they do not cause radiation damage to the sample; (2) by using contrast-matching procedures, parts of stratified layers may be highlighted or screened out; and (3) neutrons can penetrate thick substrates to probe the structure of buried interfaces. All three features are important for the study of confined polymer layers.

For these studies, we designed the Neutron Confinement Shear Cell apparatus (Fig. 2) in which single-crystal substrates of silicon, quartz, or sapphire (with areas up to tens of square centimeters) are kept parallel at controlled and well-defined separations (i.e., from millimeters to less than 100 nm). A large substrate surface area is required for neutron-reflectivity measurements, and parallel alignment of the substrates is crucial.


↑ **Fig. 1.** *Geometry of the neutron reflectivity measurements and two possible structural rearrangements of polymer brush layers in contact: (a) brush compression and (b) brush interpenetration.*

Substrates

Top view window

Neutron Port

Slider

Force springs

Piston ram

Locking collar

↑ **Fig. 2.** *Neutron Confinement Shear Cell used in the experiments. During experiments, the apparatus on the right is placed over the apparatus on the left.*

Indeed, the surface variation of our substrates is less than 350 Å (λ/20). Using Belleville washers of known spring constant, the applied force to compress the intervening material can be correlated with the inter-substrate separation. The cell is also designed to apply steady shear rates from 0.001 Hz to 20 Hz so that we can follow the dynamic structural response of the con-fined material, especially at the solid-solution inter-face. Shear rates of the order of 10^4 can be obtained using oscillatory motion.[1]

During the 2001 Los Alamos Neutron Science Center (LANSCE) run cycle, neutron-reflectivity measurements were used to determine the density distribution of spin-coated polystyrene(PS)-polyvinlypyridine (P2VP) diblocks on the substrates. The molecular weight of our polymer sample, PS-P2VP, was 120,000 g/mol. The P2VP portion of the diblock was hydrogenated, whereas the PS portion was either hydrogenated or deuterated to take advantage of contrast labeling. Previously, the structure of PS-P2VP layers at a single surface was char-acterized by Levicky and coworkers.[2]

As can be seen in Fig. 3, interference fringes are clearly visible in the reflectivity profile at high Q, which is indicative of the substrate spacing (about 1,600 Å). Further measurements were done with toluene, which is a good solvent for polystyrene. The toluene was wicked between the substrates at the 1,600-Å inter-substrate separation to solvate (wet) the polymer layers without changing the gap between the substrates. At a single surface, the PS-P2VP layers are 700 Å thick.[2] Thus, the opposite polymer-brush layer should slightly overlap for this case. As shown in Fig. 4, the PS-P2VP layers are about 600 Å thick with an inter-substrate separation of about 1,500 Å. This thickness is significantly less than expected based on the 700-Å thickness observed at a single surface. Furthermore, the density profile of the polymer brush has a fairly sharp parabolic form, and because no exponentially decaying density "tail" at the edge of the polymer layer was detected, the polymer layers evidently become flattened with little or no inter-penetration.
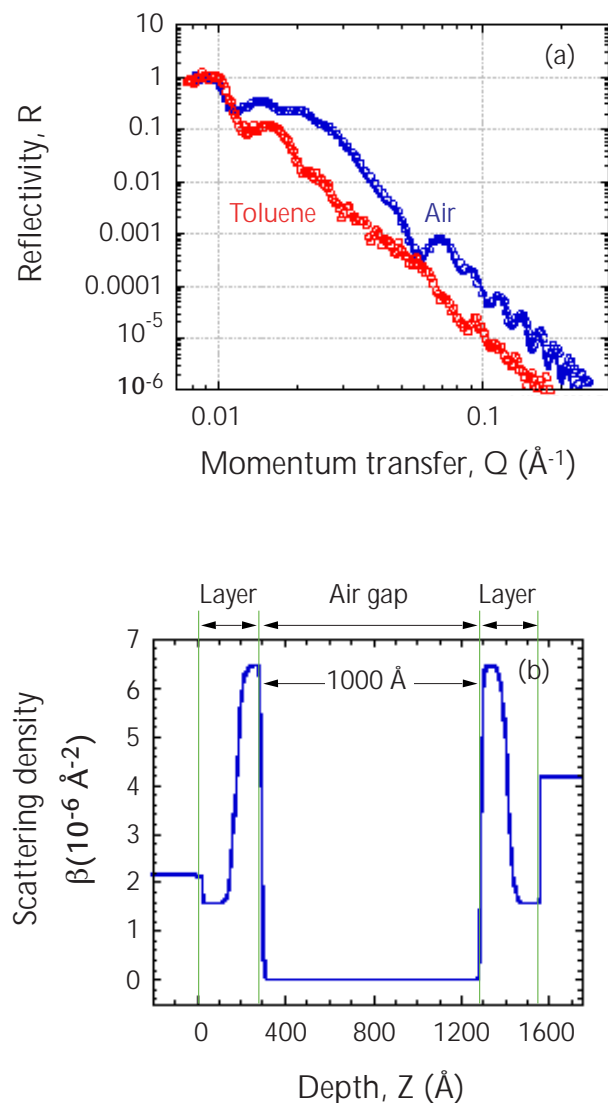
↑ Fig. 3. *(a) Experimentally measured reflectivity profile of polymer brush layers in the neutron confinement shear cell, including the model fit (i.e., from the scattering density profile in b). The same PS-P2VP layers in air (blue) are then solvated with h-toluene (red). The inter-substrate separation is still 1,600 Å, and the PS layers are separated by 1,300 Å. At a single surface, the PS-P2VP brush layers are about 700 Å thick. Under the conditions shown, the polymer brush layers are just overlapping. Subsequent measurements were done with smaller inter-substrate separations. (b) Scattering density profile corresponding to the experimentally measured reflectivity profile in a. The inter-substrate separation is about 1,600 Å, whereas the gap between the opposing polymer layers is about 1,000 Å.*
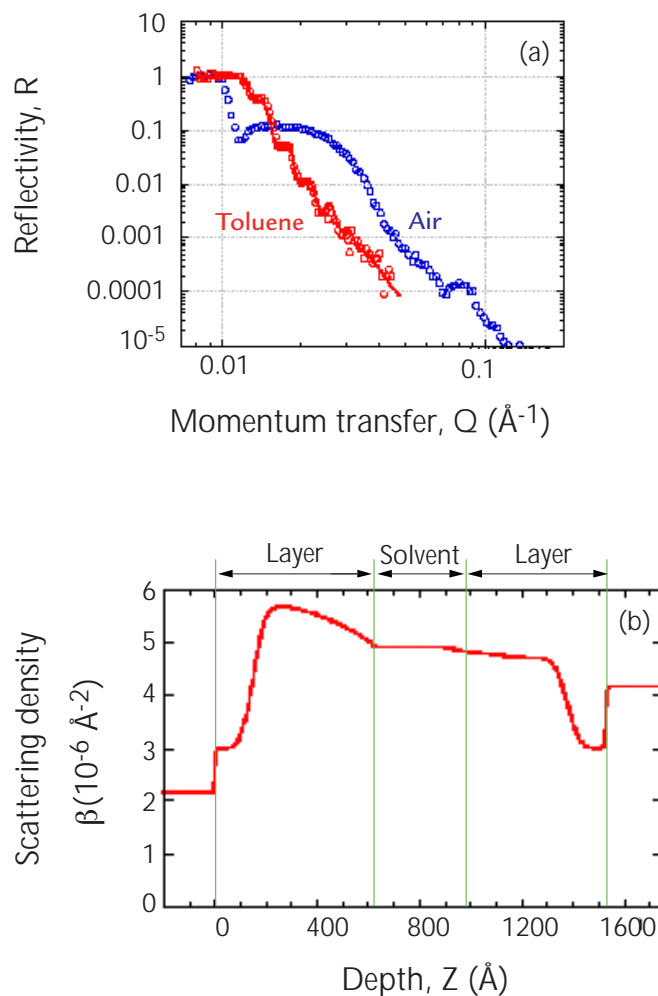
↑ Fig. 4. *(a) Experimentally measured reflectivity profile of an asymmetric dPS-P2VP against an hPS-P2VP layer in the neutron confinement shear cell, including the model fit (i.e., the red curve corresponding to the scattering density profile in b). The inter-substrate separation is again 1,600 Å, so that the PS layers are just overlapping. (b) Scattering density profile corresponding to the experimentally measured reflectivity profile in d-toluene (solvent) in a (red). The inter-substrate separation is about 1,600 Å. As shown, the PS-P2VP layers are about 600 Å thick, which is less than expected based on the 700-Å thickness observed at a single surface. The brush layers exhibit a sharp parabolic profile, and we did not detect an exponentially decaying tail at the edge of the polymer layer.*

Conclusion

Our results indicate that quantitative measurements of the scattering density profile of polymer-brush layers can be made using the Neutron Confinement Shear Cell with neutron-reflectivity techniques at LANSCE. We measured a variety of inter-substrate separations and levels of confinement during the 2001 LANSCE run cycle and are currently analyzing and preparing the data for publication. Such measurements have never been accomplished previously and thus may greatly impact polymer science, simulations, and theory. Based on the success of these measurements, the Neutron Confinement Shear Cell will provide us with a new technology to probe the structure of complex fluids or other materials of interest under confinement in a defined geometry.

References

1. T.L. Kuhl, G.S. Smith, J. Israelachvili, J. Majewski, and W. Hamilton, "Neutron Confinement Cell for Investigating Complex Fluids," *Review of Scientific Instruments* **72**, 1715-1720 (2001).
2. R. Levicky, N. Koneripalli, M. Tirrell, and S. Satija, "Concentration Profiles in Densely Tethered Polymer Brushes," *Macromolecules* **31**, 3731-3734 (1998).

Research Highlights

Probing Adsorbate Structure in Catalytic Materials Using Inelastic Neutron Scattering

N.J. Henson, P.J. Hay (T Division), L.L. Daemen (LANSCE Division), G. Koermer (Engelhard Corporation), J. Eckert (University of California at Santa Barbara/STB Division)

Catalysts play an important, yet shrouded, role in our everyday lives. From a purely chemical standpoint, they provide a method for accelerating (or in rare cases, decelerating) the rate of chemical reactions. Catalysts are therefore used in a wide variety of biological and notably industrial processes to produce many useful products. For example, the majority of reactions responsible for the formation of plastics (and their ubiquitous presence in the world) are possible through catalytic processes. A fundamental understanding of the operation of catalysts at the atomic level has long been the ultimate goal of many chemists. An understanding of the intricacies of these processes would result in our ability to tailor catalytic reactions to ultimately develop more efficient processes.

For many years, industrial catalysis was somewhat of a black art. Numerous catalytic formulations were synthesised by making subtle changes in the synthetic conditions and tested for their efficacy. The most efficient formulations were thus adopted for further study and possible integration into larger-scale industrial environments. However, in more recent times, the development of more sophisticated experimental techniques and access to high-performance computing have allowed chemists to ask fundamental questions about catalytic processes. The aim of our work was to exploit two unique capabilities available at Los Alamos National Laboratory—neutron scattering and high-performance computation—in helping us understand the behavior of molecules of catalytic interest in a zeolite catalyst.

### Examining the Unique Properties of the Zeolite ETS-10

In the mid 1700s, Swedish mineralogist Axel Fredrik Crønstedt discovered a hydrous mineral that appeared to boil when heated. He named this mineral *zeolite* from the Greek *zeo* (to boil) and *lithos* (stone). Zeolites are nanoporous aluminosilicate materials with cavities and channels of molecular dimensions. They are often hydrated and contain exchangeable metal cations. Over the past few decades, the application of zeolites in science and industry has increased tremendously because of their unique adsorption, catalytic, and ion-exchange properties. Zeolites have been specifically used as catalysts for petroleum refining and other petrochemical processes. They are also used as water-softening agents in laundry detergents and as molecular sieves for absorption, desiccant, and separation applications. Those used as catalysts in the petrochemical industry, for instance, crack (or break down) long chain molecules found in crude oil into smaller molecules that constitute gasoline. Because of their practical and economic importance, there is a great deal of interest in understanding how zeolites function at the atomic or molecular level.

Channels (or pores) running through the structure of a zeolite interconnect cavities and terminate at the surface. These channels, which vary in size and shape depending on the chemical composition and crystal structure of the mineral, allow ions and guest molecules ease of movement into and out of the structure of the host zeolite. Titanium-substituted zeolites have been observed to interact much differently with certain adsorbate molecules (such as H_2O and H_2O_2) than do conventional molecular sieves. Some titanium-containing zeolites, like TS-1, have already been commercialized as catalysts for the synthesis of certain polymers. We are interested here in the zeolite ETS-10, which is made up of SiO_4 and TiO_6 polyhedra in a three-dimensional interlocking framework that produces cavities where ions and water molecules can be loosely held (Fig. 1). The structure of the ETS-10 zeolite has a high charge density combined with a molecular-sieve architecture that gives it interesting ion-exchange and adsorption properties. The catalytic properties of the ETS-10 framework are as yet largely unexplored. Because adsorption is a fundamental step in catalysis, we hope to gain invaluable insight into unusual and unexpected modes of molecular adsorption within the ETS-10 framework. This insight could serve as an important step not only for the development of new catalytic systems based on titanium-containing zeolites but also for significant advancements in the science of molecular sieves. The mechanisms responsible for the catalytic activity in these materials are generally not known, and few experiment probes are able to investigate the structure of the active site.

Experimental Details

Using the Filter Difference Spectrometer (FDS) at the Lujan Neutron Scattering Center, we studied the dynamics of adsorbed molecules with a method known as molecular-vibrational spectroscopy by inelastic-neutron scattering (INS) to gain an understanding of
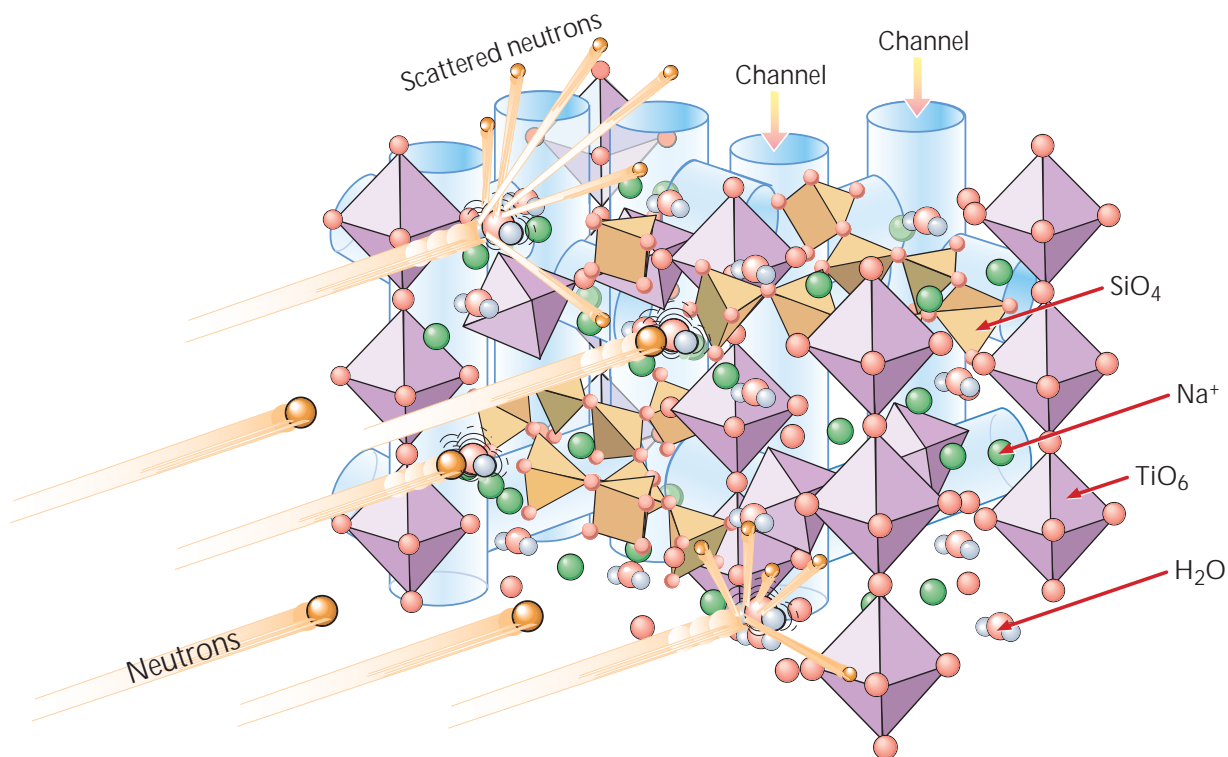
↑ Fig. 1. *ETS-10 zeolite framework (unit cell). Neutrons interact strongly with the hydrogen atoms in the water molecules within the porous structure, transferring kinetic energy to them and exciting molecular vibrations.*

the catalytic mechanism in ETS-10. When guest molecules are adsorbed in zeolite pores, their characteristic internal vibrational frequency may be shifted as a consequence of their interaction with the zeolite internal surface. These vibrations are much like fingerprints in that they are unique to the adsorbed molecules and their binding site. The vibrations therefore help scientists distinguish among the molecules within the framework of the zeolite. The INS method on the FDS is well suited for studying the vibration of water molecules adsorbed in ETS-10 because neutrons interact strongly with the hydrogen atoms in the molecules. Incident neutrons excite molecular vibrations by giving up kinetic energy upon scattering in the zeolite sample. These molecular vibrations help scientists determine the local structure of the binding sites on the internal surfaces of the host zeolite where the water molecules are located. As a result, they gain insight into the catalytic mechanism at work within the ETS-10 framework.

Results

A sample of the data collected on FDS is shown in Fig. 2. The vibrational spectrum obtained shows a number of strong peaks in the low-frequency region. These strong peaks are generally associated with motions of the adsorbate molecule bound to sites in the pores of the zeolite. The frequency and intensity of the peaks are indicative of the geometry and strength of the interaction of the adsorbate molecule with the ETS-10 zeolite framework. The adsorbate in this case was methanol, CH_3OH. However, by substituting one or more of the adsorbate hydrogen atoms by deuterium (which are poor neutron scatterers), for example, using CD_3OH, we can effectively remove any vibrations involving those atoms from the measured spectrum. Using this technique, we can focus in on specific functional groups within the molecule.

Using a computational method, we *assigned* the spectrum to relate the peaks in the neutron-scattering spectrum to actual displacements of groups of atoms in the adsorbate molecule (and thus to relate them to the binding geometry of the adsorbate molecule in the zeolite pore). The strategy is as follows. Based on the experimentally determined crystal structure of EST-10, we can construct possible models for the binding of adsorbates in the pore structure. For each candidate

structure, we calculate the vibrational spectrum and then use these data to fit to the experimental data. From this approach, we can determine the model that fits the experimental data most closely.

Although we are in the early stages of these calculations for ETS-10, we can illustrate the technique by referring to previous work that we have performed on another zeolite-sorbate system. In this work, we attempted a similar experiment and calculation on the behavior of ethane, C_2H_6, and ethene, C_2H_4 in the zeolite Na-Y. The two adsorbate molecules differ mainly in that ethene has a C=C double bond, whereas in ethane there is only a single bond between carbon atoms. This combination was of little catalytic interest, but it provided a relatively simple system as a proof of principle.

In the case of ethane in Na-Y, calculations indicated that a large number of similarly favorable binding sites
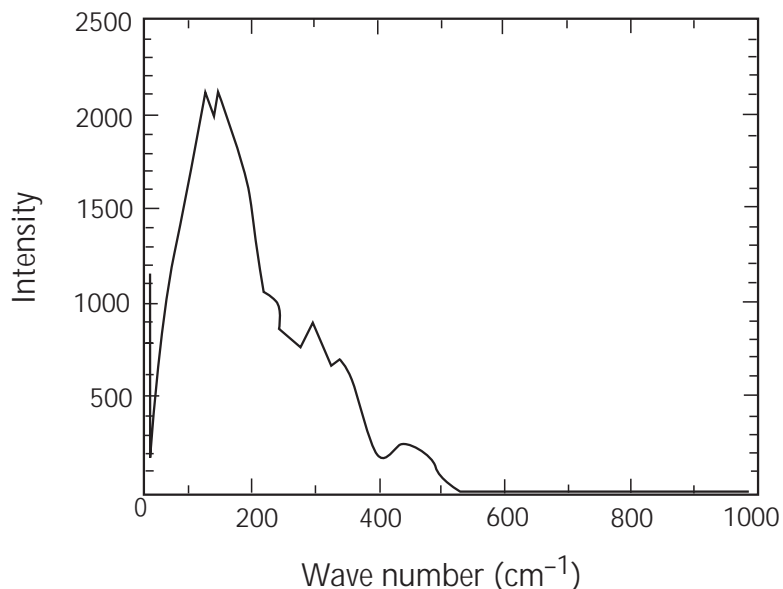
↑ Fig. 2. *INS spectrum of methanol in the zeolite ETS-10.*

would be present for the adsorbate in the zeolite pore structure. This correlated well with the measured INS spectrum, which consisted of several broad featureless peaks. In contrast, the situation was significantly different for ethene. A wide range of different binding
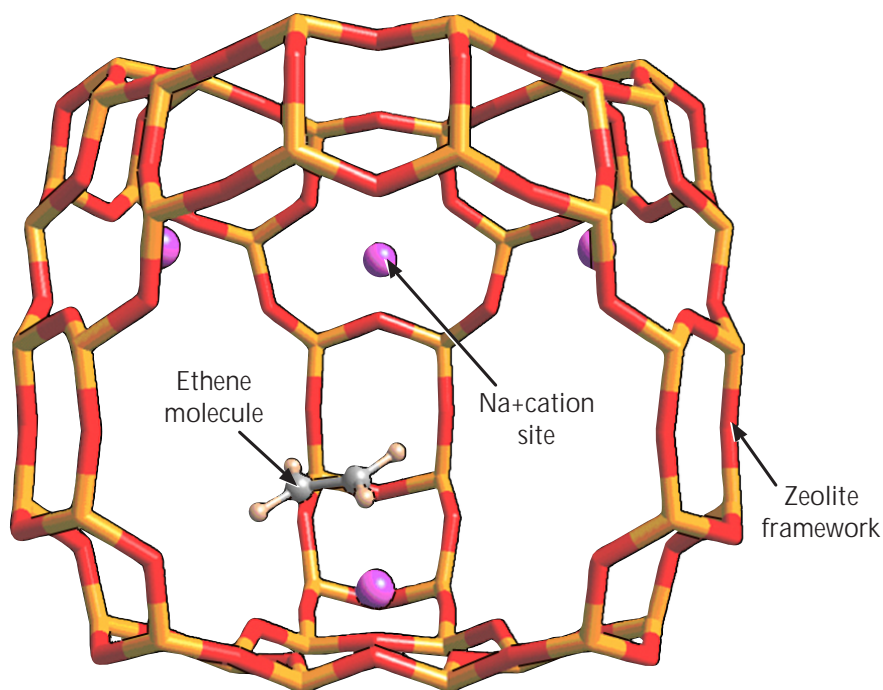
↑ Fig. 3. *Calculated binding site for ethene in zeolite Na-Y.*

sites for the adsorbate in the zeolite pore was sampled, and a Monte Carlo docking calculation predicted that the most likely binding site for ethene would involve the Na^+ cation in the zeolite structure (Fig. 3).

The carbon-carbon double bond in ethene appears to be the determining factor in this case for the general features of the binding site. Using this model, the vibrational spectrum for ethene was calculated and

used to fit the INS spectrum. The result is shown in Fig. 4. We obtained reasonable agreement between experiment and calculated spectra, and therefore we are confident that the computational method is a good approximation of the correct local environment for the adsorbate. Calculations are currently in progress to apply the same techniques to the ETS-10 system.
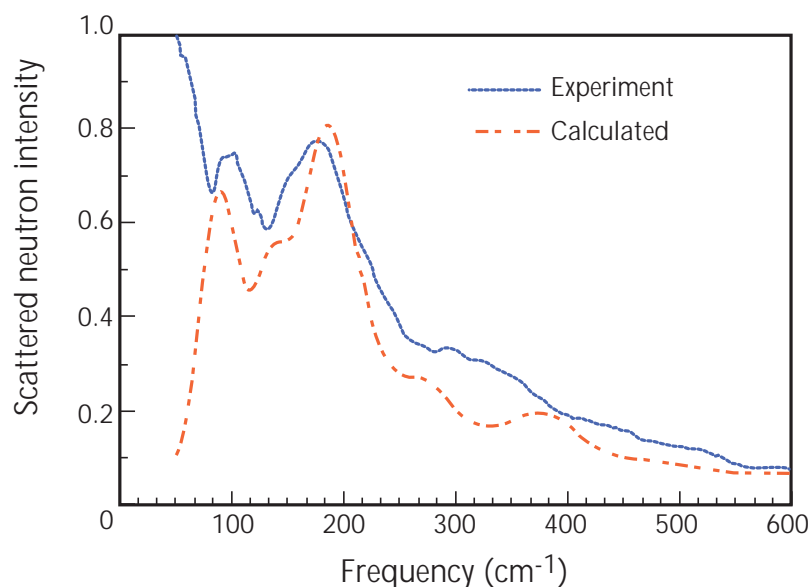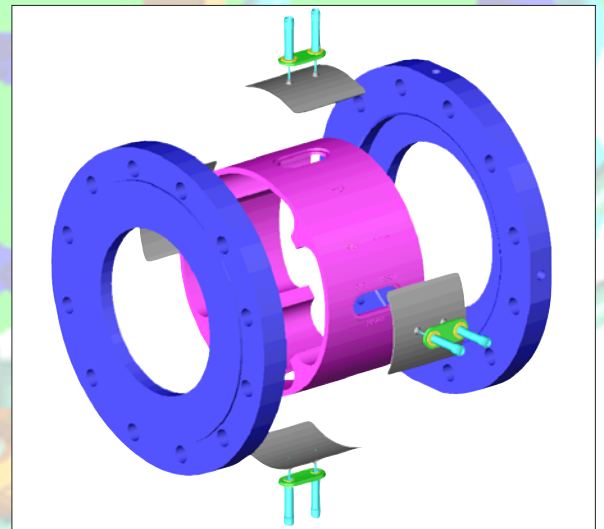

↑ **Fig. 4.** *Experimental and calculated INS spectra for ethene in Na-Y.*

Research Highlights

700-MHz, 1-MW Continuous-Wave Klystrons for the Low-Energy Demonstration Accelerator

D.E. Rees, K.A. Cummings, W.T. Roybal (LANSCE Division), J.T. Bradley, T.W. Hardek (SNS Division)

The Low-Energy Demonstration Accelerator (LEDA) was developed as part of the Accelerator Production of Tritium (APT) program. It was to consist of a 6.7-MeV radio-frequency quadrupole (RFQ) followed by a coupled-cavity-drift-tube linac (CCDTL) to accelerate a 100-mA proton beam. The RFQ operated at 350 MHz and used three 1.2-MW, continuous-wave (cw), radio-frequency (rf) stations to provide the required cavity and beam power. The CCDTL operates at 700 MHz and uses 1-MW cw klystrons as the rf power source. The designs for the RFQ components were based on rf equipment that had been developed for previous accelerators operating at 352 MHz. Radio-frequency components with a 1-MW cw power capacity were not available at 700 MHz, so new developments were required for most of the 700-MHz components. This article discusses the development of the most challenging of these components: the klystrons. Two 700-MHz rf stations were commissioned by the end of the LEDA project and were operated to conduct component, cavity, and reliability tests on the rf vacuum windows.

700-MHz Radio-Frequency Systems

LEDA demonstrated the technology to be used for the APT accelerator. The size of the APT accelerator set many requirements for the LEDA rf systems. The APT accelerator design required a total cw rf power in excess of 100 MW. For this purpose, the conversion efficiency of the alternating current (ac) from the power grid to the rf power delivered to the accelerator needed to be maximized to minimize operating costs. Because a large amount of ac power is required by the rf systems, we considered the impact of a fault in the rf on the ac power grid. This resulted in an operational requirement unique to the LEDA/APT accelerator. The klystron collector needs to absorb the full direct current (dc) in the steady state during an accelerator fault that required the removal of rf power from the cavities. The conventional practice at other cw accelerators has been to dissipate the klystron beam power for less than 10 seconds in the event of an rf fault.

The number of rf generators needed to be minimized to reduce the cost of the rf system but with a power

capacity and operational characteristics compatible with a reliable operation of the system. Architectures and designs were made to maximize operational availability. Because sections of the APT accelerator were superconducting (SC), the rf systems had to tolerate nearly full reflection of the rf power from the SC cavities in the absence of beam.

700-MHz Klystrons

A 1-MW power level was chosen for the 700-MHz klystron development with a nominal dc-to-rf conversion efficiency of 65%. This choice was based on information from klystron designers, visits to other cw accelerators, and discussions with other rf groups using high-power cw klystrons for accelerator applications. The 65% efficiency was demonstrated for klystrons operated at lower frequencies. The primary specifications for the 700-MHz klystron are included in Table 1.

Table 1. 700-MHz klystron requirements	
Frequency	700 MHz
Output power	1.0 MW
Test power	1.1 MW
Gain	40-dB minimum
Maximum electron beam voltage	95-kV maximum
Maximum electron beam current	20-A maximum
Efficiency	65% minimum
Bandwidth 1 dB	+/- 0.7 MHz
Collector dissipation	Full beam power
VSWR (voltage standing wave ratio) tolerance	1.2:1 Maximum, any phase
Modulating anode*	Yes

*The modulating anode is used to control the high voltage that accelerates the electron beam in the klystron.

When operational, modules of up to 7 klystrons would be used to drive a single CCDTL. Only 6 of the 7 klystrons would be required for operation. The additional klystron would serve as an installed and operating spare. The requirement for a modulating anode was partially derived from this architecture. The modulating anode allowed for efficiency optimization when all of the klystrons were operational at a slightly reduced power. When we selected the architecture, all cw accelerators had used modulating-anode klystrons. Since then, the B-Factory at Stanford has successfully

been commissioned with 1-MW-class cw klystrons without a modulating anode, and the Spallation Neutron Source is using high-average power-pulsed klystrons without modulating anodes. Based on these recent developments, we would now recommend eliminating the modulating anode and using a klystron with a diode gun.

Two klystron vendors (Marconi and CPI) were selected to develop the 700-MHz klystron. Two conventional, high-efficiency klystrons were therefore developed. An advanced klystron design using an additional second-harmonic cavity just prior to the output cavity was also attempted by Marconi. This klystron had to minimally meet the requirements in Table 1, but the development was directed toward increasing the efficiency to 70%. The results of the three developments are listed below in Table 2.

Table 2. 700-MHz klystron test results			
	Marconi klystron	CPI klystron	Advanced Marconi klystron
Electron beam voltage	95.1 kV	92 kV	95.1 kV
Electron beam current	16.28 A	16.6 A	15.57 A
Modulating-anode voltage	51.52 kV	78 kV	46.67 kV
Modulating-anode current	0.15 mA	1.4 mA	0.3 mA
Drive power	75 W	12.3 W	96 W
Output power	1,013 kW	1,000 kW	1,007 kW
Efficiency	65.4%	65.5 %	68%
Body power	4.0 kW	3.7 kW	3.9 kW
Output cavity power	6.2 kW	8.6 kW	6.9 kW

All three klystrons met the required specifications. The advanced klystron design indicated a slight improvement in efficiency during factory testing but was found unstable at Los Alamos National Laboratory and needed to be retuned for stable operation. After it was retuned, the klystron only achieved 65% efficiency, and therefore the use of an additional second-harmonic cavity provided no real gain in efficiency. The CPI klystron has performed well over time. The Marconi klystrons developed a collector problem during operation. The collector design proved inadequate to dissipate the full beam power as required. Marconi took steps to improve the design, and subsequently we have not observed any additional problems. A picture of the CPI klystron is included below in Fig. 1.

↑ **Fig. 1.** *CPI klystron.*

Research Highlights
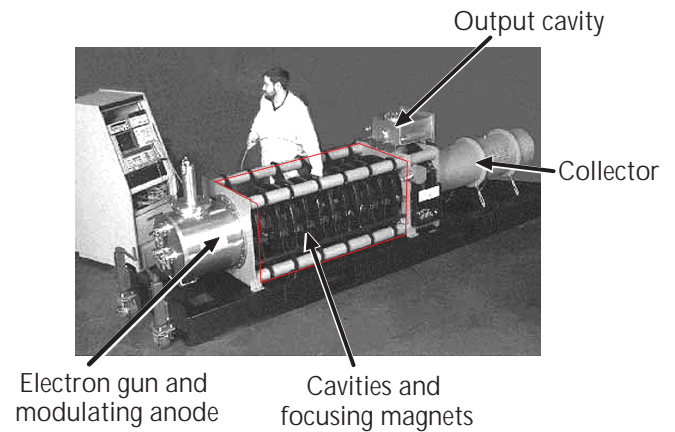
Superconducting Accelerator Technology for Low Velocity Protons

F.L. Krawczyk, J.P. Kelley, D.L. Schrage, A.H. Shapiro, T. Tajima, T.P. Wangler, M.A. Madrid (LANSCE Division), P.L. Roybal (Techsource), K.C.D. Chan, W.B. Haynes (NIS Division), R.C. Gentzlinger, D.I. Montoya, E.N. Schmierer (ESA Division)

The advantages of superconducting-radio-frequency (SCRF) resonant cavities for electron accelerators are well established.[1] The major advantage is the significant reduction in operation costs because of negligible radio-frequency (rf) losses at the surface of these cavities. The technology is also very promising for proton accelerators because, in addition to power saving, the large beam-pipe aperture minimizes radioactive contamination of the structures by use of SCRF cavities for the high-energy part of the accelerator.

### Superconducting-Radio-Frequency Resonant Cavities

SCRF cavities are resonators that consist of multiple cells (Fig. 1). They operate in a "π-mode," where the on-axis electric field inside cells at a given time alternates in sign from cell to cell. It takes the beam half an rf-period to cross a cell with the consequence that the beam always sees an accelerating field while it propagates along the accelerator.

The major difference between electron and proton accelerators is the beam velocity along the accelerator. Because of their low mass, electrons rapidly reach relativistic velocities during their acceleration, whereas protons, which are heavier, propagate more slowly and change velocity during their acceleration. All rf cavities are therefore identical for electron accelerators, but their length must be changed for proton acceleration. For sufficiently fast protons (with a velocity higher than 0.4 c, i.e., with an energy above 200 MeV), suitable structures can be derived from cavities with an elliptical-cell profile designed for electron accelerators. Cavities for protons (Fig. 1a) are similar to those for electrons (Fig. 1b) but reduced in length. Elliptical cavities have a diameter of approximately one wavelength (λ). The length of each cavity cell is $\beta\lambda/2$, where β = v/c is the beam velocity relative to that of light. For example, β = 1.0 for relativistic electrons, and β = 0.64 for the Accelerator Production of Tritium (APT) cavity in Fig. 1a.

Using a small number of cells per cavity and an independent rf-phase control of a small number of superconducting (SC) cavities allows the use of identical cavities over a range of beam velocities. For this reason,

the required number of different-sized rf cavities can be kept to two over the 200-MeV to 1-GeV proton-energy range. This concept has been used for the APT[2] and Spallation Neutron Source[3] (SNS) projects.

Below 200-MeV proton energy, the "compressed length" of an elliptical cavity for these velocities would result in mechanically unstable structures. Specifically, flattening the cavity walls makes it more difficult to resist mechanical loads and thus leads to thicker or reinforced cavities, which is a significant cost factor. Also, the small acceleration gaps would limit the accelerating field in these structures. Other types of SCRF cavities, however, have been used for protons and ions at low particle energies. The structures commonly used, named quarter-wave cavities (Fig. 2), operate at very low rf frequencies. This compensates for the reduced acceleration-gap length due to the low particle velocity (β) by a length increase due to the longer wavelengths. The quarter-wave cavities have diameters

Compressed by 36%

rf-coupler port   (a)
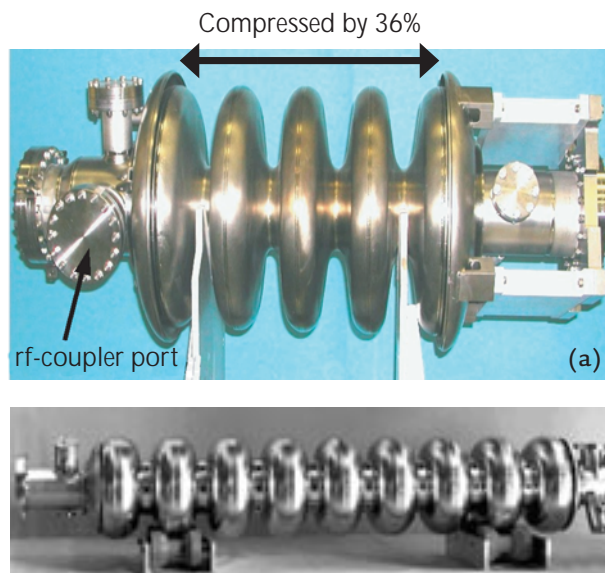
↑ **Fig. 1.** *(a) A 700-MHz, five-cell elliptical cavity, as designed for the APT accelerator. This cavity is optimized for a proton beam at 0.64 c with a 36% "compressed length" as compared to the length for a relativistic beam propagating at velocity c. The length of a cell is 13.7 cm, and the radius is approximately 20 cm. (b) A 1,300-MHz, nine-cell elliptical cavity, as designed for the TESLA (TeV Energy Superconducting Linear Accelerator)[4] project. This cavity has been designed for the acceleration of relativistic electrons. The length of a cell is 11.5 cm, and the radius is approximately 11 cm.*
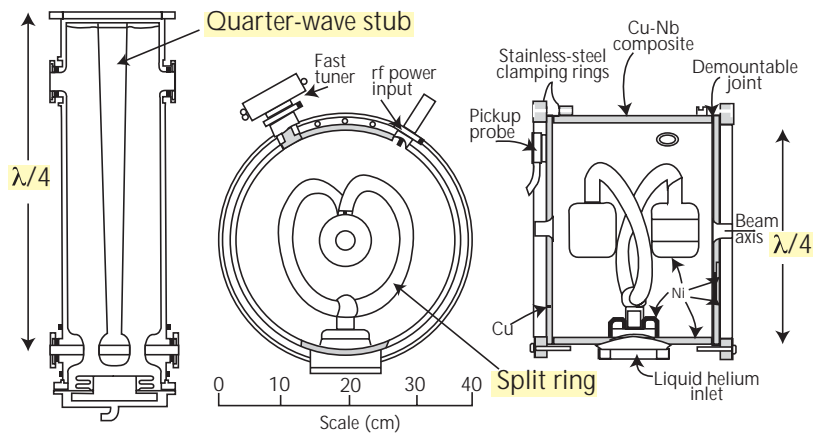
↑ Fig. 2. *Two quarter-wave structures are shown here. In both cases, an insertion (a quarter-wave stub, left, and a split ring, right) is attached to the cavity wall at one point to reduce the size of the resonator. These types of insertions give the smallest resonators for a given frequency. The double-sided arrows indicate a length of λ/4. The structures shown are used in the Argonne Tandem Linac Accelerator System (ATLAS) accelerator[5] at Argonne National Laboratory (ANL).*

on the order of one-quarter of a wavelength, and their gap length is also $\beta\lambda/2$. Their smaller size at a given frequency is an advantage over elliptical cavities. The size reduction comes from the influence of insertions in the cavity that reshape the electromagnetic fields. The disadvantage of these insertions is their mechanical instability. This instability is caused by the vibrations of these insertions, which are attached to the cavity wall at only one point. These vibrations are tolerable for low-current (and thus low-force) applications in nuclear physics. APT- and SNS-type applications need mechanically more stable structures.

For extending the use of SC cavities to low-particle velocities for high-current applications, the so-called "spoke" cavities (Fig. 3) are of more interest. At a given frequency,
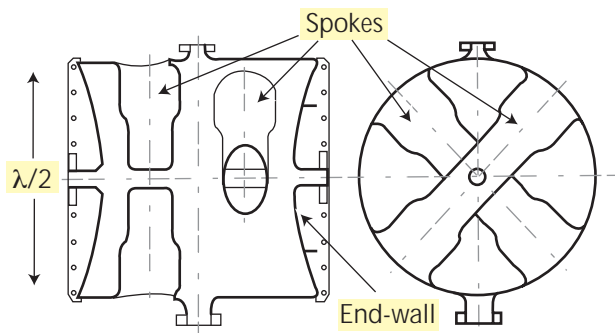
↑ Fig. 3. *A 350-MHz "spoke" cavity with two spokes inserted. The double-sided arrow indicates a diameter of λ/2. This structure has been designed for the Rare Isotope Accelerator (RIA) project[6] and matches a proton beam at 0.4 c.*

these cavities are between the quarter-wave and elliptical cavities in size and have loaded insertions (spokes) that are attached to the cavity wall at two points.[6] Their diameter is $\lambda/2$, again with gap lengths of $\beta\lambda/2$. The fact that the insertions in these structures are attached to the cavity walls in two places makes them mechanically very stable. Spoke cavities have already been studied for more than a decade but not beyond proof-of-principle tests.[7,8] Our work intends to design a cavity with realistic ancillary components like beam-pipes, rf-coupling, helium vessel, and tuning that fulfills all requirements for a high-current accelerator, including a field gradient.

There is another advantage to all these reduced-size structures: rf losses increase as the square of frequency but decrease exponentially with temperature. The lower frequency (< 500 MHz) of the structures allows operations at 4 K instead of the 2 K required for most elliptical cavities that typically operate at > 500 MHz. This low-frequency capability reduces the size and complexity of the cryogenic cooling system.

Spoke-Cavity Design for the Advanced Accelerator Applications Project

The Advanced Accelerator Applications project,[2] whose main objective is the transmutation of nuclear waste with an accelerator known as the Accelerator Transmutation of Waste, is planning to use the Low-Energy Demonstration Accelerator (LEDA) and the radio-frequency quadrupole (RFQ). Both LEDA and the RFQ have been successfully operated. The accelerator layouts proposed make use of SCRF cavities starting at the RFQ output energy of 6.7 MeV, which led to our design work for a β = 0.175 spoke cavity. The cavity design is complete and its construction is under way. Together with a power coupler whose design is almost complete,[9] this system could be operated on the LEDA accelerator. If funded, this could be the first demonstration of a spoke cavity with an accelerator beam.

The main design effort involved optimizing the rf properties of the structure. These properties are the quality factor (Q) (to maximize); the rf losses on the surface (P_{cav}) (to minimize); the ratios of peak-surface fields to the accelerating field (E_{peak}/E_{acc}, B_{peak}/E_{acc}) (to minimize); and the velocity acceptance, which is characterized by the transit time factor (T) (to maximize). The

shapes of the pillbox end-walls and the internal bar(s) influence these quantities. Different from elliptical structures, spoke cavities are full three-dimensional structures that need to be modeled without assuming rotational symmetries. In the last few years, we acquired new design tools that allow integrated three-dimensional rf, mechanical, and thermal analyses. The predictive power of these tools has been demonstrated for the APT project where elliptical cavities and rf-power couplers have been designed and successfully put into operation without major low-power modeling efforts.[10]

In spoke cavities, the electric and magnetic field are well separated, which allows for independent optimization of the shape of the high-magnetic-field and high-electric-field regions. Typically, peak-surface-field ratios get higher with lower β, but these cavities, for a given accelerating field, have ratios comparable to those of higher-β elliptical cavities. The optimization for the lowest peak fields in the structure is done by appropriately shaping the spoke cross section and the end-wall. At the same time, the optimization procedure needs to provide the largest possible acceleration gap and minimize the rf-surface losses.

The electromagnetic properties are not the only issue in designing these resonators. Mechanical properties, thermal control, fabrication, and tuning issues have a strong impact on the final design. We used geometrical models that were common to the electromagnetic and all other designs so that these issues could be addressed in parallel. The final design details included optimized rf properties; specification of external attachments that met all rf-requirements; the capability of the cavity to sustain expected mechanical loads under vacuum (i.e., with appropriate stiffening rings, which were also provided by this design procedure); and the provision of the required tuning range for operation under various operation scenarios.

Fig. 4 shows two cut-away views of the final geometry of the β = 0.175, two-gap, 350-MHz cavity. The spoke shape is fat and round at the connection to the cavity body to minimize peak magnetic fields and losses. The spoke is flat and wide at the aperture to minimize the peak electric fields, and thus field-emission effects are reduced. The cavity end-walls are not flat but extend beyond the gap-to-gap length of the cavity. This minimizes the surface magnetic fields and provides a good tuning range for the structure. Two rings, which are also used to move the end-walls for tuning, stiffen the cavity. The disadvantage of this end-wall shape is that the physical length of a spoke resonator is larger than the active length. This results in a reduction of the real-estate gradient as compared to elliptical cavities. A
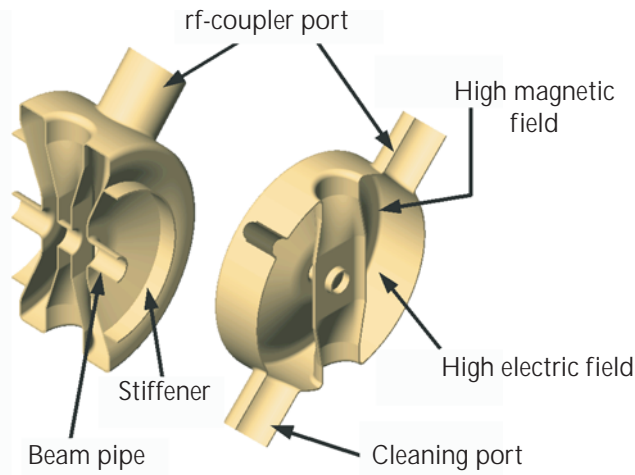
↑ **Fig. 4.** *The final geometry for the β = 0.175, two-gap, 350-MHz spoke cavity is shown in these two cut-away views. The shape of the cavity and the spoke, the position of the ports, and the location of the stiffening rings are the result of a combined electromagnetic, mechanical, and thermal evaluation of the structure.*

small port for an rf pickup and two larger ports are also shown in Fig. 4. One of the large ports is not required for the operation of the cavity, but it is important for the thorough cleaning of the rf surfaces.[11] The other large port is the rf-power feed port where the input power coupler will be attached.

The most challenging part of the spoke-cavity design for practical application is to determine the position of the input-power-coupler port. For efficiency, spoke cavities need much smaller beam-pipe sizes than elliptical cavities, which require that an rf feed be directly attached to them. The port opening and the coupler itself do affect the cavity frequency and thus had to be considered during the cavity design.

Table 1 compares some rf parameters for the APT β = 0.64 elliptical cavity and the final design of the β = 0.175 spoke cavity. These results show that spoke cavities are fairly effective structures. Their peak field ratios are comparable to the ratios in the β = 0.64 elliptical cavities. This indicates that comparable accelerating gradients should also be obtainable.

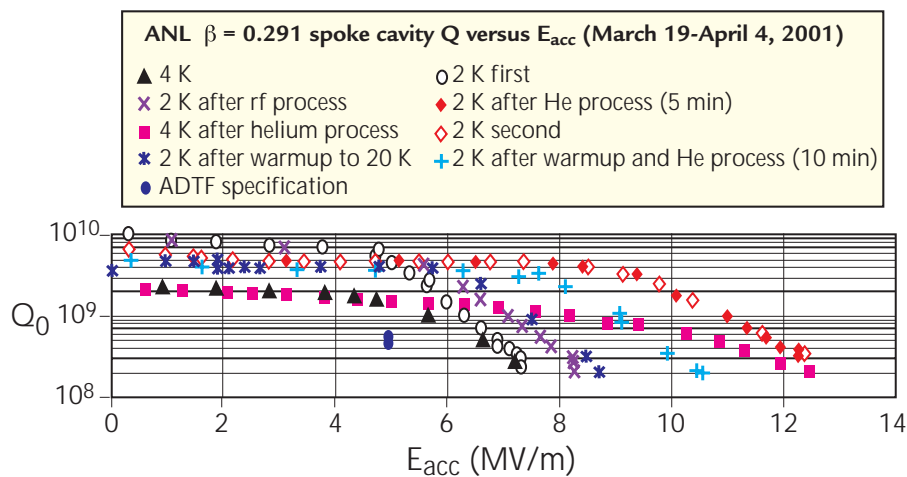| Table 1. rf parameter comparison between β = 0.175 spoke resonator and the β = 0.65 elliptical cavity		
	β = 0.175	**β = 0.64**
Q_o	1.21×10^9 (4 K)	9.4×10^9 (2 K)
T	0.7765	0.650
E_{peak}/E_{acc}	2.82	3.38
B_{peak}/E_{acc}	74 G/MV/m	70 G/MV/m
P_{cav} at 7.5 MV/m	9.32 W	10.45 W

Demonstrating the Competitive Performance of Spoke Resonators

Laboratory tests were done at Argonne National Laboratory and at Los Alamos National Laboratory[12] that demonstrated that these cavities can provide accelerating fields in the low-velocity regime that are comparable to the performance of elliptical cavities in the higher-velocity regime (Fig. 5). A spoke cavity similar to our design was tested at both laboratories and achieved accelerating gradients of more than 10 MV/m after cleaning techniques were optimized to the spoke geometry. The tests were also used to benchmark our electromagnetic- and mechanical-simulation tools for these more complex three-dimensional geometries.

Conclusion

Our design work for a β = 0.175 spoke cavity with all provisions for operations in a high-current-accelerator environment shows that for these structures a performance comparable to that of higher-β structures can be achieved. This expands the velocity range over which the advantageous SCRF technology is applicable.

ANL β = 0.291 spoke cavity Q versus E_{acc} (March 19-April 4, 2001)

▲ 4 K
✕ 2 K after rf process
■ 4 K after helium process
✳ 2 K after warmup to 20 K
● ADTF specification
○ 2 K first
◆ 2 K after He process (5 min)
◇ 2 K second
➕ 2 K after warmup and He process (10 min)

↑ **Fig. 5.** *An ANL β = 0.29 spoke cavity at 4 K reached a 12.5-MV/m accelerating gradient in a vertical test in the LANSCE-1 SC Laboratory.*[13]

References

1. Jefferson Laboratory; http://www.jlab.org.
2. Advanced Accelerator Applications/Accelerator Production of Tritium; http://aaa.lanl.gov.
3. Spallation Neutron Source; http://www.sns.gov/.
4. TESLA; http://www.tesla.de/.
5. Argonne Tandem Linac Accelerator System (Argonne National Laboratory); http://www.phy.anl.gov/atlas/index.html.
6. Rare Isotope Accelerator (Argonne National Laboratory); http://www.phy.anl.gov/ria/index.html.
7. K.W. Shepard *et al.*, "SC Linac Driver for a Rare Isotope Facility," in *Proceedings of the 9th Workshop on rf Superconductivity* (Santa Fe, New Mexico, 1999), http://www.phy.anl.gov/ria/techasp/RIA_Driver_Overview.pdf.
8. J.R. Delayen *et al.*, "Prototype 350-MHz Niobium Spoke-Loaded Cavities," in *Proceedings of the 1999 Particle Accelerator Conference* (IEEE, 1999), 955; http://accelconf.web.cern.ch/AccelConf/p99/PAPERS/MOP123.PDF.
9. E.N. Schmierer *et al.*, "Design of the Spoke Cavity ED&D Input Coupler," Los Alamos National Laboratory report LA-UR-01-4889; http://laacg1.lanl.gov/scrflab/pubs/coupler/la-ur-01-4889.pdf.
10. E.N. Schmierer *et al.*, "Results of the APT rf Power Coupler Development for Superconducting Linacs," Los Alamos National Laboratory report LA-UR-01-4890; http://laacg1.lanl.gov/scrflab/pubs/APT/la-ur-01-4890.pdf.
11. F.L. Krawczyk *et al.*, "Design of a β = 0.175 2-Gap Spoke Resonator," Los Alamos National Laboratory report LA-UR-01-4989; http://laacg1.lanl.gov/scrflab/pubs/spoke/la-ur-01-4989.pdf.
12. T. Tajima *et al.*, "Evaluation and Testing of a Low-β Spoke Resonator," Los Alamos National Laboratory report LA-UR-01-3141; http://laacg1.lanl.gov/scrflab/pubs/ANL/LA-UR-01-3141.pdf.
13. LANSCE-1 SC Laboratory, http://laacg1.lanl.gov/scrflab/.

Research Highlights

Advances in Low-Level Radio-Frequency Control System Design

A.H. Regan, S.I. Kwon, M. Prokop, T.S. Rohlev, Y.-M. Wang (SNS Division),
D.W. Thomson (LANSCE Division)

Staff members from the Spallation Neutron Source (SNS) Division and the Los Alamos Neutron Science Center collaborated on an upgrade of the low-level radio-frequency control system (RFCS), which performs a number of critical functions on the Low-Energy Demonstration Accelerator (LEDA). The RFCS has gone through several upgrades since 1988 when it was first developed for the Ground Test Accelerator (GTA). It was upgraded for the Accelerator Production of Tritium Project and is now being used on LEDA and modified further for the SNS at Oak Ridge National Laboratory. Each subsequent upgrade took advantage of state-of-the-art components and digital technology, allowing researchers to reduce the RFCS to a quarter of the size of its predecessors, yet with more features.

The RFCS primarily monitors and controls the radio-frequency (rf) fields in the accelerator cavity to within specified amplitude and phase requirements (field control functions); monitors the resonance frequency of the rf field in the accelerator cavity and takes actions to move the resonance frequency to the operating frequency (resonance control functions); monitors the high-power rf distribution system and quickly alerts the machine protection system of a fault or arc condition (high-power-protection functions); and distributes a phase-stable rf reference signal throughout the accelerator (frequency reference systems). The goal of our work is linked to the primary purpose of this unique system—that is, to minimize deviations in the rf field in the accelerator cavity from the operator-defined set points. The rf field must be at the right phase and amplitude to efficiently move beam through the accelerator.

System Implementation

Fig. 1 shows a block diagram of a typical RFCS. The dotted lines represent different VXIbus modules that perform the functions described above. The three klystrons used for the LEDA radio-frequency quadrupole have a single RFCS housed in a dedicated VXIbus "crate" that serves as a local processor for data-acquisition,
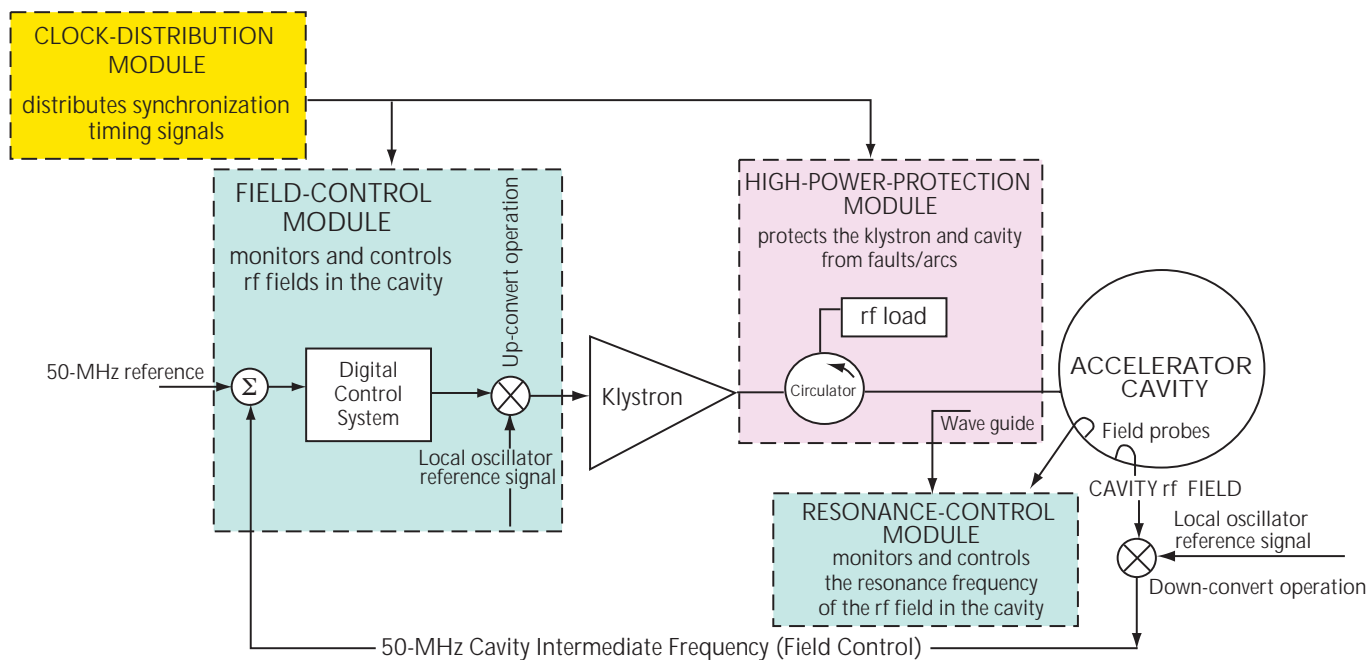
↑ **Fig. 1.** *The colored blocks represent functions performed by the RFCS control modules. The clock distribution receives a 2.5-MHz reference signal; produces local oscillator (LO) signals (352.5 MHz and 755 MHz), an intermediate-frequency field, and an analog-to-digital-converter frequency, all of which are needed to down-convert rf frequencies and to sample I/Q (in-phase and quadrature) signal components; and translates timing signals from the master timer for synchronizing sampling data.*

system-monitoring, and real-time-event-processing tasks. The VXIbus interfaces with the experimental physics and industrial control system (EPICS) to send and receive information about the way the RFCS controls the in-phase and quadrature (I/Q), rather than the amplitude and phase, components of the accelerator cavity rf field. The I/Q field control was originally suggested and implemented on the GTA's low-level RFCS. It has since become the standard around the world.

Field- and Resonance-Control Functions

The master-timing system, which serves as the source of all precision timing signals for the RFCS, transmits synchronous data-sampling signals to the clock-distribution module (CDM), which then passes these signals on to the other RFCS control modules. They use these signals to synchronously collect data on the system's operations. The field-control module continuously monitors the amplitude and phase of the rf field throughout the entire accelerator system on a pulse by pulse basis and then takes the necessary actions to compensate for any rf field perturbations detected. The resonance-control module continuously monitors the actual resonance frequency within the accelerator cavity via field probes and moves it to the set operating resonance frequency, and it maximizes the rf power that is amplified by the klystrons and then transferred to the accelerator cavity. It does this by calculating the difference between the design and actual resonance frequency of the cavity and then outputs the frequency error to EPICS, which forwards the error to the appropriate cavity tuner system. Sample data are sent to EPICS for diagnosis about the RFCS and its associated functioning. EPICS is used by the operators in the control room to monitor different parts of the RFCS, but the RFCS takes the appropriate actions, for example, performs calculations and corrects rf/resonance field perturbations, to keep the system running at the operator-set field frequencies.

High-Power-Protection Functions

The high-power protection module (HPM) protects the klystron and accelerator cavity from high-power rf faults that may occur by monitoring the system for excessive rf power at various test points and for arcs internal to the accelerator cavity. The HPM interfaces with the "outside world" for quick-response actions via a control system

that provides the HPM with rf input and via the machine protection system that terminates the beam. If a fault condition is detected, the HPM quickly shuts down the rf carrier and alerts the machine protection system, which then terminates the beam.

Frequency Reference System

The purpose of the frequency reference system is to provide a phase-stable frequency reference at each control system. The frequency reference system provides two LO frequencies (352.5 MHz, 755 MHz) and a precision 2.500-MHz clock reference to the RFCS. The two LO frequencies are used to down-convert the 402.5-MHz (352.5 MHz + 50 MHz) and 805-MHz (755 MHz + 50 MHz) signals to a 50-MHz intermediate frequency in the accelerator cavity. The resulting 50-MHz signal is brought back to the RFCS for digitization and processing. The 2.500-MHz signal is used as the reference for the CDMs and is synchronized to the LO frequencies at each RFCS subsystem.

Great Strides Using Digital Technology

The field and resonance control modules rely on fast Complex Programmable Logic Devices (CPLDs) and digital signal processors (DSPs) optimized for real-time signal processing. The resonance frequency in the accelerator cavity is obtained from DSPs by sampling the forward and the transmitted rf-field signals from the cavity and calculating the cavity's rf-field admittance. The resulting resonance-frequency error is used to drive whatever type of resonance controller is in use, for example, a water-cooling method for normal conducting cavities or a mechanical tuner for superconducting cavities. The CPLDs perform the complex control functions required to keep the cavity field at its operator-defined set point. Operator interface with the HPM also provides the operator with the ability to control rf thresholds and the time duration of allowable fault conditions within the high-power rf distribution system. The GTA's low-level RFCS did not perform the HPM functions that the current RFCS upgrades do and yet it still consisted of three crates of electronics. By the end of the GTA program, we had incorporated some digital technology, which allowed us to reduce the size of the RFCS to two full crates. By continuing to take advantage of digital technology, we have made great strides in further size reductions with enhanced performance at reduced cost.

Research Highlights

## Observation of an Intense Electron Cloud at the LANSCE Proton Storage Ring

R.J. Macek, A. Browman, D. Fitzgerald, R. McCrady, T. Spickermann, T.S. Wang (LANSCE Division)

A strong, fast, transverse instability has long been observed at the Los Alamos Neutron Science Center Proton Storage Ring (PSR) where it has become a limiting factor on peak intensity. Available evidence, based on measurements of the unstable motion of the proton beam, is consistent with an electron-proton two-stream instability. A long-standing puzzle has been the origin of sufficient electrons to account for the threshold-intensity characteristics. The well-known sources, such as residual gas ionization, beam losses, electrons from the stripping process, and secondary emission from the stripper foil, are orders of magnitude too small to account for the threshold-intensity characteristics unless a large fraction of them is accumulated for many turns. Neuffer[1] postulated that beam leaking into the gap between successive passages would trap sufficient electrons. However, measurements of the beam in the gap for normal conditions gave us a number that was an order of magnitude (or more) smaller than needed to trap sufficient numbers of electrons to explain the instability threshold intensity.

In 2001, new experiments using retarding field analyzers (RFAs) and a newly developed electron-sweeping detector have led to a much better understanding of the origin and characteristics of the electron cloud in PSR. Measurements with these diagnostics have shown that a large flux of electrons strikes the beam chamber walls near the end of the beam pulse and that the resulting soft electrons decay slowly with time after passage of the beam pulse. Sufficient numbers survive the gap to account for the instability threshold, but we are assuming that the measurements made in the one section with the electron-sweeping detector are typical of the entire PSR.

Retarding-Field-Analyzer Diagnostic

A schematic diagram of the RFA developed at Argonne National Laboratory[2] and deployed in several locations in the PSR is shown in Fig. 1. Electrons moving toward the wall enter the detector through small slots in the beam-pipe wall and encounter two grids: (1) a grounded screen that shields the collector from signals induced by the beam and (2) a repeller grid that only allows
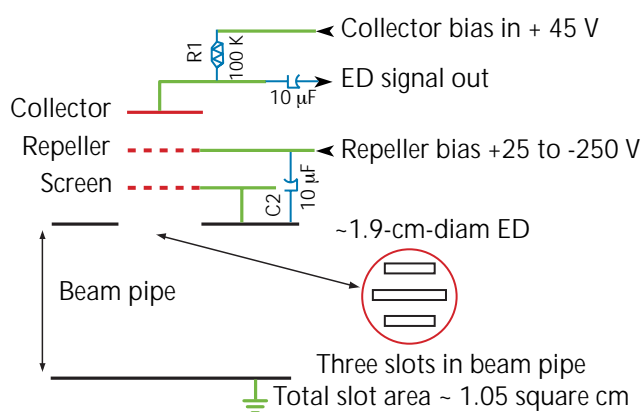
↑ **Fig. 1.** *Schematic sketch of the RFA used at the PSR. (ED is electronic detector, C1 and C2 are capacitors, and R1 is a resistor.)*

electrons of energies greater than the grid bias to pass to the positively bias collector. The PSR collector signal is connected to high-speed electronics. With this device, the flux, energy spectrum, and time structure of the electrons striking the collector can be measured. In Fig. 2, signal samples obtained from a detector located in a relatively low-loss straight section and for stable beams are plotted. Signals for several values of the repeller voltage are shown in proper time relationship to the beam-current signal. The detectors collect electrons with energies higher than the value set by the negative repeller voltage, thus providing data on the cumulative energy spectrum. In general, the higher-energy electrons are in a shorter
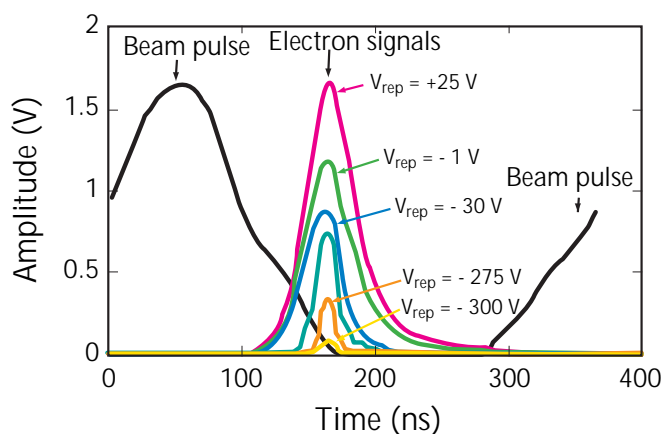
↑ **Fig. 2.** *Signals from the RFA in Section 4 of the PSR for an 8-µC/pulse beam intensity in proper time relationship to the beam pulse from a nearby wall current monitor.*

pulse. The long tails on the signal for a +25-V repeller setting undoubtedly include secondary and tertiary electrons produced by the impact of higher-energy electrons. Note that the tail extends into the start of the next beam-pulse passage.

The signal level at the peak implies ~ 400 to 500 $\mu A/cm^2$, which is a large flux of electrons. In fact, it is 5 orders of magnitude higher than the ~ 2 nA/cm^2 expected from residual gas ionization, assuming that the electrons generated in one passage of the beam pulse emerge in about a 40-ns pulse at the end of each beam pulse. The characteristics of this large flux of electrons are consistent with that expected from beam-induced multipacting on the trailing edge of the beam pulse.[3]
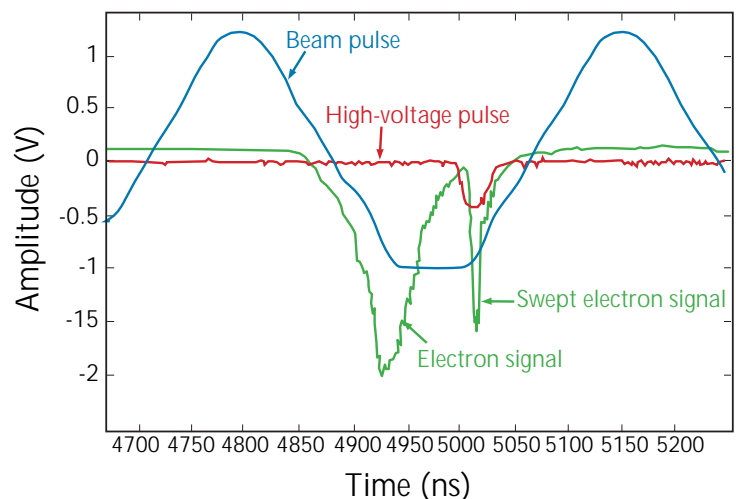
Electron-Sweeping Detector

Electrons striking the wall during the multipacting process pass from wall to wall in a few nanoseconds and therefore do not spend enough time interacting with the beam to be effective in causing the instability. However, low-energy electrons that are created by the secondary emission at the very end of the beam pulse and that survive passage of the gap will be captured by the next beam pulse and will oscillate against the proton beam during the entire passage of the beam pulse. These electrons, which may cause the instability, are not measured directly by the RFA signal. The electron-sweeping detector shown in Fig. 3 was designed to measure the electrons left in the pipe.[4]

The concept is to use a pulsed electrode opposite a large-area RFA to sweep electrons from a good fraction the pipe into the RFA detector where they are collected. The timing of the short (~ 20-ns) pulse on the electrode selects the sampling time in the gap. The larger aperture of the entrance to the RFA will give a sensitivity that is ~ 8 times higher than the other RFAs in use at the PSR. Typical signals from the electron-sweeping detector are shown in Fig. 4. The blue curve is the beam pulse, the green curve is the signal from the electron-sweeping detector, and the red curve is the high-voltage pulse applied to the sweeper. These are shown in proper time relation with the beam pulse. The prompt electrons come out at the end of the beam pulse, and the detector functions as a large area RFA until the high-voltage pulse arrives. The swept-electron signal at the end of the gap is narrow, as expected, but with a tail that we do not completely understand but which is reduced by a modest repeller voltage.
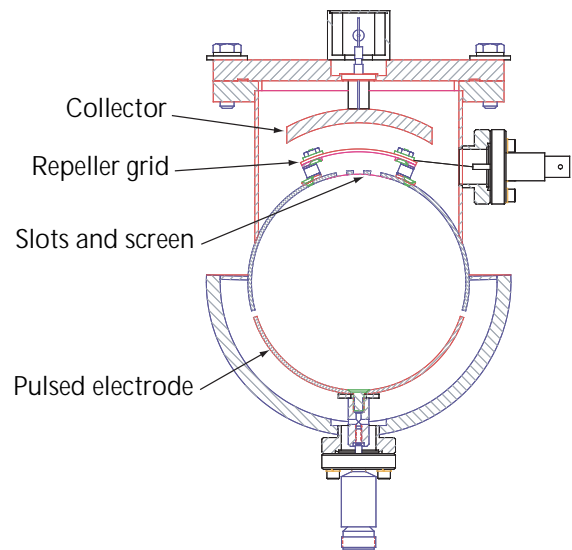

↑ **Fig. 3.** *Cross section of the electron-sweeping detector.*

↑ **Fig. 4.** *Signals associated with the electron-sweeping detector shown in proper time relationship with the beam pulse.*

With the sweeper it was possible to measure electrons in the pipe as a function of time after the passage beam pulse. By timing the high-voltage pulse to the sweeper electrode after the last pulse in the PSR at extraction, we can measure electrons well beyond the usual 100-ns gap. As can be seen in Fig. 5, where both the voltage peak and the integral of the swept-electron peak have been plotted against time from the end of the beam pulse, either of these signals has a long exponential tail, which is still observable after 1 ms.
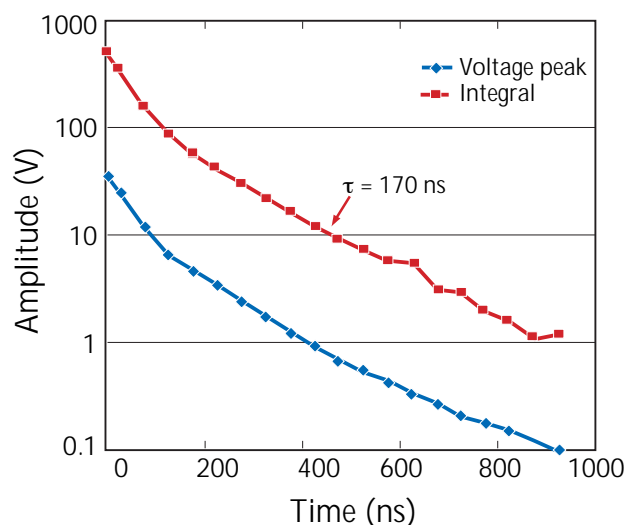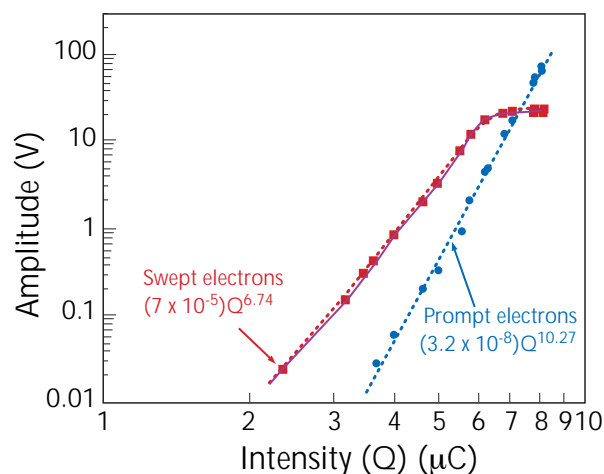
↑ **Fig. 5.** *Electrons in the beam pipe plotted as a function of time after the end of the beam pulse.*

↑ **Fig. 6.** *Signal amplitude for swept and prompt electrons plotted as a function of beam intensity.*

The time constant is ~ 170 ns and implies a high reflectivity for the low-energy electrons that are left in the pipe. A simple calculation shows that a reflectivity of ~ 0.5 is needed to account for the presence of electrons with energies of 2 to 5 eV (i.e., the peak energy of true secondary electrons). This surprising result is consistent with new CERN (the European Laboratory for Particle Physics) measurements of the secondary emission yield down to 4-eV incident electrons.[5]

The integral at the end of a 100-ns gap implies a lower limit of ~ 1.5 % on the average beam neutralization from the electrons that survive the gap. This is in the range needed to explain the instability threshold in the simple centroid model for the two-stream electron-proton instability.

With the electron-sweeping detector, we could simultaneously measure the prompt and swept electrons (at the end of the gap) as a function of intensity as shown in Fig. 6. In this experiment, the only parameter that was not held constant was the intensity (Q), which we varied by moving the stripper foil to inject less beam. These data show that the prompt electrons varied as the tenth power of intensity over the entire range. The swept electrons at the end of the gap varied somewhat more slowly as the seventh power but saturated above 5 to 6 μC/pulse. This high-intensity region is the region of greatest interest for PSR upgrades and could explain why the threshold intensity as a function of buncher voltage does not saturate in this region. Based on this data, the fractional beam neutralization from the electrons surviving the gap is roughly constant in the region above 5 μC/pulse.

Why do the swept electrons saturate? One possible explanation is that the space-charge forces in the electron cloud in the beam-free region will tend to cause more rapid expansion of the cloud, which counters the rapid buildup of electrons fed into the gap by the trailing-edge multipactor. It would saturate when these two processes are in equilibrium. The Lawrence Berkeley National Laboratory simulation code could be used to check this idea.[6]

Suppression of Electron Generation

Previous work in a straight section of the PSR has shown that prompt electrons are reduced by a factor of 100 or more by coating the vacuum surfaces with a thin layer (~ 700 Å) of titanium nitride (TiN). During 2001, the use of weak magnetic solenoid fields was tested in a short (~ 0.5-m) region of Section 9 of the PSR with the result that a 20-G field reduced the prompt-electron signal by a factor of ~ 50 as shown in Fig. 7.
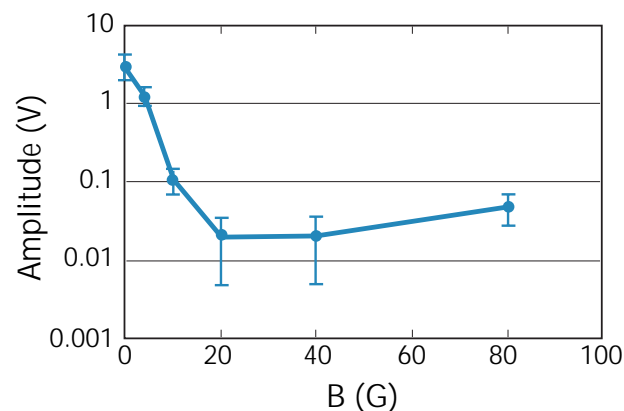
↑ **Fig. 7.** *Effects of a weak solenoid field (B) on the amplitude of the prompt-electron signal from an RFA in Section 9 of the PSR.*

Conclusion

The wealth of data collected on the electron cloud using the RFA and electron-sweeping detector has provided important new insights into the generation of the electron cloud in the PSR. The results support the hypothesis that trailing-edge multipacting creates most of the prompt-electron signal observed in straight sections of the PSR. Data from the electron-sweeping detector showed that electrons decay slowly after passing the gap and that sufficient electrons survive the gap to account for the observed instability thresholds. These results resolve a major puzzle in explaining the PSR transverse instability as a two-stream instability. TiN coatings (where applied) have greatly reduced the prompt-electron signal and, as such, offer the prospect of a cure with no increase in losses. Likewise, the use of weak solenoid magnetic fields significantly reduced the prompt-electron signal. Solenoid windings can be used in straight sections of the PSR, but these would not be effective in dipole or quadrupole magnets.

References

1. D. Neuffer *et al.*, "Observations of a Fast Transverse Instability in the PSR," *Nuclear Instruments and Methods A* **321**, 1 (1992).
2. R. Rosenberg and K. Harkay, "A Rudimentary Electron Energy Analyzer for Accelerator Diagnostics," *Nuclear Instruments and Methods A* **453**, 507 (2000).
3. R. Macek, "Sources of Electrons for Stable Beams in PSR," PSR Technote 00-10, (November 2, 2000).
4. A. Browman, "Design Report on Electron Sweeper," memo to R. Macek, March 25, 2001.
5. N. Hilleret *et al.*, "A Summary of Main Results Concerning the Secondary Emission Yield from Copper," Large Hadron Collider Project report 472 (2001).
6. M. Furman and M. Pivi, "Simulation Results for the Electron Cloud at the PSR," in *Proceedings of the 2001 Particle Accelerator Conference,* 707 (2001).

Research Highlights

Klystron Development for Jefferson Laboratory

G.O. Bolme (LANSCE Division)

The Spallation Neutron Source (SNS) program at the Jefferson Laboratory requires a source of 805-MHz, 1-MW radio-frequency power to develop and test the superconducting cavities and power couplers for the high-energy sections of the accelerator. Spare components from the Los Alamos Neutron Science Center (LANSCE) accelerator could be used to assemble a klystron-based amplifier system to meet this requirement. A quid pro quo was reached between the Jefferson Laboratory and LANSCE to build this new amplifier system for the Jefferson Laboratory in exchange for support in rebuilding two klystron tubes of a similar type. It is understood that the depletion of the LANSCE system spare parts will be minimal with no reduction in the number of spare klystrons and modulator tanks available in the sectors to support accelerator operations.

Klystron Amplifier

The plan for providing Jefferson Laboratory with a klystron-based amplifier system and a modulator tank was based on converting a salvaged modulator tank with a Litton 425-MHz klystron to an 805-MHz-modulator and klystron amplifier system. The salvaged 425-MHz klystron and modulator amplifier was from the Accelerator Test Stand program, for which it was built with a LANSCE modulator design. As such, only minor modifications were required to convert this unit to a modulator for the 805-MHz amplifier system.

Because we have very few spare Varian VA-862A klystrons, the Jefferson Laboratory system will be based on one of our spare Litton L-5120 klystrons. The system will use up our spare solenoid assembly; therefore, a complete set of solenoid coils is being purchased, and a spare solenoid assembly will be constructed from these coils and available spare parts.

The initial schedule called for completion and delivery of the klystron and modulator to Jefferson Laboratory during February 2002, and the equipment will be on loan to Jefferson Laboratory for approximately one year.

Conversion of a 425-MHz-modulator and klystron-amplifier system started in July 2001. The 425-MHz klystron and modulator were moved to the Equipment Test Laboratory (ETL) where the klystron and solenoid assemblies were removed from the modulator tank. The modulator components were pulled out of the tank and examined for necessary modifications. New lids were fabricated for the tank to accommodate the 805-MHz tube socket and solenoid assembly. The modulator tank was then rebuilt with the replacement hardware and with an available Litton L-5120 klystron. Near the end of testing at Los Alamos National Laboratory, we still had concerns about unexpected and intermittent faults; therefore, a unit was sent to Jefferson Laboratory in December 2001 from our Sector H spares. Testing of the conversion klystron and modulator amplifier was completed, and it then replaced the Sector H unit sent to Jefferson Laboratory. The klystron and modulator tank installed at Jefferson Laboratory is shown in Fig. 1.

↑ *Fig. 1. The SNS program requested that Jefferson Laboratory make the test stand operational. The support electronics for the klystron, modulator, and solenoid systems were assembled from the spare equipment modules of the LANSCE accelerator. The support electronics included two racks of electronic modules and all interconnecting wiring as shown in Fig. 2.*

The SNS program requested that Jefferson Laboratory make the test stand operational. The support electronics for the klystron, modulator, and solenoid systems were assembled from the spare equipment modules of the LANSCE accelerator. The support electronics included two racks of electronic modules and all interconnecting wiring as shown in Fig. 2.

A water manifold for the klystron, modulator, and solenoid systems was also built in the ETL as shown in Fig. 3. This water manifold included the required distribution piping, water-flow gauges, flow interlocks, temperature gauges, and hose disconnects.

↑ **Fig. 2.** *The 805-MHz klystron support electronics are the two racks on the left.*
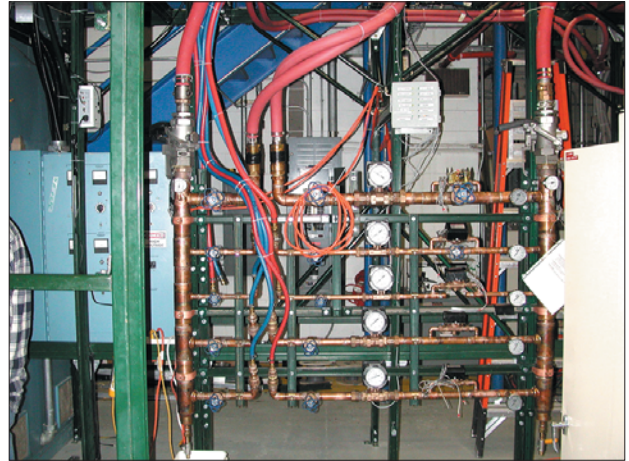
↑ **Fig. 3.** *The 805-MHz klystron water manifold.*

Research Highlights

LANSCE High-Voltage System

G.O. Bolme (LANSCE Division)

The Los Alamos Neutron Science Center (LANSCE) radio-frequency (rf) high-voltage system includes components that convert alternating current (ac) to direct current (dc) used to store energy, which powers the 201-MHz final power amplifier (FPA) and the 805-MHz klystron amplifier. This ac-to-dc conversion is required because the 201-MHz FPA needs approximately 28-kV dc bias and the 805-MHz klystron needs approximately 84-kV dc bias to deliver their respective output powers. Because these are pulsed rf amplifiers, the high-voltage systems make it possible to draw ac power from the utility substation at a relatively smooth average power and to deliver intense pulses of dc power to the amplifier systems corresponding to the accelerator beam pulses.

All of the high-voltage systems consist of the following basic components: a vacuum breaker with controls, an Inductrol voltage regulator with controls, a transformer rectifier, a capacitor bank for energy storage, a high-voltage crowbar system, and other support components to control and protect the system.

At the end of 2001, all of the major components were in operation far beyond their expected lifetimes. During the past few run cycles, several failures were encountered and some of these were indicative of the end of life of these systems. Several upgrades have been or are being completed to preclude some of the failure modes and preventive maintenance programs have been initiated to extend some of the system lifetimes.

High-Voltage Pads

The Inductrol voltage regulators and transformer rectifiers are large oil-filled units located on concrete pads north of the accelerator building (Fig. 1). These units were purchased and installed just before 1970 and have an expected lifetime of approximately 20 years, depending primarily on the condition of the insulation paper used in the transformer windings. As a result, the performance and the lifetime of the unit depend on the condition of the transformer oil and the insulation paper.

The capacity of the unit to operate without breakdown is a function of the voltage standoff of both the oil and

↑ *Fig. 1. A LANSCE high-voltage pad.*

the insulating paper. The voltage standoff can be reduced by the moisture content of the oil and other contaminants that build up in the oil during use. The moisture and acids in the oil are also the primary contributors toward breakdown of the insulating paper. Extending the life of these units necessarily starts with controlling the condition of the transformer oil.

Since the time of purchase, little had been done to maintain the units until 1995. In 1995, the oil was tested on all of our units; and in 1998, a preventive maintenance program was started to regenerate the oil back to a nearly new quality. The preventive maintenance program consists of processing the oil in four to five of the units each year, concentrating on those units in most need of improvement. This processing is done by SD Myers, Inc., using a processing plant contained in a mobile-truck unit. The processing unit is connected to our transformer unit and circulates the oil through the processing plant until the oil quality is reclaimed. Fig. 2 shows the on-site equipment for oil processing.

Since the original installation of the transformer units, five of our units acquired PCB (polychlorinated biphenyl) contamination, probably as a result of partial refilling with PCB oil. The PCB-contaminated oil creates a situation where we cannot repair any interior components in the case of a failure. Two such failure cases have occurred since January 1999 in our non-PCB operational units. As a result, we have refilled those five units with non-PCB oil, and as of 2000, all of our transformers have been certified as non-PCB units.

↑ **Fig. 2.** *Mobile-truck used for on-site transformer-oil processing.*

Another preventive maintenance program was initiated in 2001 to deal with the detrimental effect of having moisture in the transformer oil. When the transformers are in service, there is a nitrogen gas blanket put over the oil and sealed into the unit. If the pressure seals on the units deteriorate, the units then breathe atmosphere in and out as the oil expands and contracts with operating temperature. This breathing process also brings atmospheric moisture that is subsequently absorbed by the oil. Over time, the seals on the units and the pressure relief gauges have become suspect due to age. All of the pressure gauges were replaced during the 2001 maintenance outage, and the new gauges permitted pressure monitoring to the accuracy necessary to confirm the integrity of the seals. Numerous units were found to be leaking, and the seals have been retightened and resealed.

Capacitor Failures

During the accelerator run cycle of 2000, eight catastrophic capacitor failures occurred with seven of them, resulting in capacitor room fires. The failures and subsequent capacitor room cleanups were a significant source of accelerator downtime for that cycle.

Analysis of possible underlying causes pointed to the use of an uneven pulse train (i.e., a pulse sequence with some pulses removed, resulting in a pulse-rate stutter) in the pulse rate for the 805-MHz accelerator sections. The uneven pulse train resulted in a voltage ripple at various frequency components that are undesirable to the operation of capacitors. As a result, the accelerator is now being operated with only even-pulse trains and the resulting capacitor failures have been minimized. Even though the even-pulse rate has minimized the failures, the failures of 2000 have stressed the remaining operational capacitors, which are already past their rated ten-year lifetime. For this reason, capacitor purchases and preventive maintenance have been undertaken to minimize future problems.

The capacitor rooms of Sectors B and C experienced more than one failure during the 2000 run cycle and were assumed to be the most stressed. During the maintenance outage of 2001, the capacitors in these sectors were "hi-potted" (i.e., charged individually with a low-power voltage source) to 20% above their rated specification to identify those near failure. By charging each capacitor individually, a capacitor fault could be identified without the catastrophic failure associated with dumping the stored energy of the entire capacitor bank into a single fault. Any capacitor showing a fault was removed from the capacitor bank. The capacitors in Sector B were then replaced with newer salvaged capacitors (rated at 60 kV) from the Ground Test Accelerator program.

In 2001, 220 new capacitors were purchased. These capacitors have all been hi-pot tested to 50% over their rated voltage, and the older capacitors will be replaced in Sectors C, D, G, and H. The older and more reliable capacitors (i.e., the 1977 version) removed from those sectors are installed in Sectors E and F in place of the less reliable capacitors (i.e., the 1987 version). As we go into the next run cycle, we will have all of our capacitor rooms upgraded to a more reliable configuration, and each capacitor room, with the exception of Sector B, will have capacitors from the same manufactured batch.

Research Highlights

Evaluation of the LANSCE H⁻ Low-Energy-Beam-Transport System for High-Emittance Beams

R.C. McCrady, M.S. Gulley, A.A. Browman (LANSCE Division)

In April 2001, we conducted an investigation designed to discover inadequacies in the low-energy-beam-transport (LEBT) section of the Los Alamos Neutron Science Center (LANSCE) accelerator with regard to the use of H⁻ beams whose emittances are significantly larger than in beams used in production operation. This investigation was motivated by the possibility of using an H⁻ ion source developed at the University of California (UC) at Berkeley for the Short-Pulse Spallation Source (SPSS) project. This ion source produces more beam current, but the beam has a larger emittance than the usual H⁻ beam (called the production beam) delivered to the users. For our investigation, an H⁻ ion source which is used for production beams was slightly modified to produce a beam which was similar to that produced by the UC Berkeley SPSS source. Our investigation was performed as recommended by a Department of Energy review committee for the LANSCE SPSS Enhancement Project.[1]

Low-Energy-Beam-Transport System for High-Emittance Beams

The emittance of the H⁻ beam is the critical parameter influencing whether the LEBT can prepare the beam as required for injection into the LANSCE accelerator. Emittance is essentially the product of a beam's transverse size and its divergence. The emittance cannot be reduced in a beam line, and in reality it increases due to various imperfections in the beam-line components.

Measurements confirmed that the beam produced by the source used in this investigation was similar to that typically produced by the UC Berkeley SPSS source.[2] The conditions under which this investigation was conducted are representative of those that would be encountered if the UC Berkeley SPSS source were to be installed at LANSCE.

The LEBT consists of an 80-kV accelerating column, an 80-keV transport section, a 670-kV accelerating column, and a 750-keV transport section. The LEBT prepares beams in various ways for injection into the linear accelerator (linac) and for delivery to experiments. In addition to the accelerating columns, the LEBT contains bending and focusing magnets, electrostatic beam deflectors, radio-frequency (rf) beam bunchers, and various beam-measurement devices. The total length of the LEBT is approximately 16 m. In addition to the size of the vacuum pipe through which the beam passes, several other factors influence the maximum beam emittance that can be used in this beam line.

- The size of the beam must be kept relatively small while the beam passes through the solenoid magnets in order to avoid magnetic-field aberrations, which cause emittance growth.[3]

- The size of the beam must be smaller than apertures, which are in place to protect certain sensitive devices such as the 670-kV accelerating column, the beam chopper, and the rf bunchers.

- The beam size must be kept small in the beam chopper, which is an electrostatic beam deflector. The beam size dictates how closely the chopper electrode plates can be spaced and thereby influences the voltage required from its power supply to produce the electric-field strength necessary for the deflection.

- The size of the beam must be kept small in the rf bunchers.

- At the end of the LEBT, the beam must have a particular transverse distribution for injection into the linac.

- The magnetic-quadrupole-beam-focusing lenses must be located to allow the above conditions to be realized.

The LEBT was designed for a 1.5-π-cm·mrad beam emittance in the 750-keV transport section. Current production beams typically have emittances near 3.5 π cm·mrad. The 30-mA beam used in this investigation had an emittance of approximately 7 π cm·mrad, i.e., almost five times the design emittance.

Fig. 1 shows the evolution of the beam size through the 750-keV section of the LEBT (i.e., for the beam used in this investigation and for a typical production beam). The beam used in this investigation was larger throughout the LEBT, which resulted in some beam loss. With intensive tuning, 85% beam transmission through the 750-keV transport was achieved, although this tuning sacrificed the optical properties of the beam needed for acceleration and delivery to experiments. (For production operations, 90% beam transmission is typical.)
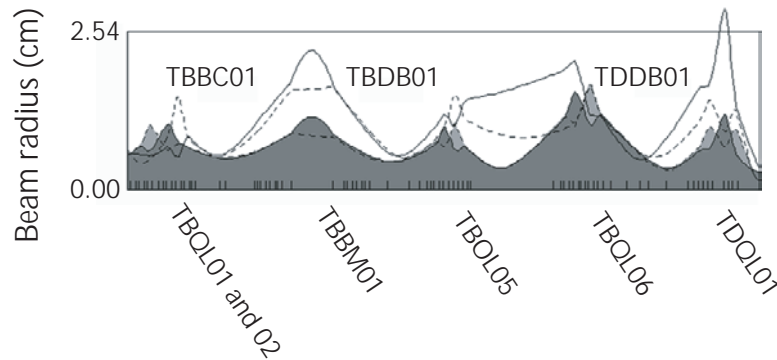
↑ *Fig. 1. Beam radii (in centimeters) are shown along the 750-keV transport section of the LEBT. The solid lines show the horizontal beam size, and the dashed lines show the vertical beam size. The smaller beam, shown in gray, is typical for production operation. The larger beam is that used in this investigation. Locations of selected magnetic components of the beam line are shown along the bottom. TBQL01, TBQL02, TBQL05, and TBQL06 are quadrupole focusing lenses. TBBM01 is an 81° beam-bending magnet. Other significant beam-line components shown are TBBC01 (the beam chopper) and TBDB01 and TDDB01 (two of the rf beam bunchers.)*

Conclusion

The following changes would have to be made to the present LEBT to transport the higher-emittance beams to the entrance of the linac:

- The 80-keV transport section needs to be rebuilt.

  - The rebuilt line needs to be shorter to allow the beam to have a transverse distribution that allows matching into the 750-keV transport.
  - The second solenoid magnet needs to have a larger bore.
  - The beam pipe and other equipment in the vicinity of the beam-emittance-measurement equipment need to be redesigned to prevent stray and deflected beam particles from producing secondary electrons that interfere with the emittance measurement.
  - Emittance-tailoring equipment needs to be installed.

- The high-voltage power supply for the beam chopper needs to be rebuilt to produce higher voltage. The larger beam in the chopper requires the plates to be spaced further apart and therefore requires a greater voltage to produce a given deflection. Furthermore, because the beam is broader downstream of the chopper, a greater deflection (and therefore a greater voltage) is required to separate the chopped from the unchopped beam. Additionally, the apertures associated with the chopper need to be rebuilt to accommodate the larger beam.

- The rf-buncher systems may need to be upgraded to accommodate the larger-diameter beam. This upgrade will require further study.

- The quadrupole lens TBQL06, which consists of four quadrupole magnets, needs to be replaced by magnets that can produce the same focusing strength but with a 50% larger bore.

These changes would allow a higher-emittance H$^-$ beam to be transported to the entrance of the LANSCE linac with an emittance of about twice that of production H$^-$ beams and twice the current. The scope of our investigation did not include acceleration in the linac. If the UC Berkeley SPSS H$^-$ ion source is to be used for production operation at LANSCE, the effects of using higher-emittance beams on the beam spill in the linac must be studied and evaluated carefully before implementation.

References

1. Department of Energy Review Committee TCSM Review of the LANSCE SPSS Enhancement Project, December 2000; Los Alamos National Laboratory report LA-UR-01-6005.
2. R.R. Stevens, Jr., Private communication.
3. R.R. Stevens, Jr., "Beam Optics for the 80-keV Beam Line" unpublished LANSCE memo (December 2000).

Research Highlights

Accelerator Development Studies

C. Pillai, R.C. McCrady, M.S. Gulley (LANSCE Division)

We continue to study the performance of the Los Alamos Neutron Science Center accelerator to improve operations and beam delivery to experimental areas. For this purpose, we undertook the following development activities in 2001. The normal production current to the Weapons Neutron Research Facility (WNR) Target 4 is about 4.5 µA as compared to the possible 10 µA that Target 4 can handle. Measuring the beam parameters for the WNR beam in the accelerator will help us understand the possible causes for this low throughput. Higher levels of beam spill (i.e., beam loss caused by its hitting the beam pipe and spraying away from the main beam) in the switchyard (SY) will limit the increase of the beam current to the Lujan Neutron Scattering Center target in the future. We must understand the possible causes for this spill and devise solutions. Chopping and bunching the beam increases the emittance, which can contribute to beam spill. Improving the chopping mechanism (i.e., by making it faster and cleaner) may help to reduce beam-spill problems. Using a beam chopper instead of the slower ground-level deflector to modulate the beam is another attempt at solving this problem.

WNR Proton Beam Delivery

For normal WNR operation, 3 to 4 micropulses are bunched before injection into the 201-MHz drift-tube section of the linear accelerator (linac). This bunching provides more protons per pulse at Target 4. The longitudinal and transverse acceptance of the machine determines the amount of current that can be delivered to experiments. The beam throughput (i.e., the fraction of the beam that is transmitted through the accelerator) for the WNR beam is measured to be ~ 50% as compared to 80% for the Proton Storage Ring (PSR) beam. This low throughput may be caused by the high peak current for the WNR beam, which is almost three times that of the PSR beam. Optimizing the phases and amplitudes of the bunchers (for longitudinal acceptance) did not greatly improve the situation. We next compared the transverse beam sizes for both the PSR and WNR beams to see whether the low throughput for the WNR beam is caused by beam size. The measurements showed that the transverse beam size in the machine is consistently larger than that of the PSR beam by ~ 25% (Figs. 1 and 2). The measured emittance at the end of the linac was ~ 50% larger for the WNR beam than for the PSR beam—another possible cause for the low beam throughput.

Beam Spill in the Switch Yard and Line D

We are trying to understand the higher levels of beam spill in the switchyard and along the 89° bend in Line D (LD). The spill has changed over the last two years and is getting worse even though the machine spill has not significantly changed. In fact, we are running the LD activation protection system (LDAP2) at a reduced gain; the LDAP5 spill level is also rather high. The activation
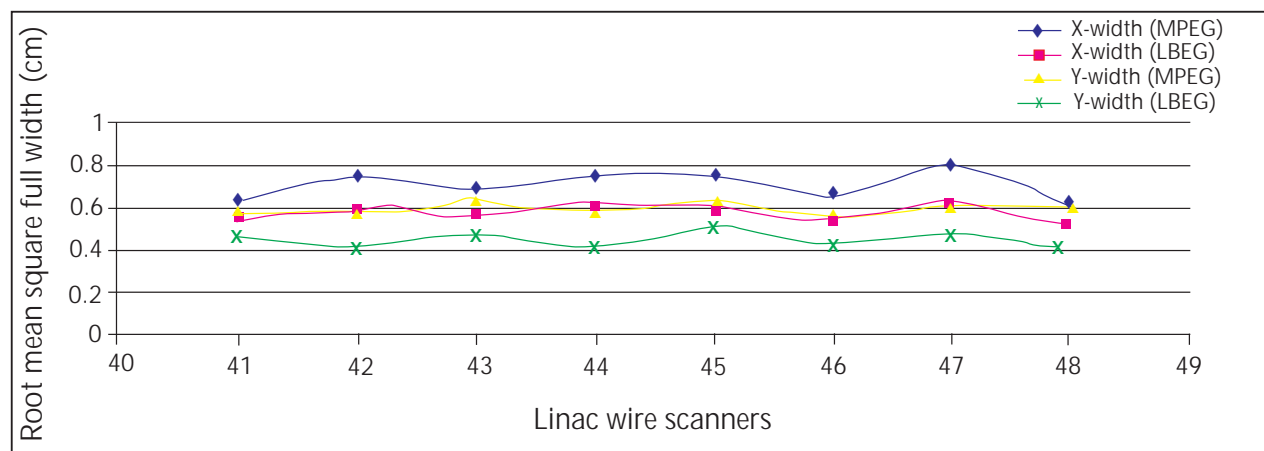
↑ *Fig. 1. Measured beam sizes for PSR (LBEG, long bunch enable gate) and WNR (MPEG, micropulse enable gate) beams in the linac (modules 41-48).*

levels at some locations in SY and LD-N (north) were measured to be ~ 50 mR/h (on contact) soon after beam shut down. We noticed that the activation levels on the left side of the beam are about twice those on the right side. Steering the beam does not improve the situation. Possible causes for the beam spill could include low- and/or high-energy tails, a much too large beam size, and magnetic and/or vacuum stripping.

The low- and high-energy tails were studied with LD phosphors and an LDWS3, which is a wire scanner (WS) used to measure the beam size. These two devices were used to their limit to improve the longitudinal tuning of the machine.

The magnetic fields of the two quadrupoles, LDQD03/04, which are normally off, were varied to produce different beam sizes in LD and to study their effect on the beam spill. We observed no improvement in the beam spill in this study, although we did notice some reduction in beam size at the LDWS05 and LDWS06 locations where the beam spill is high.

Another set of measurements was taken for the 699-MeV beam (chopped) at the same peak and average currents as before. The SY, LD, and PSR-injection (RI) lines had to be re-tuned for this. The emittance of the beam in the machine was very similar to that of the 800-MeV beam. The beam size in the SY and LD was also very similar. However, the spill pattern was nearly a factor of 2 better (Fig. 3). Does this indicate that there is the possibility of field stripping in the 89° bends?
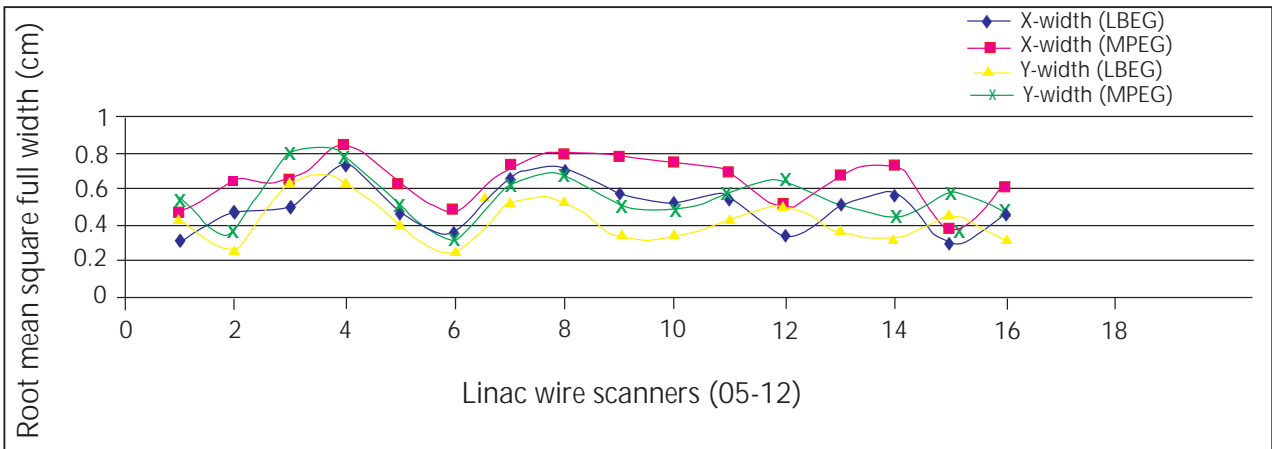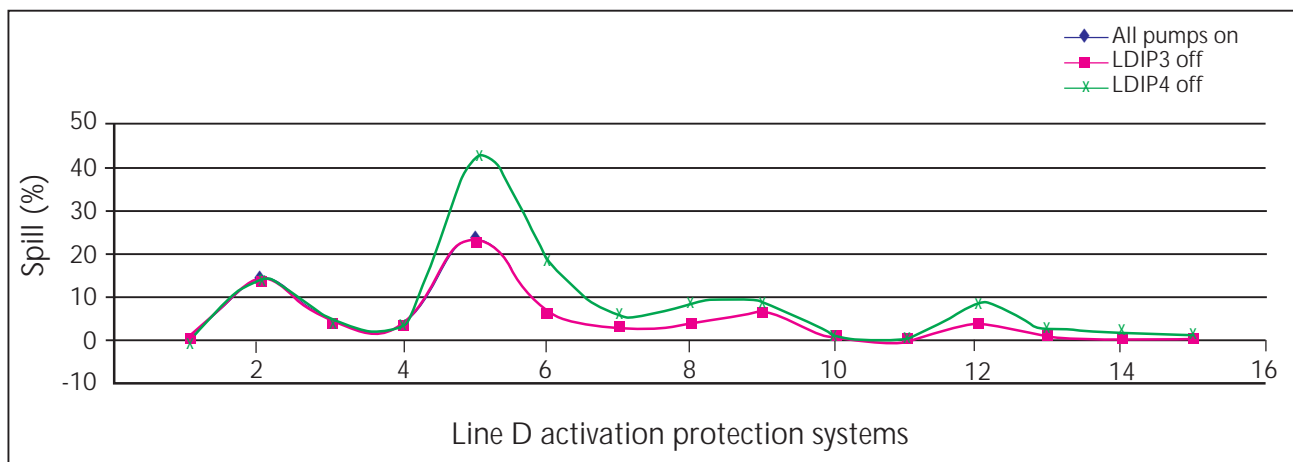

↑ **Fig. 2.** *Measured beam sizes for PSR (LBEG) and WNR (MPEG) beams in the linac (05WS2-12WS1).*
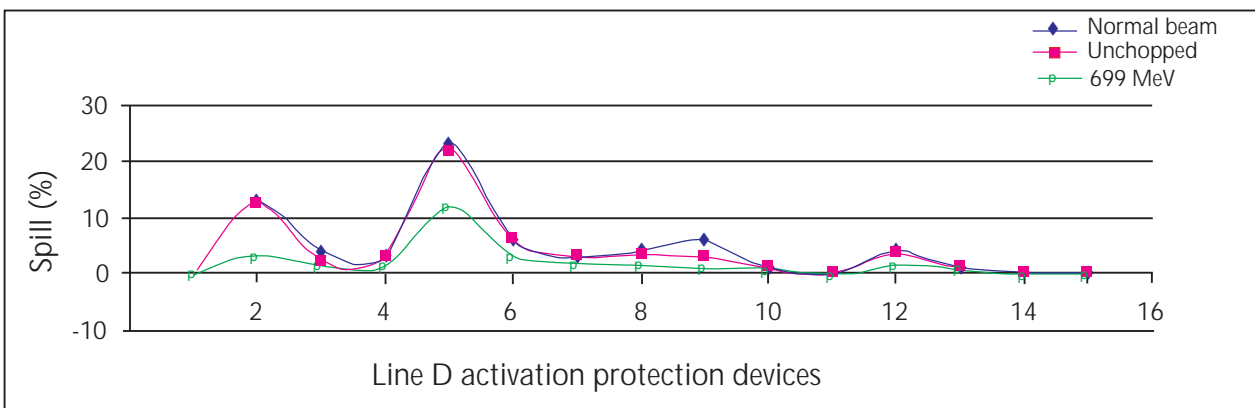
↑ **Fig. 3.** *Spill pattern for the PSR beam in the SY and LD (10-μA average current) for the three cases explained in the text.*

↑ Fig. 4. *Spill pattern for the PSR beam in the SY and LD (10-μA average current) showing effect of vacuum.*

Next we tried to change the vacuum in the LD by turning off separately the ion pumps, LDIP3 and LDIP4. No change in the spill or in the current readouts of the neighboring ion pumps was observed after LDIP3 was turned off for more than 30 minutes. However, spill levels in LD began to increase 5 minutes after LDIP4 was turned off (Fig. 4), which indicates a poor pumping efficiency of LDIP3. Improving the vacuum in SY and LD can improve the spill there substantially.

Chopping and bunching the beam produces emittance growth. To test this, we calculated the beam emittance at the end of the linac by measuring 41-48WS and using the WSMATCH program. The conclusion is that the emittance growth is ~ 20% for the chopped (normal) beam. The beam size in the machine is also consistently smaller for the unchopped beam, as expected. These measurements were taken with beam to RIBS (Ring Injection Beam Stop) at a 10-μA average current. The peak current in the machine was kept at the normal value of ~ 7 μA. TBFJ1s (transport B four jaw No. 1) were used to jaw down the peak (reduce the beam current) to 7 μA for the unchopped beam. The beam size in the SY was slightly smaller (5–10%) for the unchopped beam than for the chopped beam. But there was hardly any change in the spill levels (Fig. 3), although lower levels were expected from the beam-size measurements.

Krause Modulation Using the Beam Chopper

In the Krause modulation investigation, we examined the possibility of using the beam chopper instead of the ground-level deflector for modulating the beam pulse width at the beginning of the accelerator beam gates.

Currently each macropulse for the 1L Target has a time structure that allows the radio-frequency (rf) power control systems for the linac to respond reasonably to the sudden demand for power as the beam loads the systems at the beginning of the macropulse. This time structure consists of 15 pulses of increasing length during the first 30 μs of the macropulse, which appears as a ramping up of the beam current in the accelerator. Through a process known as Krause modulation, the beam is transversely deflected with a ground-level deflector to a beam stop during the time between the pulses. As the ground-level deflector is turned on and off, the beam is partially deflected. Some of this partially deflected beam is later spilled from the accelerator.

Independently of the Krause modulation, the beam chopper produces a time structure that is necessary for PSR operation. This time structure consists of a repeating pattern of about 280 ns "on" and 70 ns "off" throughout the beam macropulse. As in the ground-level deflector when the time that the chopper voltage is turning on and off, beam is only partially deflected and is directed off of the beam centerline and later spilled from the accelerator. Thus there are two devices causing partial deflection of the beam during the first 30 μs of the macropulse.

New capabilities in the chopper pattern generator allow for a new scheme to ramp up the beam current at the beginning of the macropulse. This scheme involves slowly increasing the beam pattern width from 30 ns to the full 280 ns and not modulating the ground-level deflector. Thus only one device is producing partially deflected beam. Moreover, the lifetime of the ground-level

deflector's driver electronics may improve as demand for its use is reduced. We implemented this scheme during an accelerator-development period in October 2001. We found that the rf control systems still responded reasonably well to this method of ramping up the beam current. The beam was sent to the PSR, and no deleterious effects were observed. We compared measurements of the beam profiles and beam spills in the two schemes but found no significant differences. This scheme could be implemented without negative effects on operations and may improve reliability.

Research Highlights

Upgrades of the LANSCE Quadrupole-Magnet-Power Supplies

S. Cohen, M. Fresquez, E.A. Morgan, L. Duncan (LANSCE Division)

Over 700 magnet-power supplies are required to drive the magnetic optics that precisely guide the proton beam through the Los Alamos Neutron Science Center (LANSCE) linear accelerator (linac) and experimental areas. The LANSCE-6 Magnet Power Supply (MPS) team has the responsibility for the reliable operation of these supplies. Replacing outdated and obsolete power supplies is a continuous job for the MPS team. The team's main concerns always revolve around safety, reliability, and compatibility with both the existing accelerator hardware and any anticipated future upgrades to the hardware and control software. Whenever possible, we try to use commercially available "off-the-shelf" units. In addition to the benefit of quick delivery times, commercial equipment has usually been certified for safety by a nationally recognized testing laboratory.

Design and Installation of Magnet-Power Supplies

During 2001, twelve quadrupole-power supplies were replaced and their controls upgraded. Seven supplies drive quadrupoles in the Low-Energy Beam Transport (LEBT) line and five larger units replaced antiquated water-cooled power supplies for the beam-line magnets of the Proton Storage Ring (PSR) injector. The new commercial off-the-shelf power supplies replace old custom-built units for which parts have become unavailable.

Although the power supplies are commercial items, they still need specifically designed electronics to be used with the LANSCE linac control system. Ease of safe repair and increased reliability were the primary concerns in the final design and installation of the control-system interface for the power supplies. All of the new supplies have isolated test points to protect technicians from potentially dangerous voltages and currents. If repairs are needed, the control electronics are on swing-out panels for easy access (Fig. 1.)

↑ Fig. 1. *This photo of the LEBT quadrupole-power supply shows swing-out electronics for safe, easy servicing.*

The new power-supply controls, designed and built by the MPS team, are compatible with the existing linac control system and have been built in "hooks" to allow it to work with anticipated control-system upgrades. The LEBT power supplies replace 30-year-old supplies, which were responsible for a significant fraction of the MPS system down time during the 2000 run cycle. During the 2001 run cycle, there was no down time attributed to these new power supplies and their controls.

Another power-supply upgrade using the same technology was implemented for five PSR-injector quadrupoles. Because these new power supplies include in-house modifications, their operation mimics the units that were replaced and eliminates operator confusion and adjustments for the new equipment (Fig. 2).
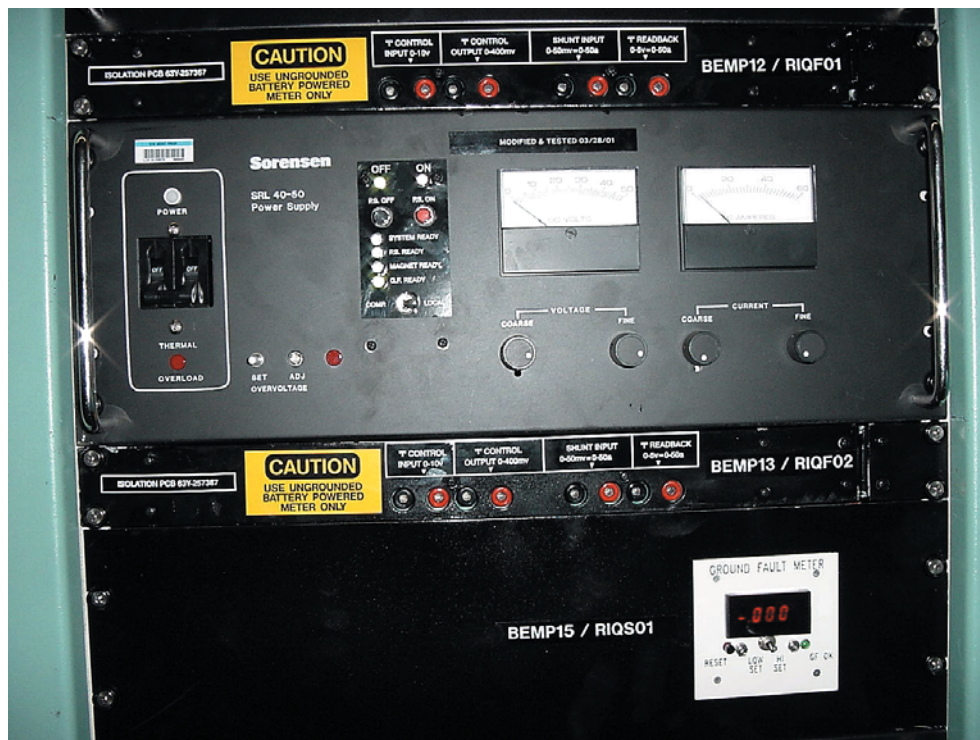
↑ *Fig. 2. This photo of the power-supply unit for PSR-injector quadrupole shows the electronic panel that mimics the operation of the unit that was replaced.*

Research Highlights

LANSCE Accelerator Control System Upgrade

E.A. Bjorklund, M.J. Burns, G.P. Carr, J.A. Faucett, D.J. Hayden, M.D. Lusk, M.A. Oothoudt, J.M. Potter, J.A. Reynolds, D.B. Romero, S.C. Schaller, F.E. Shelley, Jr. (LANSCE Division)

The Los Alamos Neutron Science Center (LANSCE) Accelerator Control System (LCS) uses hardware and software originally developed in the 1960s through the 1980s for the half of the facility that had not been upgraded to the Experimental Physics and Industrial Control System (EPICS). (EPICS contains a set of tools for building applications, a run-time environment, and a high-performance, flexible architecture—all of which provide a foundation for building a system that controls experimental physics applications.) Vendor support for LCS hardware and software is withering or gone and spare parts are becoming difficult to obtain. An effort is under way to upgrade the LCS software and hardware to modern, maintainable standards. Approximately half of the 25,000 command and read-back channels in the LCS have been upgraded to EPICS, but progress has been slow due to limited funding. The upgrade strategy is to replace first those things most likely to fail and cause accelerator down time. During 2001, progress was made on hardware and software upgrades, and an important proof-of-principle test was performed on an upgrade path to EPICS for the 1960s hardware interface to approximately 9,000 channels. (Fig. 1 is a photo of members of the LANSCE LCS team.)

Computer Hardware Upgrades

The LCS uses VAX (virtual address extension) computers in remote locations along the beam line to command and read devices in those locations. Operators use other VAXs in the control rooms to monitor and control the accelerator. By today's standards, the VAXs are very slow and extremely expensive. Maintenance is also expensive, and repair times are becoming longer.

Three of the nine remote VAXs were upgraded to EPICS Input/Output Controllers (IOCs) during 2001. The remaining six VAXs will be upgraded after software is converted to EPICS.

↑ **Fig. 1.** *Members of the LANSCE Accelerator Control System Team: Matthew Lusk, Stuart Schaller, Fred Shelley, Gary Carr, Michael Oothoudt, Jerry Potter (back row, left to right); John Faucett, Dolores Romero, Mary Burns (front row, left to right); Eric Bjorklund, David Hayden, Jerome Reynolds (not present).*

The VAX responsible for the Injector Control Room (ICR) console was replaced with a Sun workstation running EPICS software. The control-room knob-interface panels used by operators for incremental control of devices were converted from VAX CAMAC (computer-automated measurement and control) hardware to IOC VME (virtual memory extension) hardware. All CAMAC hardware was removed from our main VAXs in this conversion. Most of the disk files managed by the VAXs were moved to a Sun disk server. The remaining files will be moved to this server after software upgrades scheduled for the 2002 run cycle outage are made. Two of the six remaining control-room VAXs will then be removed.

In addition to VAXs, the control-room consoles require Sun computers to run EPICS software. The Sun computers in the Central Control Room were replaced with new low-cost computers that are three times faster. The improved speed of the newer Suns provides operators with faster notification of changes and smoother control of devices. The older Suns were redeployed to less heavily used parts of the facility such as the ICR.

Computer Software Upgrades

The software in the LCS is heavily dependent on the VAX/VMS (virtual memory system) operating system. The control-system programs must be rewritten to move their functionality to EPICS. Of the approximately 250 programs in the LCS, 73 have been identified as necessary in the new EPICS system. Some of these programs are fairly simple and required only a few man months to write the original code, but others are very complicated and required several man years for the original code. Fortunately, with modern software tools (such as EPICS Display Manager and Java), the programs can be rewritten with much less effort and cost. During 2001, software programs for accelerator parameter management (PM, PSRPM), data display (BEAMPLOT, DSRP, INJWATCHER, PULSEPLOT, S-HTEST, XYPLOT), radio-frequency power control (RFON), and accelerator tune-up (UNROLL) were converted to EPICS.

The VAXs also supply services that need to be moved to the new LCS system. The VAXNotes system contained historical data on maintenance and operation of the accelerator that many teams use as references for their work. This information was moved to a Web server, and a search capability was added.

Moving the control-room knob-interface panel from VAX CAMAC hardware to EPICS VME required a major

software effort. The software was completed, tested, and put into production in 2001.

Remote Instrumentation and Control Equipment System Replacement Test

The Remote Instrumentation and Control Equipment (RICE) system is the hardware interface to approximately 9,000 input and 2,100 command channels for the linear accelerator and experimental-area beam lines. The system was designed and built in-house in the late 1960s. As the system aged, the majority of its hardware components became unavailable. Replacement of this old custom-made system with a new single system is very difficult; hence only minor improvements have been made over the years. However, about 80% of the channels (those not needing detailed information on the beam-time structure) can now be implemented in commercial programmable logic controller (PLC) systems. Furthermore, software needed to interface EPICS to PLCs has been developed by LANSCE-8 in support of the Spallation Neutron Source project. Thus, testing the operation of part of the accelerator with a PLC system was deemed useful.

In December 2001, most binary control and read-back channels for the last accelerating module of the accelerator were moved from RICE to a PLC. Software was written to interface the PLC data to the LCS so that existing programs could use the data from the PLC. The accelerator was operated for three weeks in this configuration with no problems. A proposal is being written to permanently replace this class of RICE channels with a PLC system. A proposal for dealing with the channels that depend on beam-time structure (mostly diagnostics) will be developed later. For further information on these upgrade activities, see *LANSCE Control System Upgrade Progress and Plan*, October 1, 2001, LA-UR-01-6403, http://lansceops1.lanl.gov:8000/controls/Upgrades/20001231PlanProgress.pdf, and *Results of RICE Replacement Test*, December 17, 2001, LA-UR-02-0071, http://lansceops1.lanl.gov:8000/controls/Upgrades/RICE_Repl_test_result.pdf.

Research Highlights

Measurements of Proton Beam Halo in the Low-Energy Demonstration Accelerator

R.W. Garnett, D. Gilpatrick, W. Lysenko, T.P. Wangler, M.E. Schulze, R. Sheffield (LANSCE Division), K.C.D. Chan, P. Colestock, J.D. Schneider (NIS Division), H.V. Smith (DX Division), C.K. Allen (SNS Division), K.R. Crandall (TechSource), J. Qiang (Lawrence Berkeley National Laboratory)

The formation of beam halo is an important concern for high-intensity proton linear accelerators because halo particles lost in the accelerator can induce radioactivity, which complicates the maintenance of the accelerator and reduces overall availability. Therefore, it is important to understand the physical causes and possible cures for beam halo and beam losses. These concerns provided the motivation for a first experimental study of proton beam halo, which was carried out at the Low-Energy Demonstration Accelerator (LEDA).[1,2,3] The measurements were completed in 2001, and analysis of the data is in progress.

Understanding Beam-Halo Formation

The LEDA Facility delivered a 6.7-MeV, 100-mA proton beam from the 350-MHz radio-frequency quadrupole (RFQ) into a new beam line that was designed and built for the experiment. The beam line consisted of a periodic array of 52 quadrupole magnetic lenses for transverse confinement of the beam and beam-diagnostic devices to monitor and measure the beam properties, particularly the horizontal and vertical beam-density profiles. Nine interceptive beam-profile diagnostics were the primary instruments used to measure the beam distributions. These newly designed diagnostics determine the beam's horizontally and vertically projected particle-density distributions with an approximate 10^5:1 dynamic range. These diagnostics used both traditional wire-scanner and water-cooled, graphite-scraping devices. Combining data from these two devices using computer software results in a single ultra-high dynamic-range device, called a wire scanner, halo scraper (WS/HS).

To study beam-halo formation in the new beam line, the first four quadrupoles were energized to establish mismatch conditions more or less favorable for beam-halo formation. The mismatches were chosen to correspond to either of two modes of the beam: (1) a symmetric or breathing mode, where the oscillations in the two transverse planes (x and y) were in phase, and (2) an anti-symmetric or quadrupole mode, where the oscillations were out of phase. We will use the

measured beam distributions for these two cases to test our beam-dynamics simulation codes, to answer practical questions concerning whether the aperture radii in future high-current accelerator designs are properly chosen, and to determine whether special collimation systems are required at low energies to scrape the halo and limit the beam losses at high energies. As a test of our understanding of the physics of the beam, we are also interested in its transverse root-mean-square (rms) emittance. The rms emittance measures the area occupied by the beam in phase space, which is defined by the coordinates and angles of the particles relative to the beam center. The rms emittance can be determined experimentally from measured rms beam sizes at different locations.

From theory, we believe that the main cause of beam-halo formation in a periodic focusing channel is beam mismatch. A beam is matched when there is a balance between the inwardly directed focusing force and the outwardly directed forces composed of the space-charge force plus a pressure force from the rms emittance. Beam mismatch corresponds to an imbalance in the forces, which acts in two ways. First, a mismatch induces oscillations of all the beam particles and an immediate increase in the amplitudes of particle transverse excursions. Second, the repulsive space-charge force, which acts while the particles oscillate through the beam, slowly drives some particles to even larger amplitudes. We believe the simulation codes contain the correct physics to describe these effects. However, there may be additional effects not yet included in the simulation codes that also influence the particle distributions. In addition, an important uncertainty in the experiment is the lack of detailed knowledge of the input beam from the RFQ. Nevertheless, the beam-halo experiment tests the hypothesis that the formation of beam halo is induced by mismatched beams.

Description of the Beam-Halo Experiment

The RFQ was capable of delivering a continuous or pulsed beam comprised of a sequence of sub-nanosecond bunches at a 350-MHz rate. To avoid melting the thin wires used to measure the beam profiles, the beam was pulsed at 1 Hz in 30-μs macropulses. The beam line (Fig. 1), beginning at the end of the RFQ,
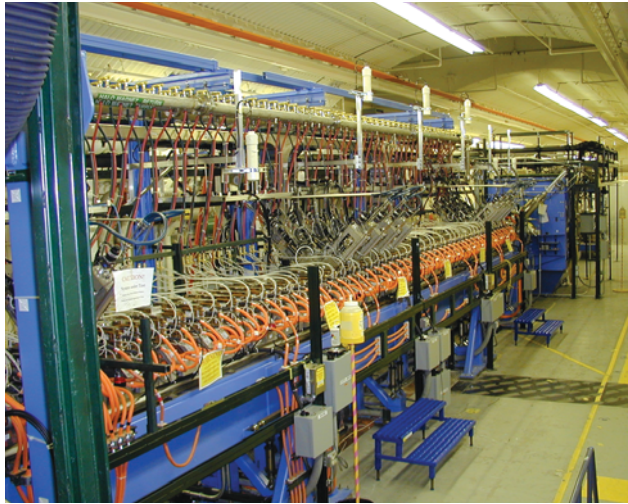
consisted of a 52-quadrupole focusing lattice with 9 beam-profile diagnostics, 10 beam-position monitors (BPMs), 10 beam-steering magnets, 5 beam-loss monitors, and 3 beam toroids for beam-current measurements. The focusing lattice was a spatially periodic array of alternating focusing and defocusing quadrupole magnets with a 21-cm cell length for each of the 52 cells. This resulted in 26 focusing periods and a total length of approximately 10.9 m. The beam propagated in vacuum within a 27.8-mm inner-diameter (ID) beam pipe. There were no longitudinal focusing elements to keep the short bunches from expanding along the beam axis, and after a few meters the bunches overlapped to form a continuous modulated beam. The main effect of the longitudinal debunching on the transverse particle dynamics was to reduce the effective beam current and accompanying space-charge forces that affect the transverse beam-halo formation. However, the effects of the transverse space-charge forces in the mismatched beam were still predicted to be easily measurable.

The beam-profile diagnostics were nominally located in the middle of the drift spaces between chosen quadrupole pairs. Eight of the diagnostics were distributed in two clusters of four each. The choices of four diagnostics per cluster, the spacing of the diagnostics, and the locations of the clusters allowed us to calculate the rms emittance from the beam-profile measurements at two locations, one shortly after the beam had debunched and the other near the end of the beam line. The first diagnostic was installed near the beginning of the beam line

to monitor the input particle distribution, determine whether there was halo present in the input beam, and determine the rms emittance of the input beam.

Beam Diagnostic Instrumentation

With their unique design, the beam-profile diagnostics (Fig. 2), each consisting of two WS/HS assemblies for measurements in each transverse plane, were the most important diagnostic devices for the experiment. These instruments acquired horizontal and vertical particle-density distributions over an approximate 10^5:1 dynamic range. We measured the core of the distributions using traditional wire scanners and measured the tails of the distribution using a pair of water-cooled graphite scraping devices (one scraper on each side of the wire). The wire scanners and the halo scrapers were mounted on the same moving frame whose location was controlled with stepper motors. A sequence within the Experimental Physics and Industrial Control System (EPICS) software communicated with a LabVIEW virtual instrument from National Instruments to control the motion and location of each WS/HS assembly. Both secondary electrons from the wire scanner's 0.033-mm carbon wire and protons impinging on the scrapers were detected with a loss-integrator electronic circuit. Algorithms implemented within EPICS and Research Systems' Interactive Data Language subroutines analyzed and plotted the acquired distributions. Beam loss was measured by detecting the ionizing radiation resulting from beam interception by the beam pipe or other structures. A CsI scintillator attached to a 5-cm photomultiplier (PM)[4] allowed the detection of beam-induced radiation over a dynamic range of 10^8:1. The signal from a high-gain PM tube was fed to a trans-impedance amplifier via a coaxial cable. The 170-kHz bandwidth of the front-end electronics allowed for observation of 1-ms beam-loss variations. These beam-loss monitors were sufficiently sensitive to detect less than 70 pA of beam loss.
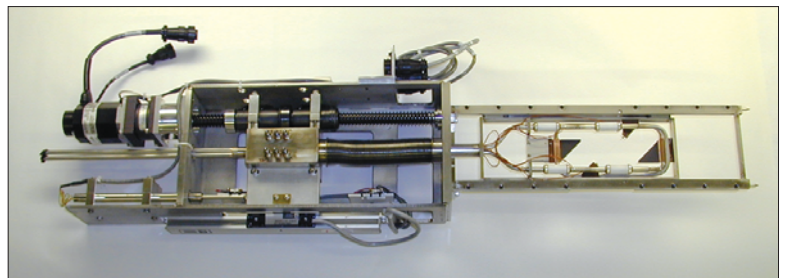
↑ **Fig. 2.** *One of two WS/HS actuator assemblies per station used to measure the vertical and horizontal beam profiles. Each scanner assembly contained a wire and a pair of plates, located at the right of the picture. These profile measurements have a 10^5:1 dynamic range.*

It was important that the beam be centered within the 27.8-mm ID beam-pipe aperture to within 1 mm. The beam-position measurement consisted of a traditional micro-stripline type of BPM, a cable plant, a 200-kHz log-ratio electronics processor, and an interface from LabVIEW to EPICS that provided the linearization and calibration algorithms. Over a 74-dB dynamic range in beam current, the position measurements had an accuracy and resolution of < 1% and < 0.02% of the beam pipe ID, respectively. A bunched-beam current was obtained as the sum of the four electrode signals from a BPM. The pulsed beam current was measured with a set of three alternating-current transformers manufactured for LEDA by Bergoz. These transformers performed with a resolution and accuracy of < 0.1 and 0.5 mA, respectively.

Initial Results

Measurements have been made at proton-beam currents of 16, 50, 75, and 100 mA and at different values of a mismatch parameter μ, defined at the match point as the ratio of the initial to the matched beam size. Typical measured transverse profiles are presented in Fig. 3, where the matched (top) and breathing-mode mismatch at $\mu = 1.5$ (bottom) profiles are shown near the end of the beam channel for a 75-mA beam current. The approximately parabolic shape in the semi-logarithmic plot of the matched profile is qualitatively consistent with expectations for a Gaussian-like beam core. The plot shows evidence of a particle-density signal above noise out to 10 mm from the peak, which is more than 8 times the 1.2-mm rms width of the matched beam. The large observed amplitudes even for a matched beam are consistent with the hypothesis that large-amplitude halo particles are already present in the input beam.

For the mismatched profile, we observe unexpected structure in the form of shoulders in the semi-log plot. These shoulders correspond to density levels of about 10% of the peak. The rms size of the mismatched profile is 1.8 mm, and there is evidence for a particle-density signal above noise out to about 10 mm from the peak, which in this case is not different than the maximum amplitude for the matched beam. The shoulders, which are the most prominent general feature for the mismatched beams, may be a consequence of non-elliptical phase-space contours below the 10% density level.

The rms emittances at 75 mA, shown in Fig. 4, increase with distance along the channel and increase with increasing mismatch strength as expected if mismatch is responsible for growth of beam halo. The observation of rms-emittance growth for mismatched beams,
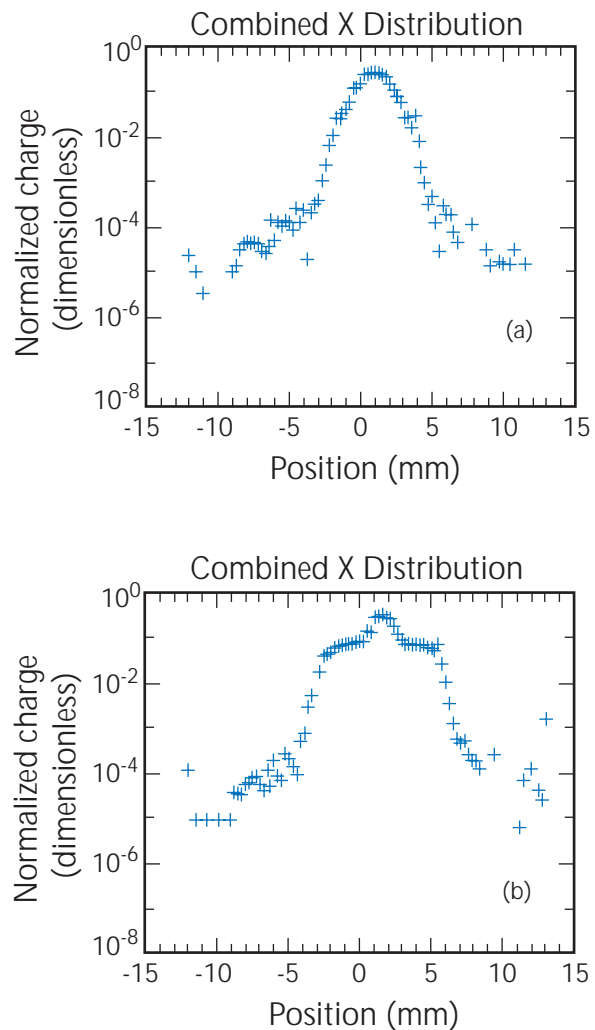
Fig. 3. *Measured beam profiles in x near the end of the beam line. The plot at the top (a) is for the matched beam, and the plot at the bottom (b) is for a mismatched beam. The position in the abscissa is obtained by combining data from WS/HS devices.*

together with only small increases in maximum detectable amplitudes, suggests that the particles driven outwards by the beam oscillations have not yet attained large enough amplitudes to contribute much to the outermost regions of the particle distribution, which are already populated.

Multiparticle simulations in the transport channel have been carried out using the IMPACT code[5] with a three-dimensional particle-in-cell, space-charge subroutine. The simulations use ten million particles and an input beam distribution based on previous multiparticle simulations beginning at the ion source. The measured beam profiles are about 30% broader than those from the initial simulations.
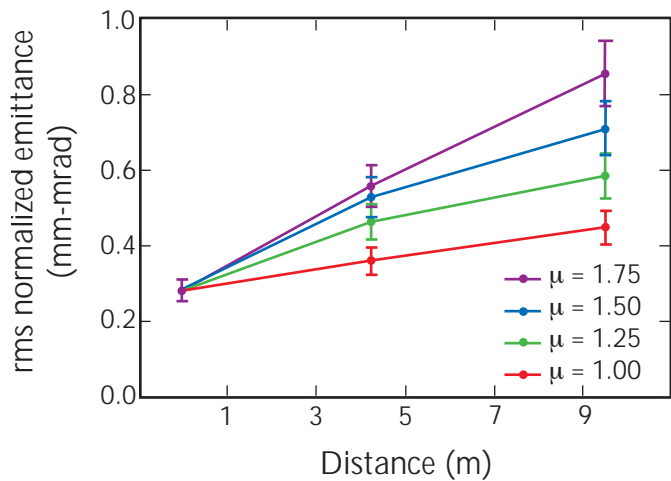
↑ Fig. 4. *Normalized rms emittance in x at 75 mA versus distance at different breathing-mode mismatch strengths measured by the mismatch parameter μ described in the text.*

Conclusion

The beam-halo experiment at LEDA addresses questions on the frontiers of accelerator physics and has provided the first experimental tests of our understanding of halo formation in high-current proton beams. The beam-profile diagnostic has opened a new regime for observing beam halo to densities as low as 10^{-5} of the core density. The emittance-growth results are confirming our general expectations for halo growth caused by beam mismatch. The experiment is also providing new and unexpected results. We observe evidence for halo in the input beam. The mismatched-beam profiles show unexpected structure, which suggests nonlinear aberrations of uncertain origin. The measured beam sizes are about 30% larger than predicted from the simulations. Work is now in progress towards a better understanding of these measurements.
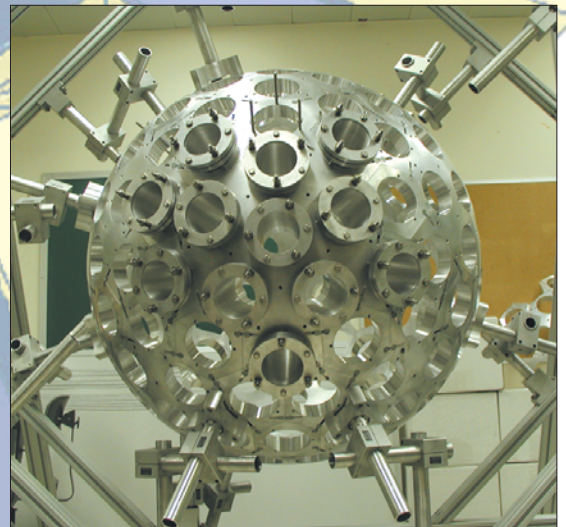
References

1. P.L. Colestock *et al.*, "Measurements of Halo Generation for a Proton Beam in a FODO Channel," in *Proceedings of the 2001 Particle Accelerator Conference* (IEEE, 2001), 170-172.

2. M.E. Schulze *et al.*, "Characterization of the Proton Beam from the 6.7-MeV LEDA RFQ," in *Proceedings of the 2001 Particle Accelerator Conference* (IEEE, 2001), 591-593.

3. T.P. Wangler *et al.*, "Experimental Study of Proton-Beam Halo Induced by Beam Mismatch in LEDA," in *Proceedings of the 2001 Particle Accelerator Conference* (IEEE, 2001), 2923-2925.

4. J.D. Gilpatrick *et al.*, "Experience with the Low Energy Demonstration Accelerator (LEDA) Halo Experiment Beam Instrumentation," in *Proceedings of the 2001 Particle Accelerator Conference* (IEEE, 2001), 2311-2313.

5. J. Qiang *et al.*, "An Object-Oriented Parallel Particle-in-Cell Code for Beam Dynamics Simulation in Linear Accelerators," *Journal of Computational Physics* **163**, 434 (2000).

Research Highlights

Mercury Target Development Tests for the Spallation Neutron Source at the Weapons Neutron Research Facility

J.R. Haines, B.W. Riemer, C.C. Tsai, D.C. Lousteau, J.D. Hunn, K. Farrell, L.K. Mansur
(Oak Ridge National Laboratory), **S.A. Wender, B.E. Takala, V. Tcharnotskaia**
(LANSCE Division)

For several years, Oak Ridge National Laboratory (ORNL) researchers have been collaborating with researchers from the Weapons Neutron Research Facility (WNR) at the Los Alamos Neutron Science Center (LANSCE) to study issues associated with using mercury as the target material for the Spallation Neutron Source (SNS). Mercury was selected as the target material for the SNS because of its favorable neutron-production characteristics and potential to handle the high-proton-beam power (2 MW) that is planned for this facility. An important issue identified for liquid-metal targets in pulsed sources is their ability to withstand the rapid pressure increase when they are irradiated by the pulsed proton beam. Although a WNR pulse contains much less energy than a pulse for the 2-MW SNS, focusing the WNR proton beam in the Blue Room down to a size of about 20 mm in diameter will allow us to reasonably simulate the beam intensity, and therefore the pressure increase, expected for the SNS. Previous tests with an array of target shapes, diagnostics, and instrumentation measured the vessel strain to ensure that the target can sustain the dynamic pressure loads. Besides providing data that are helping the SNS team to design and analyze the actual SNS target, these tests successfully demonstrated that a newly developed fiber-optic-based strain-measurement system could function in this demanding radiological environment.

Understanding Pitting in Irradiated Targets

Tests conducted during 2001 were designed to examine whether the pressure pulse caused pitting damage to the stainless-steel container for the mercury. The pitting phenomenon was first identified as a potential concern by a team of researchers at the Japan Atomic Energy Research Institute, where they observed pitting of stainless-steel surfaces that were in contact with mercury subjected to large, mechanically induced pressure pulses. As such, we then need to discern whether the surfaces of mercury-target vessels become pitted with comparable beam-induced pressure pulses. This issue could not be resolved from examinations of targets previously irradiated at WNR because these targets were not inspected before irradiation and the roughness of the surfaces was too great to distinguish between beam-induced pits and other imperfections in the surface of the materials.

Because of the urgency to complete the SNS target design, we conducted two experiments in 2001 to study the pitting issue—in July and December. One of the two targets used in July 2001 is shown in Fig. 1. This type of cylindrically shaped target is referred to as a "large-effect" (LE) target and was first used in the strain measurements to obtain an easily measured "large" strain in the thin diaphragms that were incorporated in the end plates/flanges.


800-MeV PSR proton beam

↑ **Fig. 1.** *LE target used for the July 2001 mercury-target-pitting tests in the Blue Room at WNR. Thin diaphragms were used in these tests to achieve large strains.*

All four of the diaphragms tested in July 2001 were fabricated from 316-type stainless steel in the annealed condition. Three of four were used directly in the LE targets, whereas the fourth was treated with a surface-hardening technique. This treated diaphragm was used on the rear (proton-beam exit) end of one of the two LE targets.

A photograph of the mercury-facing surface of one of the untreated diaphragms is shown in Fig. 2. As shown in the photo, large pits, visible to the naked eye, are distributed over a region that is about 5 mm in diameter and centered about 10 mm directly below the center of the diaphragm. Using activation-analysis techniques, the beam was centered approximately 5 mm directly above the center of the diaphragm. This 180° shift between the beam and the pit region may be due to radial focusing of the pressure wave and its reflection off of the side walls of the cylinder.

Micrographs of the surface of one of the untreated diaphragms before and after exposure to 200 nearly full-current pulses from the Proton Storage Ring (PSR) are
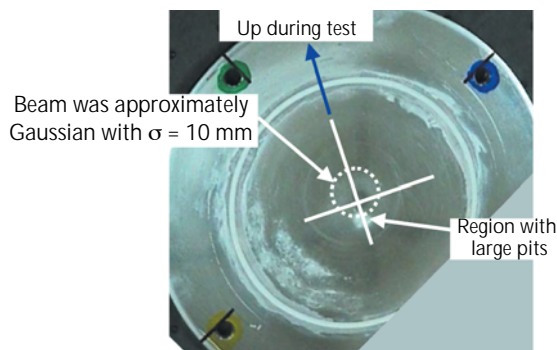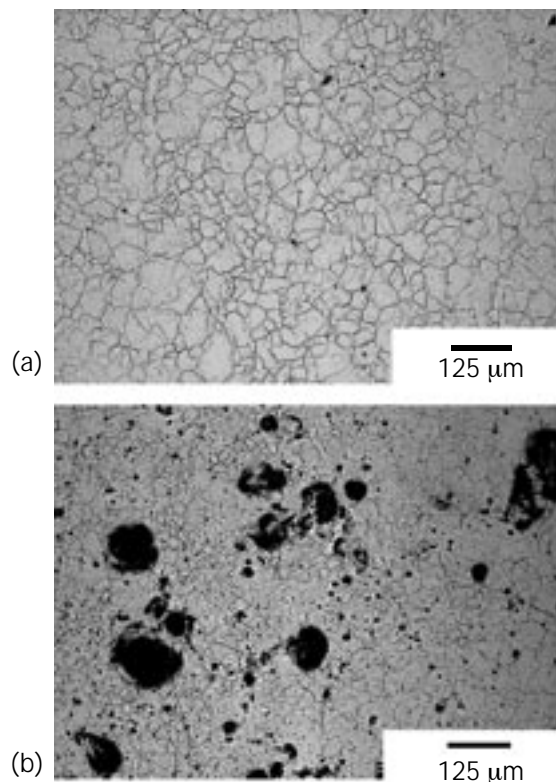
↑ **Fig. 2.** *This thin diaphragm flange was exposed to mercury in the July 2001 tests in the Blue Room at WNR. The cross marks the center of the diaphragm and the circle indicates the 1-σ boundary of the approximately Gaussian-shaped beam. Large pits were clustered in a region symmetric to the center of the beam relative to the center of the diaphragm. This shift may be caused by the radial focusing of the pressure wave.*

↑ **Fig. 3.** *This image shows micrographs of a stainless-steel diaphragm from one LE target used in the July 2001 mercury-target-pitting tests: (a) a typical region before beam exposure, and (b) a section near the center of the diaphragm containing large pits that were formed by exposure to 200 pulses in the Blue Room at WNR. These large pits had diameters of up to approximately 100 μm. Small, randomly distributed pits were also found on the bare surface of the three annealed stainless-steel specimens. Large pits were found, to a lesser extent, on the one diaphragm that was treated with a hardening process, and dramatically fewer small, randomly distributed pits were detected.*

shown in Fig. 3. Evidence for pitting is obvious in these images. In carefully examining the diaphragm surfaces, two categories or types of pits were observed: (1) large (~ 100-μm-diam) pits that appeared in a cluster near the center of the diaphragm, as shown in Fig. 2, and (2) randomly distributed, small (~ 10-μm-diam) pits. Large and small pits occurred on both the front (beam entrance) and rear (beam exit) of the untreated diaphragms. Although some of the large pits clustered near the center of the diaphragm were found on the surface-hardened diaphragm, dramatically fewer randomly distributed pits could be detected at the resolution used to perform the inspections (~ 5 μm).

Based on the July 2001 test results, we concluded that mitigating this pitting damage is required to ensure that the mercury target can achieve an acceptable lifetime at the SNS. With this in mind, the December 2001 tests were dedicated to further examine the pitting phenomenon and looking at possible elimination, or at least reduction, of the pitting problem.

Seven mercury targets were tested in December 2001. Four of these targets used different shapes or different diaphragm materials and were exposed to 200 beam pulses. Most notably, we used a target with a rectangular cross section in an attempt to eliminate the postulated radial focusing of the pressure wave. Also, we tested diaphragms with increased thickness in an attempt to reduce the large stresses. Two targets were also tested with only 20 pulses to determine whether future experiments might be possible at this reduced fluence level. Finally, a lead-bismuth target, with geometry and materials essentially the same as that used in July 2001,

was exposed to the WNR beam for 200 pulses. This experiment was done in collaboration with the LANSCE team working on the lead-bismuth target design for the Advanced Accelerator Applications program. Examination of the December 2001 irradiated targets will begin in late February 2002 following their shipment from Los Alamos National Laboratory to ORNL after extensive decontamination and health-physics inspections.

Conclusion

Further Blue Room tests to examine alternative mitigation schemes and the threshold for pitting damage are proposed for July 2002. Specific plans must await results of the inspection of the targets irradiated in December 2001. Our next tests will likely be the final tests before committing to construction of the SNS target.

Research Highlights

New Measurements of Neutron-Induced Fission of Uranium with GEANIE

R.O. Nelson, N. Fotiades, M. Devlin, G.D. Johns (LANSCE Division), T. Ethvignot, P. Casoli, T. Granier (Commissariat à l'Energie Atomique, France), W. Younes, J.A. Becker, L.A. Bernstein, P.E. Garrett (Lawrence Livermore National Laboratory), C.A. McGrath (Idaho National Engineering and Environmental Laboratory)

Over sixty years after the discovery of nuclear fission by Hahn and Strassmann,[1] its first interpretation by Meitner and Frisch,[2] and a more detailed description by Bohr and Wheeler,[3] numerous mysteries about this complex phenomenon still need to be solved. When a heavy nucleus bombarded by neutrons splits into two fragments, the properties of these fragments depend strongly on the intimate quantum structure and the excitation energy of the fissioning nucleus. It is difficult to precisely predict what these properties are theoretically, although modern computing capabilities are enabling insights never possible before. A recent description of some of these theoretical developments is given in Reference 4. An example of a recent calculation of the nuclear potential-energy surface[5] of the fissioning nucleus is given in Fig. 1 and will be described in more detail in this research highlight. Previous measurements were done with fairly low-energy neutrons, i.e., available at nuclear reactors and at mono-energetic sources below 15 MeV.[6,7] At the

Weapons Neutron Research Facility (WNR) at the Los Alamos Neutron Science Center (LANSCE), a relatively large flux of fast neutrons is available up to 400 MeV to extend these studies at much higher energy. As such, we hope to shed new light on this historic field of research with new measurements using the Germanium Array for Neutron-Induced Excitations (GEANIE) gamma (γ) ray spectrometer. The results are important not only for Defense Programs but also for improving our understanding of nuclear fission, which could be useful for future industrial applications involving fast neutron-induced fission (e.g., Advanced Accelerator Applications, which includes transmutation of nuclear waste and power generation).

Recent Experimental and Theoretical Progress

The two most abundant uranium isotopes have a different behavior with respect to neutron-induced fission. Uranium-235, or ^{235}U, is fissile, which means that fission is possible with neutrons of any energy, and the other one—uranium-238, or ^{238}U—will experience fission only with neutrons above a threshold energy of about 1.5 MeV. In recent experiments, pure targets of separated isotopes of ^{235}U and ^{238}U were irradiated with neutrons spanning a broad energy range at WNR.

The WNR at LANSCE uses a pulsed 800-MeV proton beam to produce neutrons with a broad energy spectrum. The neutrons are collimated along flight paths (FPs) to the sample under study. By measuring the time between the arrival of the very short proton-beam pulse at the neutron-production target and the arrival of the subsequent incident neutrons at the sample, we can determine the energy of the incident neutrons. This is the "time-of-flight" technique. The longer the FP, the better the incident-neutron energy resolution, but the lower the neutron beam intensity. GEANIE is located 20 m from the neutron-production target with typical neutron-energy resolutions of ~ 2% at 1 MeV, ~ 20% at 100 MeV, etc.
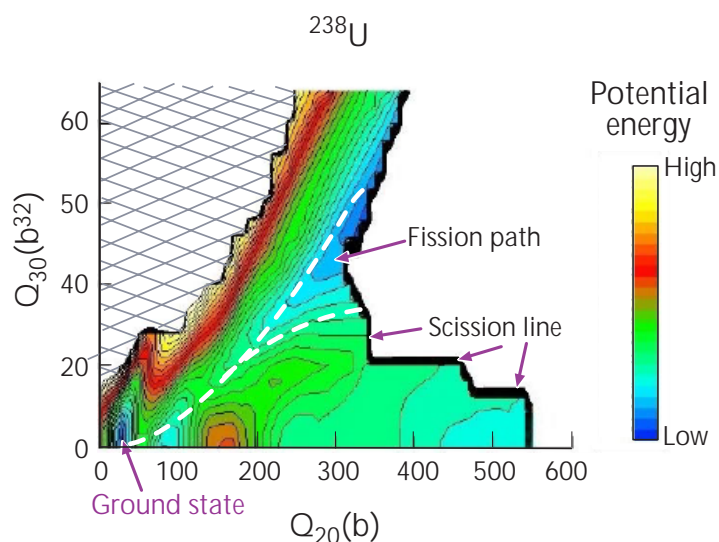

↑ **Fig. 1.** *Calculated potential-energy surface for the ^{238}U nucleus as a function of mass asymmetry (Q_{30}) versus elongation (Q_{20}).[5] The energy—or fission barrier—is minimized along the path from stability (ground state) to fission (the scission line) with asymmetric fragments. The crosshatched area shows the limits of the calculations.*

GEANIE consists of 26 high-resolution germanium (Ge) γ-ray detectors with 20 BGO (bismuth germinate) background-suppression shields. Eleven of the Ge detectors are made of thin Ge crystals. These thin crystals have excellent γ-ray energy resolution, but very low detection efficiency at γ-ray energies above 1 MeV. The other 15 Ge detectors have a relatively large volume with much higher efficiencies at higher γ-ray energies than the thin Ge detectors. The two types of detectors are complementary to each other and allow detailed studies of lower-energy γ-rays, such as those most often encountered in measurements from actinide nuclei, along with the higher-energy γ-rays that are also observed. The excellent energy resolution of the GEANIE detectors enables identification of fission fragments based on the known characteristic γ-rays that they emit.

Inclusive γ-ray measurements were performed in 1998 and 1999 with γ-rays recorded either individually (singles, γ) or in coincidence with each other (doubles, γ-γ). The complex spectra obtained consisted of hundreds of γ-rays from fission fragments, various uranium isotopes produced in (n,xn) reactions (including strong inelastic scattering), and background produced by scattered- and fission-neutrons interacting with the Ge detectors. More recently, a configuration optimized for γ-γ coincidence was used for acquiring data with targets of ^{235}U (in 2000) and ^{238}U (in 2001) targets. The γ-γ coincidence data allow us (through gating on individual, or groups of, transitions from a particular product nuclide) to separate the unresolved contributions to a γ-ray line from two or more fission fragments and from the various backgrounds. A third type of experiment was performed using thin ^{238}U deposits on thin silicon photovoltaic cells (Fig. 2). The photovoltaic cells are operated with special preamplifiers as fission-fragment detectors, enabling fission-fragment γ-ray coincidence measurements. These measurements provide "clean" fission-fragment γ-ray spectra. The thin targets necessary to detect the fission fragments also allow useful measurements of the x-rays emitted by these fragments (Fig. 3) and thus give an alternate method to discriminate on the nuclear charge (Z) of the fragments.

New theoretical work is being done to use the ever-increasing power of computers to predict the fission-fragment mass distributions that can be obtained from our data. The ^{238}U potential-energy surface shown in Fig. 1 results from a microscopic calculation (using the Hartree-Fock-Bogoliubov theory). By projecting the mass asymmetry onto the scission line where the fissioning nucleus breaks into two fragments, we can

Photovoltaic cells with targets

Ge detectors

Background suppression shields
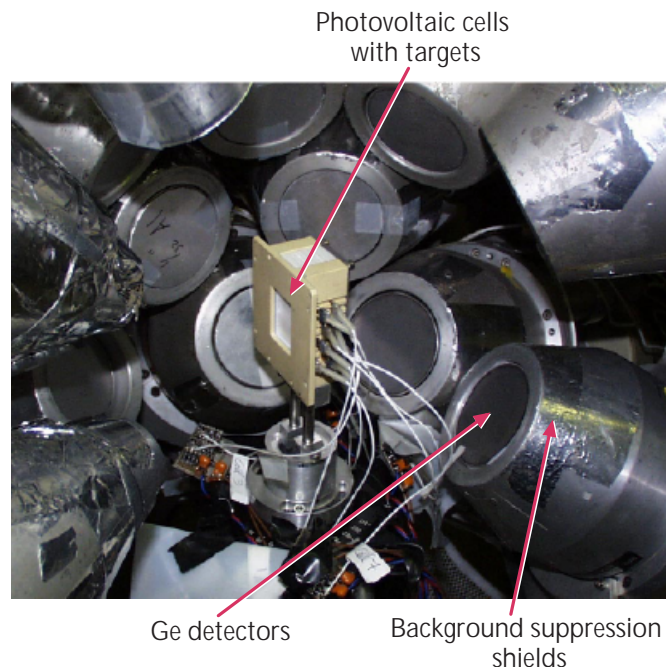
Fig. 2. *The ^{238}U target placed in the center of GEANIE consists of eight layers of uranium coated onto photovoltaic cells. With this device, only the fission events are selected amongst numerous reactions induced by the high-energy neutron beam incident on the setup.*
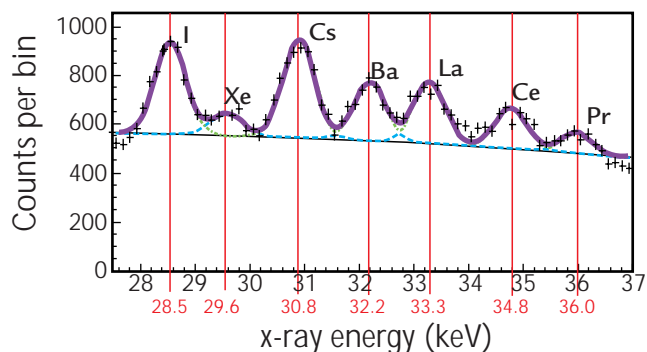
Fig. 3. *Observed x-ray peaks in the global GEANIE spectrum. The blue curve is a fit to the data. Each x-ray peak is labeled with the chemical symbol of the fission-fragment element.*

calculate the mass distributions of these two fragments. The goal of this work is to extend such calculations to higher energies and hence to predict the mass distributions measured in this work, or for any other nuclear system.

**Latest Results on Mass Distribution Versus Neutron Energy**

In a study of symmetric versus asymmetric fission of ^{235}U using γ and limited γ-γ data obtained on GEANIE,

Younes *et al.*[8] observed that the transition from predominantly asymmetric to predominantly symmetric fission-fragment mass splits occurs over a span of about 20 MeV of excitation energy from 14 to 35 MeV. Above about 85 MeV, the excitation energy of the fissioning system is not well defined but is distributed over a wide energy range. This detailed study of the energy dependence of this transition will allow for the testing of microscopic fission models at higher energies.

For ^{238}U neutron-induced fission, we have identified γ-rays from 101 different fission fragments from γ-γ coincidence data. Of these 101 nuclides, 9 are stable and would not be observed in typical radiochemical fission-product measurements. In terms of the neutron and proton makeup of the fission fragments, 72 are even(N)-even(Z) nuclides, 25 are odd-A nuclides, and 4 are odd(N)-odd(Z) nuclides (i.e., N is the neutron number, Z is the proton number, and A = N + Z is the mass number). The even(N)-even(Z) nuclides generally provide the most straightforward cases to study by γ-ray emission because most of the decay proceeds through the lowest-lying levels of the ground-state rotational band and because these low-lying levels are typically at excitation energies for which γ-ray emission is readily observable. Thus a large fraction of fragment yield is measured through the observation of a single γ-ray. The odd-A and odd(N)-odd(Z) nuclides are more challenging to study because the spectrum of their excited states is more complicated. Therefore, more γ-rays must be measured and the level scheme needs to be better known to reliably estimate the yield of a particular fission fragment.

Examples of the γ-ray production of four even(N)-even(Z) isotopes of xenon (A = 136-142) are shown in Fig. 4 as deduced from singles γ-ray data. The faster-than-expected decrease of the ^{140}Xe production with increasing energy may be due to nuclear structure effects that cause us to lose some of the gamma decay in our measurement. This loss can be due either to a delay of the decay (by a long-lived state) or to nuclear structure effects in which a significant fraction of the decay proceeds to the ground state by a different path than through the ground state rotational band. The fission-fragment yields for 4 isotopes of barium as inferred from the doubles γ-ray yields are shown in Fig. 5. Here the expected
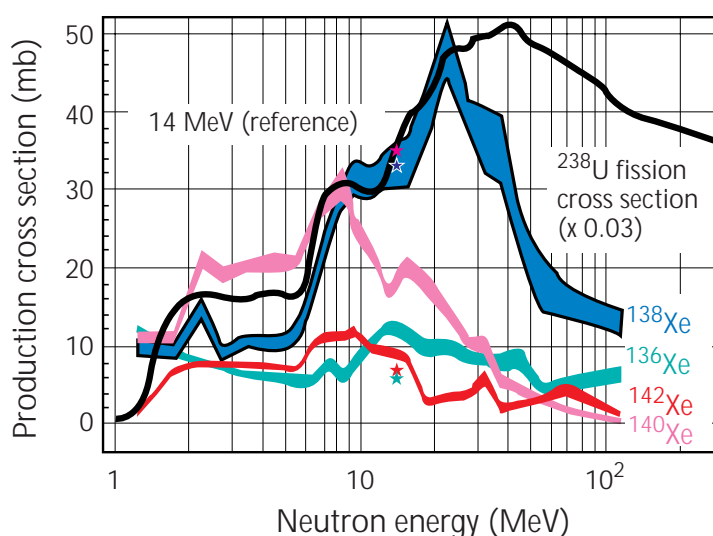
↑ Fig. 4. *Fission-fragment-production cross sections for 4 isotopes of xenon obtained from the 2+ to 0+ γ-ray transitions, assuming that all fragments emit the 2+ to 0+ γ-ray (i.e. neglecting those fragments formed in the ground state and assuming all decays cascade through the 2+ state.) The stars represent the values of the 14-MeV evaluated data.*
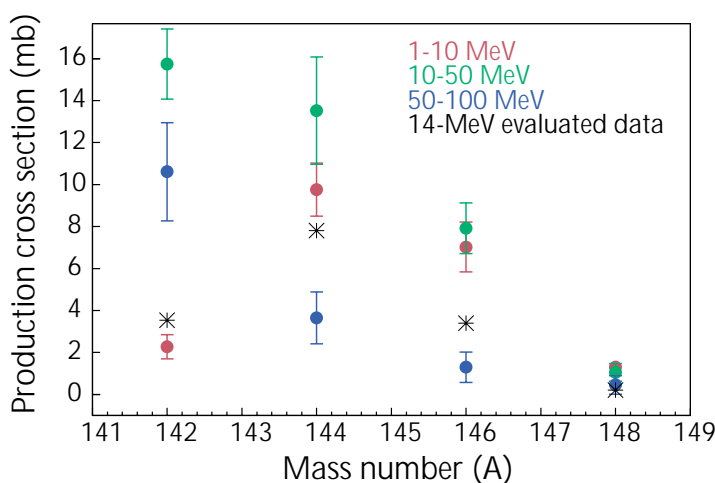
↑ Fig. 5. *Fission-fragment-production cross sections for 4 barium isotopes from neutron-induced fission of ^{238}U are shown for three incident-neutron energy bins. The black asterisks represent the evaluated data at 14 MeV. The average neutron energies in the bins are 4 (for the 1-10 MeV bin), 25 (for 10-50 MeV bin), and 72 MeV (for the 50-100 MeV bin).*

shift toward lighter isotopes with increasing incident neutron energy is observed. This shift occurs because of the increased neutron emission at all stages of the reaction.

With the unique neutron beams and detector facilities at LANSCE, the actinide fabrication and handling capabilities at Los Alamos National Laboratory, and the fission detectors and actinide sample fabrication

resources of the Commissariat à l'Energie Atomique in France, we can perform new and detailed studies of fission for defense, basic, and applied research. Our first studies of ^{235,238}U have shown in detail the transition from asymmetric to symmetric fission as a function of excitation energies, and they provided fission-fragment yields over a wide incident-neutron-energy range. We plan to extend these studies to ^{239}Pu, to other actinides, and to lighter nuclei soon. With the high neutron energies available at WNR, we can investigate fission at high excitation energies. These studies would include bismuth, lead, gold, and even lighter nuclei, which do not fission at lower excitation energies. This work will help with our basic understanding of fission and has direct application to advanced accelerator-based systems for nuclear waste transmutation and power generation.

References

1. O. Hahn and F. Strassmann, "Concerning the Existence of Alkaline Earth Metals Resulting from the Neutron Irradiation of Uranium," *Naturwissenschaften* **27**, 11 (1939); H.G. Graetzer (translation), *American Journal of Physics* **32**, 10 (1964).
2. L. Meitner and O.R. Frisch, "Disintegration of Uranium by Neutrons: A New Type of Nuclear Reaction," *Nature* **143**, 239 (1939).
3. N. Bohr and J.A. Wheeler, "The Mechanism of Nuclear Fission," *Physical Review* **56**, 426-450 (1939).
4. P. Moller, D.G. Madland, A.J. Sierk, and A. Iwamato, "Nuclear Fission Modes and Fragment Mass Asymmetries in a Five-Dimensional Deformation Space," *Nature* **409**, 785-790 (2001).
5. J.F. Berger, personal communication (2001); J.F. Berger, M. Girod, and D. Gogny, "Microscopic Analysis of Collective Dynamics in Low-Energy Fission," *Nuclear Physics A* **428**, 23 (1984).
6. R. Vandenbosch and J.R. Huizenga, *Nuclear Fission* (Academic Press, Inc., New York, 1973).
7. *The Nuclear Fission Process*, C. Wagemans, Ed. (CRC Press, Boca Raton, Florida, 1991).
8. W. Younes *et al.*, "Transition from Asymmetric to Symmetric Fission in the ^{235}U(n,f) Reaction," *Physical Review C* **64**, 054613 (2002).

Single-Event-Effects Measurements at the LANSCE Irradiation of Chips and Electronics House

B.E. Takala (LANSCE Division)

The Los Alamos Neutron Science Center (LANSCE) Irradiation of Chips and Electronics (ICE) House is located on the 30° left flight path (FP) of the high-energy neutron source at the Weapons Neutron Research Facility (WNR). The shape of the neutron spectrum on this FP is very similar to the spectrum of neutrons produced in the atmosphere by cosmic rays, but with a flux more than 5 orders of magnitude higher (Fig. 1). This large neutron flux allows testing of semiconductor devices at greatly accelerated rates in which one hour of exposure at LANSCE is equivalent to more than 100 years of flight time.
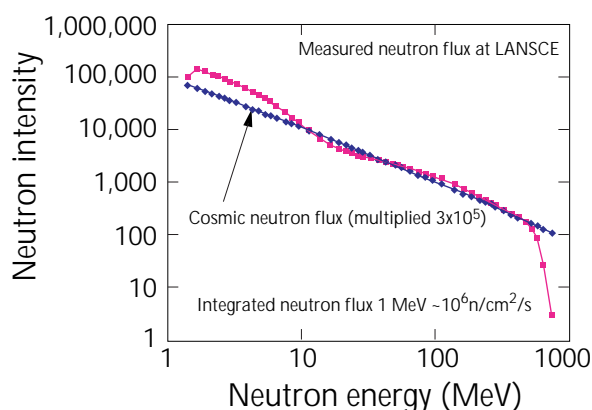

↑ Fig. 1. *The LANSCE neutron spectrum is very similar to the cosmic-ray-induced neutron spectrum but with a flux more than 5 orders of magnitude.*

Testing neutron-induced single-event effects (SEE) is important because neutrons have been recognized as a significant threat to semiconductor devices at aircraft altitudes. Since WNR was first demonstrated as an effective SEE testing tool in 1992, a growing number of companies from around the world continue to use the WNR high-energy-neutron source to study various failure modes caused by neutron radiation. The ultimate goal of this research is to find ways to overcome the effects of incoming galactic- and solar cosmic-ray-induced neutrons.

Effects of Neutrons Produced in Space

Galactic and solar cosmic rays collide with nuclei in the upper atmosphere creating a shower of subatomic particles. The charged-particle components of the cosmic-ray shower are strongly absorbed by the atmosphere, but the neutrons are able to reach aircraft altitudes and below because they have no charge.

These energetic incoming neutrons penetrate semiconductor devices and collide with the atoms in the material, causing charged recoils (i.e., from neutron and atom collisions) and the production of secondary particles (e.g., protons, electrons) that deposit charge and energy in the devices (Fig. 2). This charge deposition can initiate so-called SEEs in semiconductor devices that can seriously affect their performance.
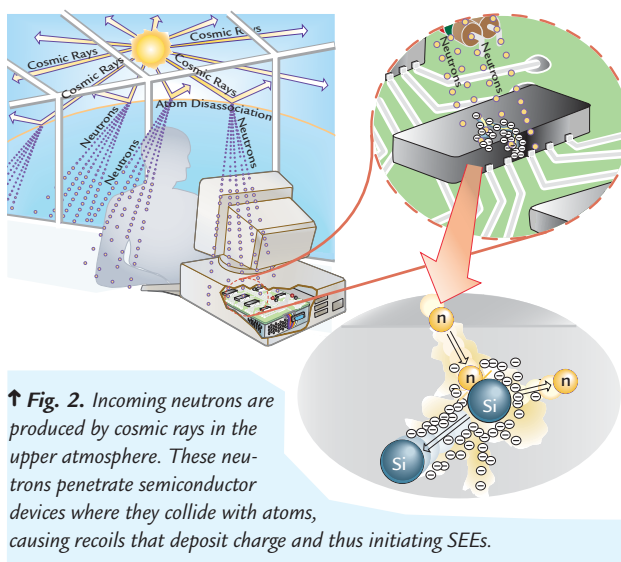
↑ Fig. 2. *Incoming neutrons are produced by cosmic rays in the upper atmosphere. These neutrons penetrate semiconductor devices where they collide with atoms, causing recoils that deposit charge and thus initiating SEEs.*

SEEs include single-event upsets (SEUs), multiple-event upsets (MEUs), single-event latchup, single-event burnout, and gate rupture. SEUs occur when a memory location changes its state because of charge deposited by an energetic particle. SEUs typically occur at a rate of approximately one upset per billion bits per hour at aircraft altitudes. Although this type of failure may be corrected by error checking, increased costs and a loss of performance are associated with this solution. MEUs, where several memory locations are altered, have been measured to be a few percent of the single-event rate. MEU failures are more difficult to correct than SEUs. Failures such as latchup in which a device ceases to function are more serious because they usually require turning the device off and then on to eliminate the latchup. Other more serious failure modes occur in high-power devices in which a neutron can initiate a cascade of charged particles that causes these devices to draw large currents—possibly permanently damaging them as a result. The failure rate in these devices strongly depends on the amount of applied voltage. The failure rate increases dramatically above a critical threshold voltage that may be significantly less than the rated voltage of the device.

Advantages of Testing in the ICE House

The ICE House provides experimenters with several advantages over other testing methods. Unlike heavy-ion tests where a device must have its case material removed and placed in vacuum to permit particles to reach the sensitive regions of the chip, testing in the ICE House beam permits normal operation of the device in the open air. In fact, because neutrons are not strongly absorbed by the device, several devices may be placed in the neutron beam at once, one behind the other.

The integrated neutron flux at the ICE House is approximately 10^6 neutrons/cm^2/s for energies above 1 MeV. No other facility in the world can offer this intensity with a spectrum matching the natural atmospheric spectrum so closely. Because this flux is achieved with approximately 35,000 individual neutron pulses due to the time structure of the accelerator proton beam, the results are still representative of atmospheric results because the probability of multiple neutron events is exceedingly low for individual pulses with so few neutrons.

Research Conducted During 2001

Listed below with some of their research goals are some of the organizations that used the ICE House beam in the 2001 run cycle.

- **Aerospatiale Aeronautique.** Validating and characterizing (1) new avionics systems using synchronous dynamic random-access memory protected by error detection and correction and (2) 0.6-μm and 0.25-μm static random-access memory (SRAM) to confirm a new theoretical model.

- **Altera Corporation.** Testing several new programmable logic devices for neutron-soft-error sensitivity.

- **Honeywell.** Determining failure rates of several types of fielded SRAM, comparing failure rates to past field history, and studying SEE in programmable-logic-device (PLD) circuits.

- **Infineon Technologies.** Developing memory-module testing techniques.

- **Intel Corporation.** Evaluating various designs of microprocessor circuitry for their sensitivity to high-energy neutrons and of soft-error-rate modeling for the latest products and processing technologies.

- **LSI Logic Corporation.** Evaluating the interplay between critical charge, sensitive volume for static storage nodes, and the associated neutron-soft-error cross section for 0.18-μm complementary-metal-oxide-semiconductor SRAM and PLD circuits.

- **Prairie View A&M University.** Studying items such as SRAM, carbon-nanotube materials,

metal-oxide-semiconductor transistors, metal hydride shielding, and spacesuit fabric.

- **Sandia National Laboratories, Lucent Technologies, and Bell Laboratories.** Characterizing neutron-induced SEU in advanced Lucent memory and logic technologies, performing modeling to identify design or process fixes, and investigating upset trends in three integrated circuits of decreasing feature size.

Recent Trends in Neutron-induced SEE Research

In addition to continuing research efforts into traditional memory upsets, new issues emerged from recent work. Effects on logic nodes in field-programmable gate arrays are being widely studied. The relationship between failure rates and feature size is hotly debated. Where some experimenters had predicted the SEE problem to worsen with decreased size, failure rates have remained relatively constant or even decreased. However, some mitigation methods have not shown the predicted improvements. Over all, predictions from computer codes have become unreliable. Clearly, either something new is taking place in the chips or traditional analysis is no longer appropriate. Research opportunities in the field are abundant at this time.

Developing a Los Alamos National Laboratory SEE Research Program

LANSCE believes there is an opportunity to grow our research participation in SEE. An ICE workshop was held in July 2001 to discuss LANL capabilities and interests and to consider paths for growth. LANSCE is aggressively seeking collaborators in this development effort. Sandia National Laboratories, the National Aeronautics and Space Administration, and the Federal Aviation Administration have all expressed interest in exploring a significant research facility based on the LANSCE WNR neutron beam. LANSCE is also exploring the idea of participating on electronics standards committees such as the Joint Electron Device Engineering Council, which has drafted a testing/performance standard for neutron-induced SEE.

Summary

Neutron-induced SEEs are again emerging as a significant threat to semiconductor electronics. LANSCE, through the new ICE House, is uniquely positioned to address this problem for the electronics industry and the nation. Valuable research at the forefront of the field is being conducted at the LANSCE ICE House where new research opportunities are being uncovered. LANSCE is aggressively pursuing collaborators to develop a SEE research program at Los Alamos National Laboratory.

Research Highlights

Irradiation Experiments to Support the Advanced Accelerator Applications Program

R.T. Klann (Argonne National Laboratory), E.J. Pitcher, S.A. Wender, K.A. Woloshun, V. Tcharnotskaia (LANSCE Division), G.L. Morgan, M.A. Paciotti (P Division), J.M. Oostens (AAA-TDO), M.R. James (D Division)

The Advanced Accelerator Applications (AAA) program has been tasked by the Department of Energy with the design of an accelerator-driven facility to transmute radioactive waste. A subcritical system coupled to a high-energy accelerator, which contains large quantities of minor actinides to be incinerated, is unlike any other system ever assembled. This system poses significant technical challenges that must be overcome before a large-scale facility can be built. A research and development program, which has been established to accomplish this mission, includes the development of several experimental facilities to study fuel development, structural-materials and system integrity, facility operations and control, and the physics of coupled systems.

In support of the research and development program, a series of experiments at LANSCE were identified to address pertinent issues related to corrosion of structural materials, target-neutron-yield data, and basic cross sections. In 2001, we began the following irradiation experiments: (1) the study of the influence of proton irradiation on the corrosion kinetics of structural materials in lead-bismuth coolant systems, (2) the study of high-energy-neutron leakage from a lead-bismuth spallation target (discussed in this research highlight), and (3) the measurement of cross sections for sodium activation by protons.

Neutron Leakage from a Spallation Target

Spallation-neutron sources produce neutrons whose energies extend up to the incident-proton energy. In the design of accelerator-driven waste transmuters, the high-energy neutrons that leak from the spallation target have three practical implications: (1) the incident neutrons lead to the production of secondary neutrons in the fuel region, (2) the neutrons have the largest range of all other particles in materials, and (3) the production of H and He atoms in the steel structural elements are dominated by high-energy neutron reactions. This H and He gas production limits the lifetime of structural materials near the target. To reduce this gas production in the multiplier region, a "buffer" made of high-atomic-mass material can be placed

between the target and the multiplier to attenuate the leakage of high-energy neutrons from the target into the multiplier. Experimental verification of expected flux distributions in the multiplier is envisaged as a function of buffer and target sizes.

Ongoing experiments will measure high-energy neutron and proton distributions as a function of target radius (i.e., radii of 5 cm, 10 cm, and 20 cm) for a lead-bismuth target with a target length of 50 cm. The data obtained from these experiments will be used to generate a high-energy-physics benchmark (using a basic geometry, as well as verifiable system parameters) and to validate the Monte Carlo code MCNPX. In addition, the data will allow the evaluation of the effectiveness of a buffer in modifying the leakage of high-energy neutrons from the spallation target.

Measurements being performed use time-of-flight (TOF) and activation-foil techniques. Each technique offers basic nuclear data that cannot be achieved by the other technique—that is, the techniques provide similar but complementary data regarding the spectra and spatial distribution of the neutrons emanating from the spallation target. In the TOF technique, the timing of individual events is accurately recorded to subsequently recreate the emitted-neutron spectra. The times of 800-MeV proton pulses striking the target are recorded. Some neutrons emitted from the target travel down the beam tube and interact with the detector. Their arrival time at the detector is recorded, and their velocity and energy is then determined. Summing many events, an energy spectrum of the neutrons interacting with the detector is obtained. This technique provides very detailed spectral information for a discrete emission angle and target position.

With the activation-foil technique, foils are placed at specific locations on the surface of the target. During proton irradiation of the target, neutrons are produced from spallation and other reactions. Neutrons, with a wide range of energy and angle, are emitted from the target and interact with the foils in specific reactions with known probabilities (cross sections) to create radioactive species. The foils are then removed after a given irradiation period, and the gamma (γ) ray emissions from the foils are counted to determine the amount of activity created by the neutron reactions.

Knowing the cross sections for these reactions, the energy spectra of the neutrons that caused the interactions can be determined from the data (also known as spectral unfolding). The energy spectra thus obtained are not as detailed as the spectra created from the TOF measurements; however, the spectra are for a specific location on the target and include all emission angles. For this reason, the two techniques are complementary to each other.

In December 2001, we conducted irradiations of a 20-cm-diam, 50-cm-long lead-bismuth target (Fig. 1) with an 800-MeV proton beam. The lead-bismuth target was located in the Blue Room (Target 2) at the Weapons Neutron Research Facility (WNR). Two flight paths (FPs) (at 7.5° and 30° relative to the incident proton beam) were re-commissioned to perform the TOF measurements. The activation foil packets that were assembled contained the following elements: Bi, Nb, In, Co, Ni, Cu, Fe, Al, Au, Rh, Ti, Zn, Lu, and Tb. The foil packets were mounted at the 0-, 5-, 10-, 20-, 30-, 40-, and 50-cm positions along the top of the target (Fig. 1a) and at 90° intervals around the target at the 10-cm location.

Analysis of the results will continue through 2002 and into 2003. Initial analysis of the activation foil and TOF data indicates that both techniques produced statistically significant data that can be used to compute neutron spectra. One set of the initial TOF counts is shown in Fig. 2. Identification of γ-ray peaks from the irradiated foils indicates that many of the expected products are present. For example, products from (n,xn) reactions on the bismuth foil reveal that all reactions up to x = 11 are present. The thresholds for the (n,xn) reactions begin at about 14 MeV and step up in energy by 8 to 10 MeV for each higher-x reaction. This is significant because a single bismuth foil can provide results for many reactions each with an independent value for the total flux above threshold. For example, results for the (n,8n) reaction give the total flux above 54.24 MeV (the threshold value).

(a)

Activation foils

Phosphor

02/12/2001 11:56

(b)

30° flight path

7.5° flight path
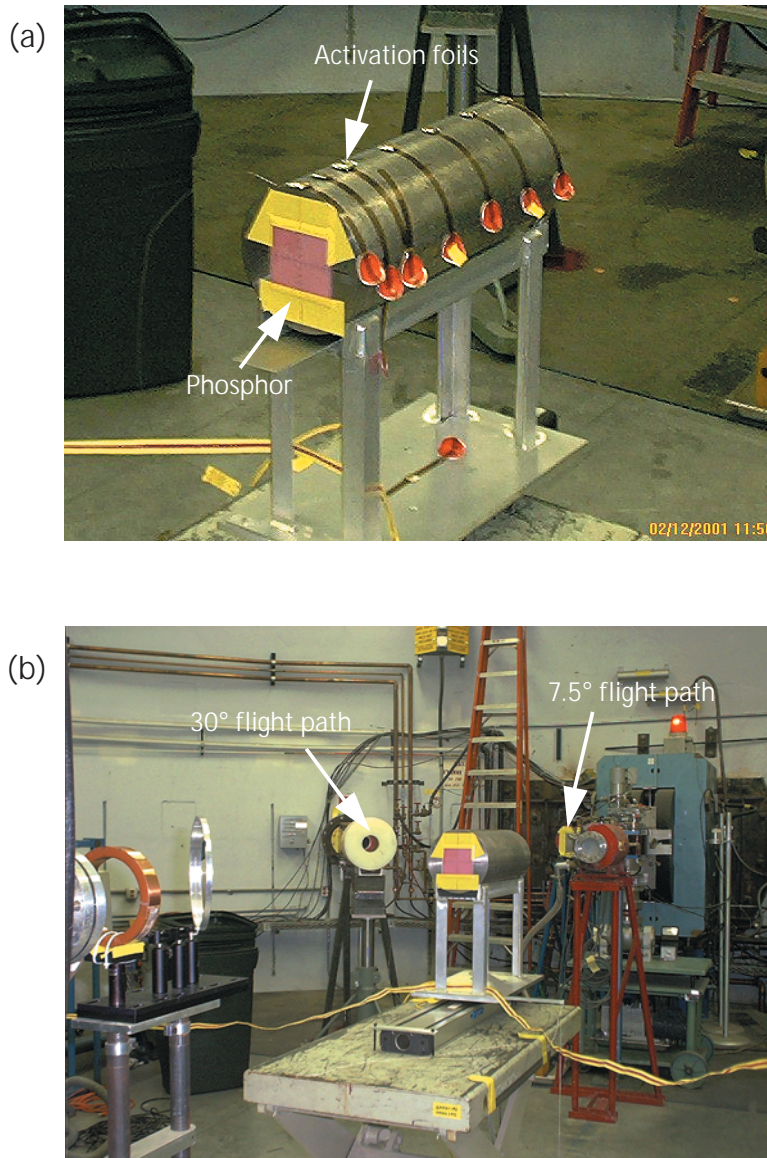
↑ **Fig. 1.** *(a) This image of lead-bismuth target shows the mounted phosphor and foils. (b) This larger image shows target positions and collimators for the 7.5° and 30° FPs in the WNR Target 2 Facility where the experiments were conducted.*

Fig. 3 shows the measured activity of ^{207}Bi and ^{206}Bi in the bismuth foils (normalized) in comparison to the total neutron flux above 20 MeV calculated using MCNPX (also normalized). ^{207}Bi is created from the (n,3n) reaction with a threshold of 14.42 MeV and ^{206}Bi is created from the (n,4n) reaction with a threshold of 22.55 MeV. So the thresholds are comparable to the MCNPX calculations with an energy tally boundary of 20 MeV. The measured activities are in
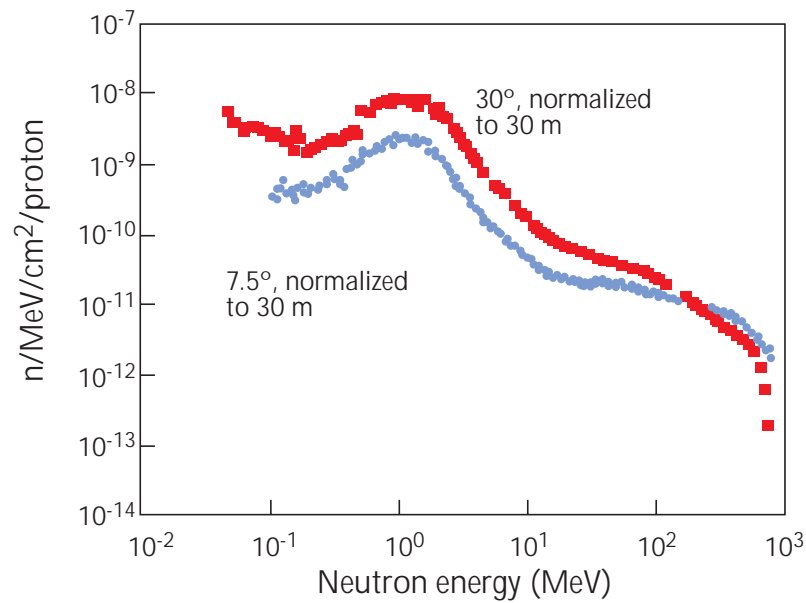
↑ **Fig. 2.** *Neutron-energy spectra at angles of 7.5° and 30° with respect to the incident-proton beam. The lead-bismuth target was positioned with the front face of the target at the intersection of the proton beam line and the neutron FPs.*
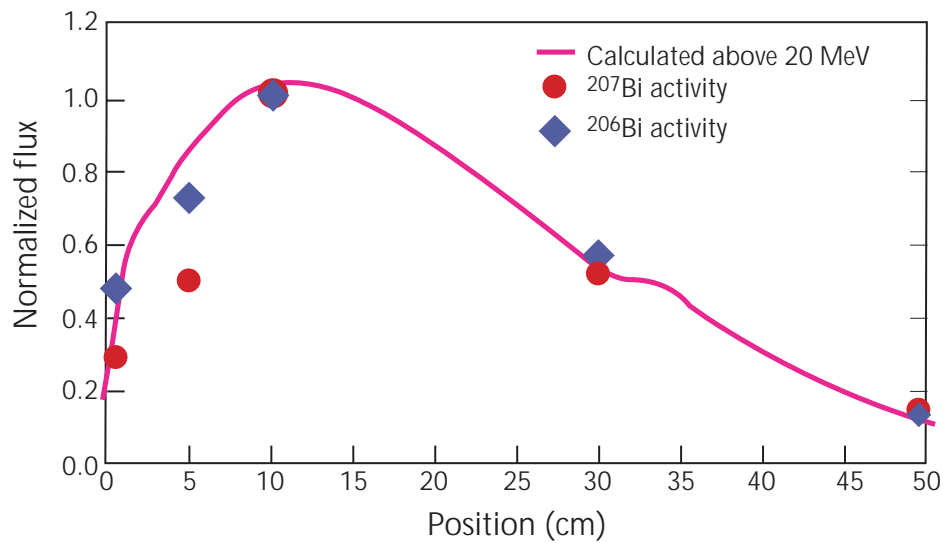
↑ **Fig. 3.** *This preliminary result compares the measured* ^{207}*Bi and* ^{206}*Bi activities to the calculated total neutron flux 20 MeV. Values are normalized to 1.0 at the 10-cm location.*

reasonable agreement with the calculated flux, even though the activities have not been corrected for spectral variations along the length of the target. In addition, the measured activities demonstrate a consistent trend along the length of the target.

Summary

Our experiments in support of the AAA program are designed to address key technical issues for the target and buffer design of an accelerator-driven transmutation of waste system. The proof-of-concept measurements and initial target irradiations performed in 2001 are still being analyzed. First analysis of the data indicates that the Target 2 Facility at WNR can support the AAA program and produce useful data for the project. These experiments will continue in 2002 and 2003.

Research Highlights

What is the "Color" of Atomic Nuclei?

A. Schiller, J.A. Becker, L.A. Bernstein, P.E. Garrett, T.S. Hill, D.P. McNabb, W. Younes (Lawrence Livermore National Laboratory), E. Tavukcu (North Carolina State University), A. Voinov (Frank Laboratory of Neutron Physics), M. Guttormsen, J. Rekstad, S. Siem (University of Oslo), R.C. Haight, R.O. Nelson (LANSCE Division)

Color, as humans perceive it, depends on electromagnetic properties of matter in the narrow band of optical wavelengths. White objects scatter all optical wavelengths; black objects absorb them. Colored objects, like a blue ball, absorb some wavelengths (e.g., red light) but scatter others (e.g., blue light). The sky appears blue because the blue component of the sunlight is scattered by molecules of the atmosphere—but it makes the sun, on the other hand, appear yellow. Some animals can perceive electromagnetic waves that humans cannot. Bees, for example, can see in the near ultraviolet light. We can only speculate what impression of "color" this makes.

Atomic nuclei are very small (~ 10^{-15} m in radius) compared to optical wavelengths (~ 5×10^{-7} m). Therefore, interaction (scattering or absorption) of electromagnetic waves by atomic nuclei is generally negligible for optical wavelengths but becomes important for much shorter wavelengths comparable to the atomic-nucleus size. Electromagnetic waves of such short wavelengths are called gamma (γ) rays and are usually characterized by their quantum energy rather than by their wavelength. If γ-rays were visible to the human eye, we would see different nuclei in different colors because they absorb/scatter electromagnetic waves differently. Investigating the color of atomic nuclei is interesting from a basic-science point of view. But model calculations of nuclear reaction probabilities (cross sections) also benefit from knowledge of the color of specific nuclei—at least when electromagnetic quanta are participants in the nuclear reaction under study.

Electric and Magnetic Dipoles

Different kinds of electromagnetic radiation can be observed in atomic nuclei. The simplest ones are electric- and magnetic-dipole radiation. An electric dipole is a simple configuration of a positive and a negative charge, whereas a magnetic dipole is a loop current (Fig. 1). Electromagnetic radiation is produced when the dipole moments begin to oscillate. The difference between electric- and magnetic-dipole radiation is very subtle. The electric dipole viewed in a mirror in Fig. 1 (lower panel) looks as though the positive and negative charges have been interchanged. Thus, the electric-dipole moment (d, vector) changes direction in the mirror image, and we say that the electric dipole has "negative parity." The loop current viewed through a mirror is indistinguishable from the original loop current. Therefore, the magnetic-dipole moment (m, vector) does not change direction in the mirror image, and we say that the magnetic dipole has "positive parity."

In atomic nuclei, an electric dipole occurs when protons and neutrons become separated. The protons in this case are then more positively charged than the
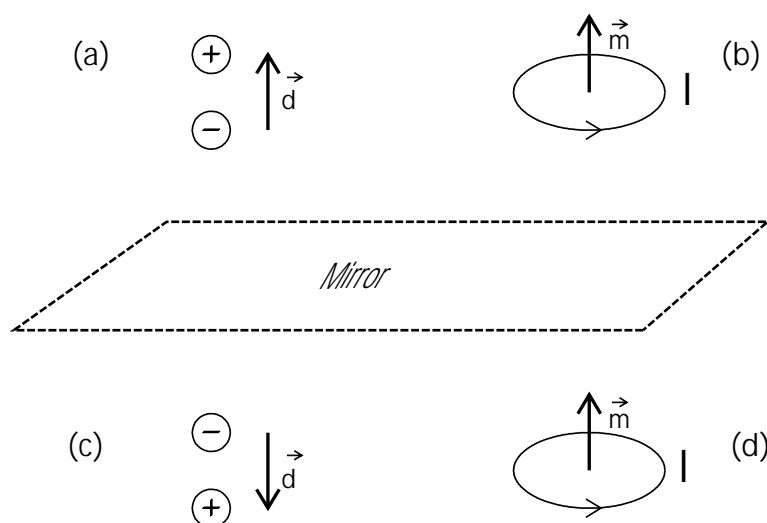

↑ **Fig. 1.** *(a) The electric dipole moment (d, vector) points from the negative charge to the positive charge. (b) The magnetic dipole moment (m, vector) is perpendicular to the loop current (I). The direction of the magnetic dipole moment is defined such that the loop current circulates counter-clockwise around the magnetic dipole moment. Seen through a mirror, the electric dipole moment changes direction (c), whereas the magnetic dipole moment does not (d).*

average nuclear matter, and, as shown in Fig. 1, they take the place of the positive charge. The neutrons, on the other hand, are more negatively charged than the average nuclear matter, and they take the place of the negative charge. The neutrons and protons will oscillate against each other at a certain frequency and therefore give rise to a huge resonance in the absorption spectrum of electromagnetic radiation. This resonance is located at the oscillation frequency of the protons against the neutrons and is called giant electric-dipole resonance (GEDR) (Fig. 2).

Magnetic dipoles can be realized as (1) the circular motion of a charged particle (proton) orbiting around the center of the nucleus (i.e., orbital magnetic moment) or as (2) the spinning of a particle around itself (i.e., spin magnetic moment). The orbital magnetic moment can be understood in terms of classical mechanics, whereas the spin magnetic moment is a pure quantum effect. In any case, the circular orbital motion on the one hand or the spinning around itself on the other hand takes the place of the loop current in Fig. 1. The spin magnetic moment will start oscillating because the spinning axis is flipped in the nucleus with a certain frequency ν_1 due to the influence of the spin-orbit term of the nucleon-nucleon force. As a result, we get the spin flip or giant magnetic-dipole resonance (GMDR) as a second resonance in the absorption spectrum of electromagnetic radiation (Fig. 3). The GMDR is generally weaker (by ~ 2 orders of magnitude) than the GEDR, and the resonance frequency of the GMDR is lower (by ~ 30%) than that of the GEDR. The orbital magnetic moment is discussed in the Fig. 4 caption.
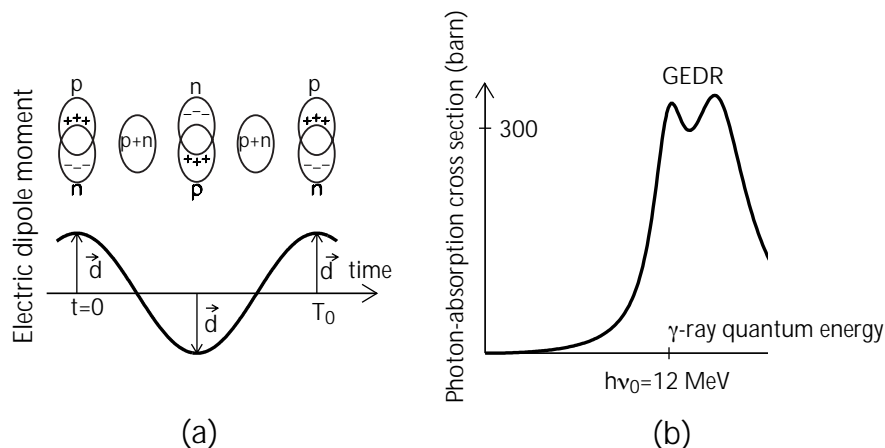
Fig. 2. *(a) The oscillation of protons versus neutrons in the nucleus and of the connected electric-dipole moment (d, vector) with an oscillation frequency $\nu_0 = 1/T_0$. (b) Resulting photon-absorption cross section with an electric-dipole resonance (GEDR) at the frequency ν_0. The numerical value is for the ^{172}Yb nucleus. The GEDR is double peaked because the ^{172}Yb nucleus is deformed.*
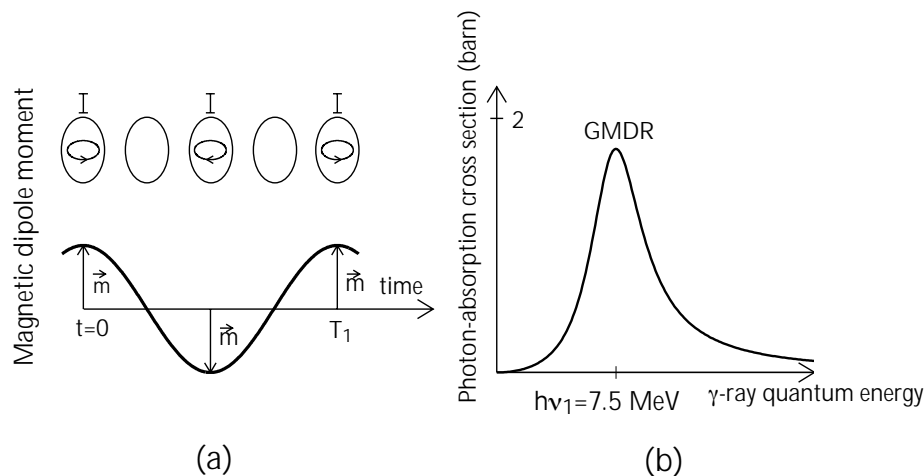
Fig. 3. *(a) Oscillation of the spin magnetic-dipole moment [m, vector; also represented by the loop current (I)] with respect to time. This oscillation is due to the flipping of the spinning axis with a frequency $\nu_1 = 1/T_1$. (b) Resulting photon-absorption cross section showing a magnetic-dipole resonance (GMDR) at the frequency ν_1. The numerical value is for the ^{172}Yb nucleus.*

Experiment

In a previous experiment, we measured the total γ-ray absorption spectrum by the nucleus ^{172}Yb at the Olso Cyclotron Laboratory in Norway.[1] (The actual measured quantity is the total radiative strength function, which is proportional to the absorption spectrum.) This absorption spectrum, from which the γ-ray strength function was obtained, can be described by the sum of the GEDR and GMDR and a third,

unknown resonance, which is even weaker and centered at lower frequencies than the GMDR. Our group[2] speculates whether this small resonance is that of the orbital magnetic moment (also called the scissors mode), whereas another group[3] speculates about the possibility of a weak electric-dipole resonance at these low frequencies—called the pygmy resonance. These two competing speculations are depicted in Fig. 4.

To test these hypotheses, we excited the ^{172}Yb nucleus by thermal-neutron capture on ^{171}Yb using flight path 14 at the Lujan Neutron Scattering Center. This excitation mechanism has the advantage that the energy and parity of the initial state are well determined. We then recorded the spectrum of γ-ray cascades populating a given low-lying level in ^{172}Yb by only two γ-ray

transitions. The chosen low-lying level has a parity that is opposite to that of the initial level. This means that the de-excitation by two γ-ray transitions has to involve one electric- and one magnetic-dipole transition. The sum of energies of both γ-ray transitions obviously has to match the energy difference between the initial state and the low-lying level, whereby we identify such special decay processes. The two γ-ray transitions also have to be observed within a short coincidence window of a few 10^{-9} seconds. The intensity and the spectral distribution of the two γ-ray transitions will tell (by means of a difficult-to-explain calculation) whether the third resonance structure at low frequencies is of electric- or orbital magnetic-dipole character (Fig. 5).
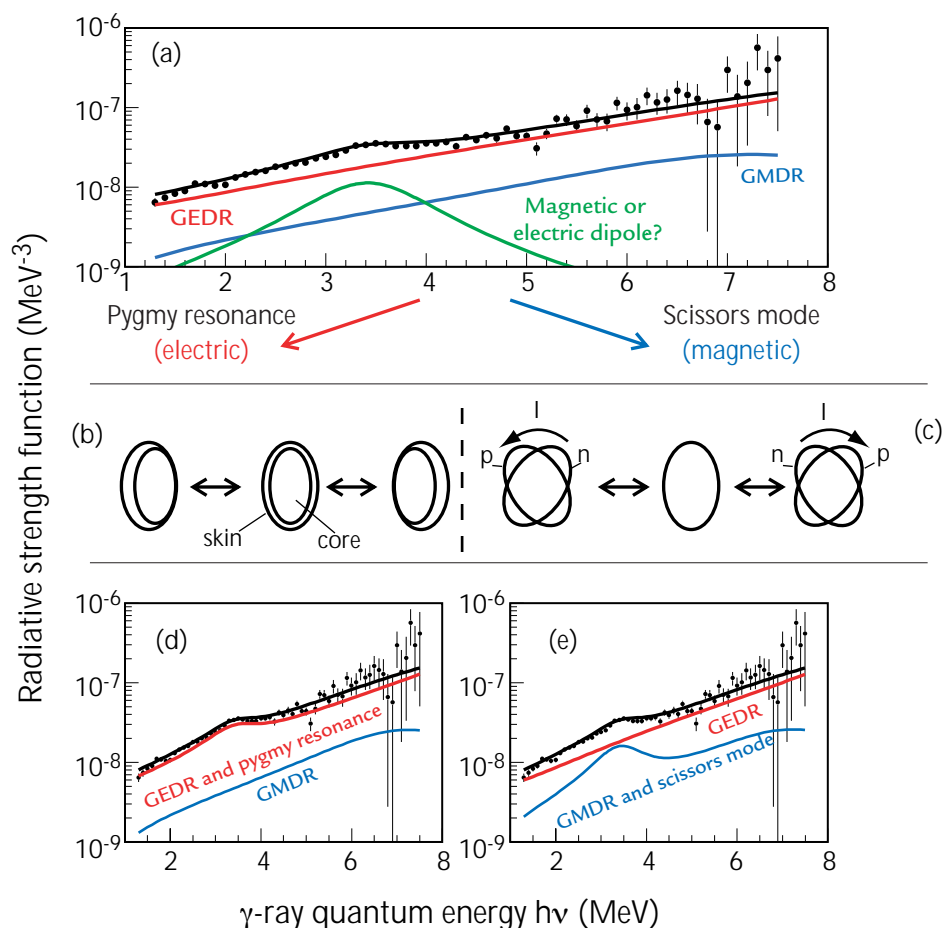
↑ **Fig. 4.** (a) Total radiative-strength function of ^{172}Yb (data points).[1] This strength function can be described as an incoherent sum of the GEDR (red line), the GMDR (blue line), and a third resonance (green line) at lower energy with unknown multipolarity. If this third resonance were of the electric-dipole character (pygmy resonance), it would correspond to a vibration of the neutron skin relative to a core of protons and neutrons (b). If the resonance were of the orbital-magnetic-dipole character (scissors mode), it would correspond to a counter-wise angular vibration of the protons and neutrons (c) much like the movement of scissors. In any case, this low-energy resonance has to be added either to the already known GEDR (d) or GMDR (e) to give the total electric- or magnetic-radiative-strength function.
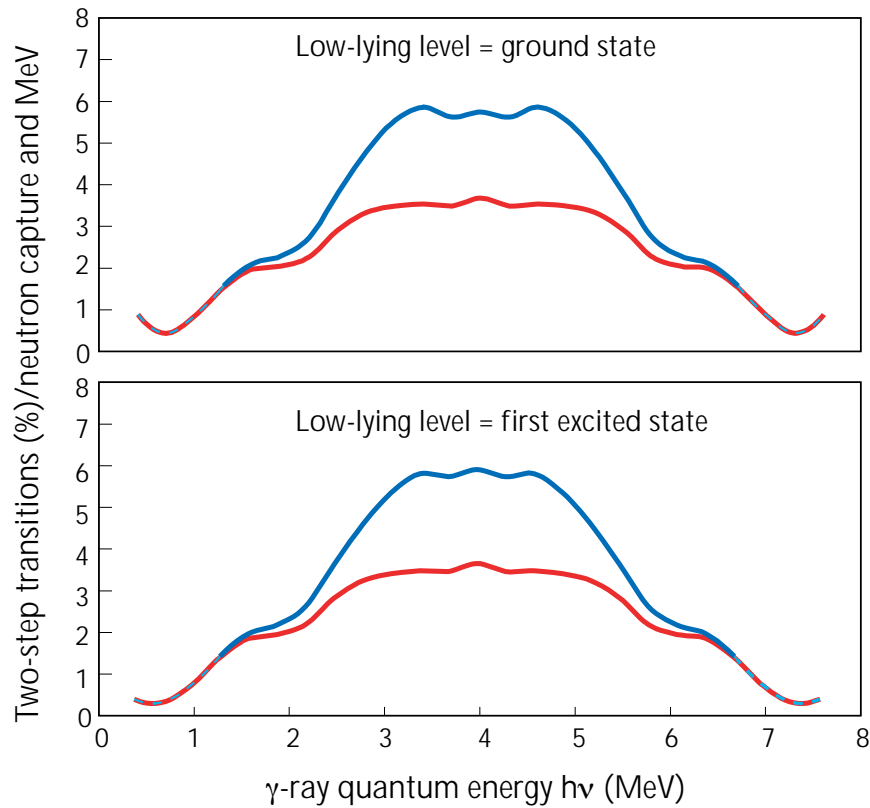
↑ Fig. 5. *(a,b) Anticipated spectral energy distribution of the two γ-ray transitions after neutron capture. If the unknown resonance is an electric-dipole resonance (pygmy resonance), we expect our data points to lie on the red lines. If it is an orbital-magnetic-dipole resonance (scissors mode), we expect our measurement to follow the blue lines. The spectral distribution must be symmetric because the energies of both γ-ray transitions have to add up to the energy difference between the initial state and the chosen low-lying state in the ^{172}Yb nucleus.*

Conclusion

Preliminary results already show that we collected enough statistics in this experiment to yield a meaningful spectral distribution of two-step γ-ray transitions. Analysis of the data continues. We soon hope to fill Fig. 5 with data points, favoring either the hypothesis of an electric-dipole resonance (i.e., pygmy resonance, red line) or an orbital-magnetic-dipole resonance (i.e., scissors mode, blue line).

References

1. A. Voinov *et al.*, "γ-ray Strength Function and Pygmy Resonance in Rare Earth Nuclei," *Physical Review C* **63**, 044313 (2001).
2. A. Schiller *et al.*, "Observation of the Scissors Mode in the Quasi-Continuum," Los Alamos National Laboratory preprint (http://xxx.lanl.gov/abs/nucl-ex/0011018).
3. P. Van Isacker *et al.*, "Effect of the Neutron Skin on Collective States of Nuclei," *Physical Review C* **45**, R13 (1992).

Research Highlights

Inclusive (n,xn) Double-Differential Cross-Section Measurements

K. Ishibashi, N. Shigyo, Y. Iwamoto, D. Satoh (Kyushu University), R.C. Haight (LANSCE Division), M. Sasaki, T. Nakamura (Tohoku University)

In calculations of radiation transport with protons and neutrons, it is important to describe processes where one of these nucleons interacts with a nucleus while protons or neutrons are emitted in the reaction. These processes are especially important (although not well known) for incident energies above 20 MeV for programs in accelerator transmutation of waste, radiotherapy, and spallation-neutron-source development. The quantity that describes the probability of emitting a nucleon at a given angle with a given energy is called the double-differential cross section (DDX). For proton-induced reactions, DDX cross sections have been measured for many years. Also there is some information on neutron-induced reactions where protons are emitted in the reaction. But DDX data for neutron-induced reactions where neutrons are emitted are very limited and in fact have never been obtained above 100 MeV. In this research highlight, we describe measurements of inclusive (n,xn) cross sections (i.e., one neutron is detected, but no other reaction product x) for incident-neutron energies ranging from 20 to 400 MeV. The emitted neutrons were detected by the proton-recoil method, using specially designed phoswich detectors (i.e., the phosphor-sandwich technique). Measurements were carried out at the Weapons Neutron Research Facility (WNR) using the time-of-flight (TOF) method. The overall neutron TOF was determined from signals originating from the accelerator proton burst and the phoswich detector. Cross sections thus obtained will be compared to the calculations using the intra-nuclear-cascade-evaporation (INCE) model[1] and the GNASH code.[2]

DDX Data—Needs and Challenges

Intermediate-energy-proton accelerators are used in conceptual accelerator-driven subcritical systems for long-lived nuclear-waste transmutation and in cancer therapy. For these reasons, there is a great deal of interest in cross sections in the intermediate-energy region. To design these facilities, DDX measurements of proton-induced reactions were performed after 1988. These data contributed to improvements to the

following codes: the INCE code, quantum-mechanical-molecular dynamics (QMD) associated with the statistical-decay model code,[3] and the quantum-mechanical pre-equilibrium Hauser-Feshbach code.[2] For instance, predictions from recent INCE calculations have greatly improved compared to the original high-energy transport code developed in the early 1970s. Adjustments to parameters, such as the effective nucleon-nucleon-collision cross sections at medium energies, were made in INCE and QMD codes. Adjustments were also made to the V_0 parameters in the Feshbach-Kerman-Koonin (FKK) formalism.[4]

Proton-induced reactions, however, give limited information about reactions at intermediate incident energies. At these energies, protons induce a cascade reaction that starts from an initial p-n collision in heavy neutron-rich targets. Neutron-induced reactions can play an important role in gaining a better understanding of the whole cascade process. For FKK calculations, data for neutron-induced reactions are required to determine the value of $V_0(p\text{-}p)/V_0(p\text{-}n)$ at the low-energy end of the intermediate-energy region, but this value has so far only been reported at an incident energy of around 100 MeV.

The present state of data suggests that the nuclear-model codes might have trouble predicting DDXs. For example, it is well known that there are relatively important changes in the nuclear-optical potential[5] in the 50- to 300-MeV energy region. The optical-model parameters are important input to the calculations. Secondly, DDX data for proton-induced reactions barely cover this energy range, and therefore they do not constrain the calculations as much as needed. Then there are the thick-target-neutron yields[6] that we measured for incident-proton energies around 1 GeV, and these have some disagreement with the results of the LAHET code[7] in the energy region of several tens of MeV. Thus, even the proton-induced data leave much to be desired in the development of reaction-model codes to predict neutron-induced DDXs.

Measurement of (n,xn) Cross Sections

WNR provides short and intense neutron pulses over a wide continuous-energy range that covers the nuclear-optical-potential changing region. Data at these energies can give information to supplement those for proton-induced reactions for improving the INCE and FKK

calculations. These neutron data can thus provide advances in intermediate-energy nuclear physics that can lead to more accurate neutron-transport calculations for nuclear-engineering purposes.

The purpose of this study is to measure inclusive Fe(n,xn) DDX for incident neutrons with energies from 20 to 400 MeV. The measurement necessitated an experimental method having both an acceptable detection efficiency and an energy resolution suited to the continuous-energy neutron beam.

The experiment was performed on flight path (FP) 4FP15L at WNR. The experimental arrangement is shown in Fig. 1. With a continuous-energy-neutron beam, the time between neutron production from the WNR target and the detector signal gives the sum of the flight times for the incident and emitted neutrons. The TOF of the emitted neutrons can be obtained from its energy measured in the detector. The TOF of the incident neutron is obtained by difference. To detect the emitted neutrons, we use the recoil-proton method. Here, neutrons emitted in the reaction knock out protons from a polyethylene disk, commonly called a "radiator." These recoil protons are detected by a combination of a thin detector (plastic or gas) followed by a thick Na(Tl) crystal. In passing through the thin detector, a recoil proton leaves a small part of its energy in the detector, and this signal is used to identify the particle as a proton. The rest of its energy is deposited in the NaI(Tl) detector—unless the proton exits the crystal either because of its initial direction or because it is scattered out of the crystal.
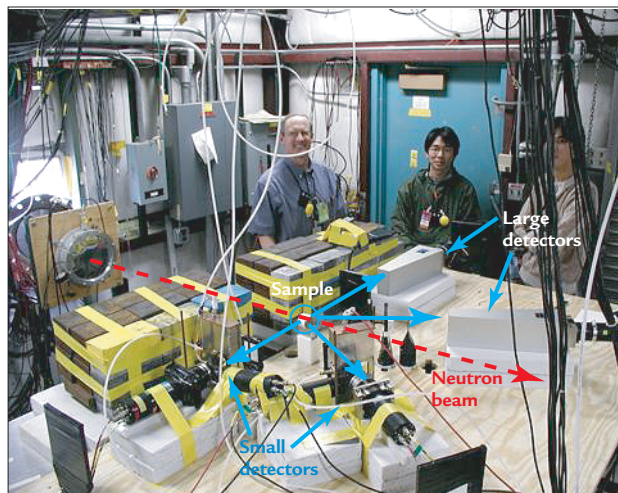

↑ Fig. 1. *Detector arrangement showing the direction of the incident neutron beam, the Fe sample, and the small and large detectors.*

This experiment employed unique detectors whereby an Na(Tl) crystal was integrated into a package with plastic scintillators on the sides of the crystal but not on the entrance face. One photomultiplier tube viewed the total light from both NaI and plastic scintillators. Because the pulse durations of light from these two types of scintillators are very different, we can tell if the light came from the NaI(Tl) crystal alone, or from the plastic alone, or from both. This combination of two types of scintillators with different pulse durations is called a "phoswich." *Good* events are those in which all of the recoil-proton energy is deposited in the NaI(Tl) crystal. If the recoil proton exits the side of the NaI(Tl) crystal, this is a *bad* event; the plastic scintillator gives a signal used to reject the event. Our phoswich detectors have a detection efficiency considerably higher than that of magnetic spectrometers, which cover a relatively narrow energy range, and these phoswich detectors are better suited for simultaneous multi-angle measurements.

To discriminate full- from partial-energy-deposition events in the NaI crystal, two detectors of different sizes were used with NaI(Tl) crystal lengths of 35 cm and 5 cm. These detectors were equipped with radiators having thicknesses of 20 mm and 4 mm for the large and the small detectors, respectively. The distance between the sample and the phoswich detectors was about 50 cm, and the detection angles were 30° and 90°. To subtract events from carbon in the polyethylene radiator, we also made measurements with dummy carbon disks. The sample was a 4-cm-thick, 5-cm-diam Fe disk. To eliminate charged-particle events from the Fe sample, plastic scintillators were set between the sample and the radiators. A plastic scintillator placed behind the phoswich detector was used to eliminate high-energy recoil protons with a range longer than the length of the detector.

Conclusion

Pulse-shape discrimination of events from the NaI(Tl) region from those in the plastic scintillator was clear for the phoswich detector (Fig. 2). The TOF spectra for the large phoswich detector are plotted in Fig. 3. Event rates without the Fe sample were much less than that with the sample in. Counts using the polyethylene radiator were about twice that from the dummy carbon disk. Fig. 4 shows calculated DDX results, with which we will compare the data we are obtaining in this experiment. This calculation is for only one incident neutron energy, and our WNR data will cover all neutron energies from 20 to 400 MeV.
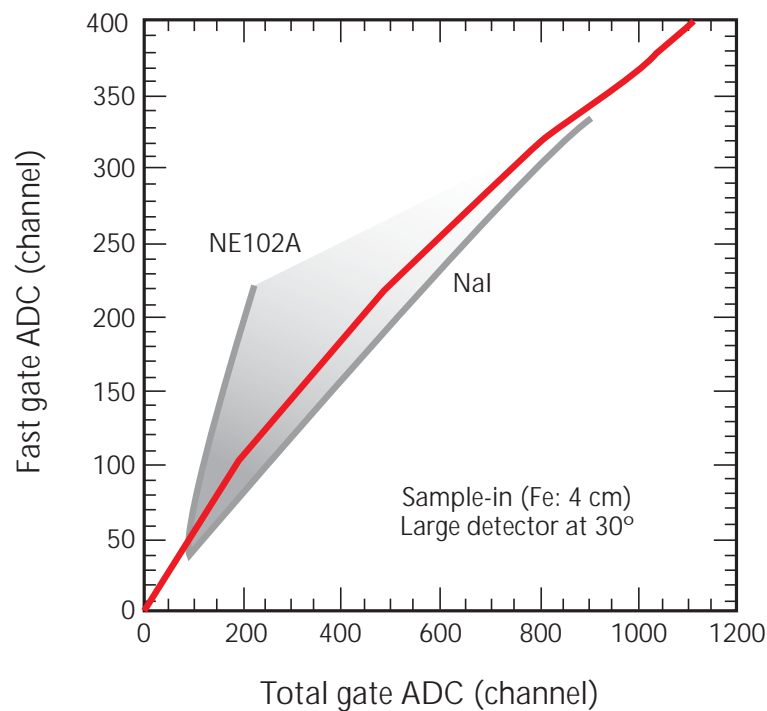
← **Fig. 2.** Pulse-shape discrimination for the large phoswich detector. Two gates are placed on the signal: a fast gate and a total gate. Because of the differences in the pulse durations from the NE102A (plastic) scintillator and the NaI scintillator, we can identify those events that interact only in the NaI detector, those that interact only with the NE102A detector, and those that leave part of their energy in each detector (the region between the curves labeled NE102A and NaI). The good events, namely those that leave all of their energy in the NaI detector, are those below the red curve in the figure. (ADC means analog-to-digital converter.)
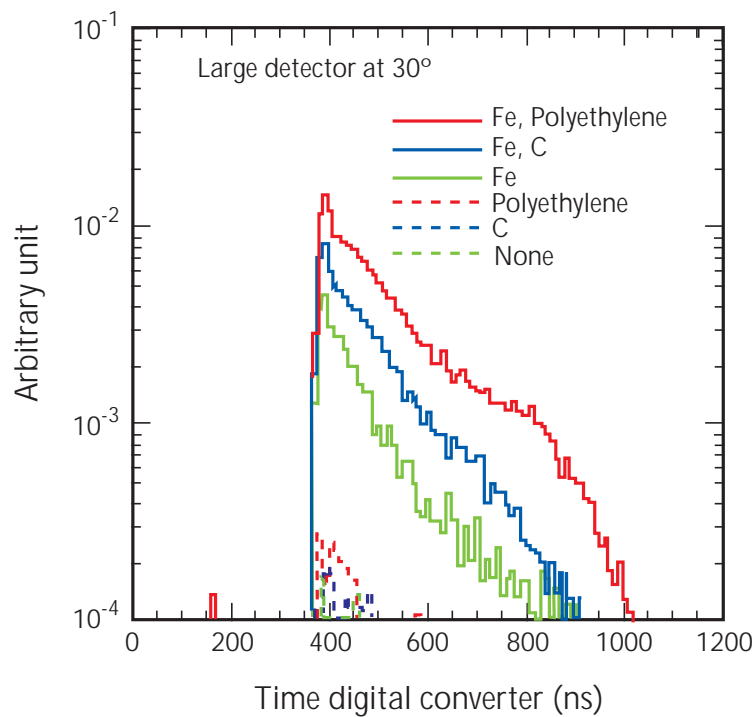
← **Fig. 3.** Neutron TOF spectra for the large phoswich detector. Solid and dashed lines show results of Fe sample-in and -out, respectively. Red, blue, and green lines represent polyethylene radiator data, dummy carbon radiator data, and data with no radiator, respectively.
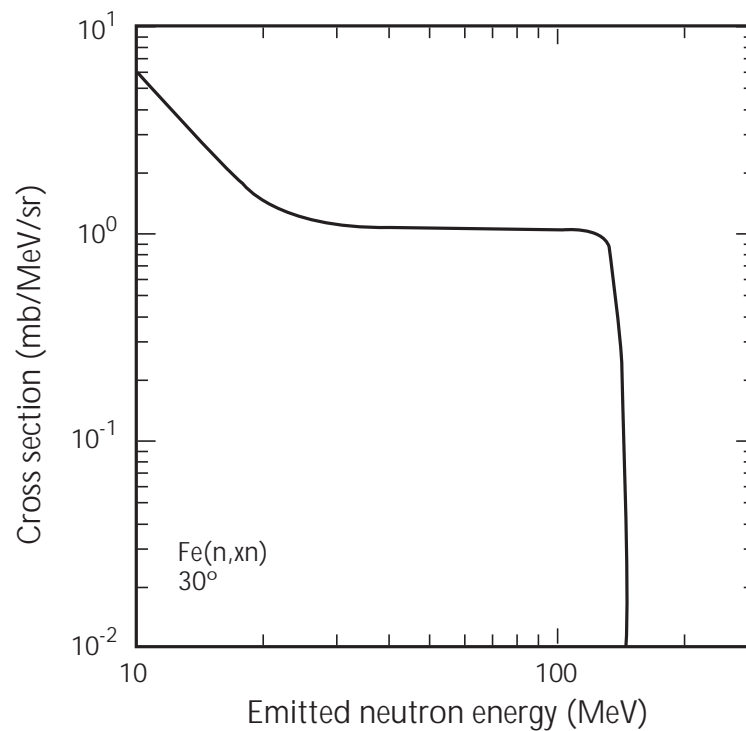
↑ Fig. 4. *Neutron-production DDX as calculated by the GNASH code for one incident neutron energy of 150 MeV. We will test the predictions of this code at this energy and at all energies from 20 to 400 MeV with our experimental data.*

References

1. H. Takada *et al*., "An Upgraded Version of the Nucleon Meson Transport Code: NMTC/JAERI97," Japan Atomic Energy Research Institute report JAERI-Data/Code 98-005 (1998).
2. P.G. Young, E.D. Arthur, and M.B. Chadwick, "Comprehensive Nuclear Model Calculations: Introduction to the Theory and Use of the GNASH Code," Los Alamos National Laboratory report LA-12343-MS (1992).
3. K. Niita *et al*., "Analysis of the (n,xn') Reactions by Quantum Molecular Dynamics Plus Statistical Decay Model," *Physical Review C* **52**, 2620 (1995).
4. W.A. Richter *et al*., "Inclusive (p,p') Reactions on Nuclei in the Mass Range 115 to 181 at Incident Energies from 120 to 200 MeV," *Physical Review C* **54**, 1756 (1996).
5. F.S. Dietrich *et al*., "Recent Measurements of Neutron Total Cross Sections on a Wide Range of Targets from 5 to 600 MeV at LANSCE/WNR," in *Proceedings of the International Conference on Nuclear Data for Science and Technology*, 402 (1997).
6. S. Meigo *et al*., "Measurements of Neutron Spectra Produced from a Thick Lead Target Bombarded with 0.5- and 1.5-GeV Protons," *Nuclear Instruments and Methods A* **431**, 521 (1999).
7. R.E. Prael and H. Lichtenstein, "User Guide to LCS: the LAHET Code System," Los Alamos National Laboratory report LA-UR-89-3014 (1989).

Proton Radiography

Research Highlights

Overview of Proton Radiography Experiments at LANSCE

F. Merrill, C. Morris (P Division), Proton Radiography Team

The proton radiography (pRad) program at the Los Alamos Neutron Science Center (LANSCE) is investigating weapons-physics issues related to the physics of implosions, hydrodynamics, high explosives (HE), and the dynamic failure properties of materials when explosively driven by HE. Proton radiography provides the unique capability of studying the evolution of explosive processes with high spatial and temporal resolution. With this technique, 800-MeV protons, provided by the LANSCE linear accelerator, penetrate directly through an exploding or imploding system. The protons, delivered in 50- to 100-ns-long pulses, interact with the material of the dynamic system and undergo scattering that is proportional to the product of the density and thickness of the material. The configuration of the materials, which are moving with typical velocities of ~ 1 mm/μs, is effectively "frozen" during the short duration of the proton pulses. These protons are then transported from the object, through a magnetic lens to a Fourier point where protons are intercepted if they were scattered to angles larger than some maximum cutoff. This cutoff angle provides the image contrast, whereby the proton density is lowered for protons passing through thicker materials. The protons surviving the cutoff angle are then magnetically transported to a scintillator located at an image location, where the proton positions are identical to their initial position at the object location. The scintillator converts the proton flux to light, which is collected by a series of fast-gated cameras. The multiple images are separated in time by typically 1 μs for up to 21 pulses per dynamic event and can be combined to produce a "motion-picture" of the dynamic event in which materials travel ~ 1 mm between frames.

pRad Experiments at LANSCE

In 2001, 36 dynamic pRad experiments were performed at LANSCE in support of the weapons-physics efforts at Los Alamos National Laboratory (LANL), Sandia National Laboratories (SNL), Lawrence Livermore National Laboratory (LLNL), and the Aldermaston Weapons Establishment (AWE), bringing the total number of dynamic experiments performed at LANSCE to 114. For these shots, the LANSCE accelerator and beam-delivery complex provided protons with 100% reliability. In addition to these dynamic experiments, beam time was used for detector and concept development and for the radiography of static mock-ups to determine shot configurations and the design of

future experiments. The 36 pRad shots in 2001 fell into three categories: (1) outside-user experiments, (2) HE-driven dynamic studies, and (3) implosion dynamic studies. For outside-user experiments, we hosted SNL for five shots to continue investigations on explosively driven voltage bars, and LLNL for seven dynamic experiments (Fig. 1). HE dynamic shots included further investigations of the formation of dead zones in HE, detonation-wave shapers, and detonation-wave colliders, where two independent detonation waves within the same sample of HE are run against each other (see *Studying the Propagation of Detonation Waves Through Explosive Objects* in this report, p. 98). Experiments were performed to study material dynamics and failure mechanisms, such as spall formation (see *Proton Radiography of High-Explosive Spall in Selected Metals* in this report, p. 102). Experiments were also performed to obtain sheet-jet uniformity measurements and ejecta measurements (see *Combining Cross Correlation and Proton Radiography to Measure Velocity Fields in Explosively Driven Events* in this report, p. 106).

A third in a series of BilliG experiments (BilliG5L) was performed at LANSCE on September 7, 2001, in collaboration with AWE. This experiment required the joint efforts of LANSCE, P, X, ESA, ESH, and DX Division personnel. The chief scientific goals of the


↑ **Fig. 1.** *Installation of a dynamic HE experiment in the 6-ft containment vessel in Area C.*

experiment were to study implosion-related phenomena relevant to the performance of nuclear weapons and to further validate the capabilities of proton beams for radiographic imaging of nuclear-weapons hydrodynamic tests. The results of a Laboratory-Directed Research and Development (LDRD) effort to study dynamic systems at the meso-scale level were used to develop a magnifier system deployed for this BilliG5L shot. This optical magnification provided improved resolution along with a wider dynamic range, resulting in higher-quality radiographs of the imploding system.

The LDRD-sponsored effort to extend pRad capabilities to study dynamic systems with finer resolution also produced the first magnetically magnified dynamic radiographs. In this system, the protons are allowed to expand by a factor of 3.1 by the magnetic lattice while still being in focus. A diagram of the proton trajectories through this system is shown in Fig. 2. This system results in factor of 3 magnification of the

radiographic image at the scintillator. This magnifying system was used to measure the velocity of markers (i.e., embedded gold beads) in shocked materials for SNL and to measure detailed burn-front characteristics in HE by X-5 at LANL.

In addition, a nine-frame framing camera, developed by Bechtel-Nevada, was installed and commissioned in the LANSCE pRad Facility in Area C. This camera, in combination with the 12 single-shot cameras, collected 21 images of the evolving copper sheet jet, which was the last dynamic pRad experiment of 2001. This number of images is a pRad record and sets a new standard in "motion-pictures" for future dynamic experiments at LANSCE.
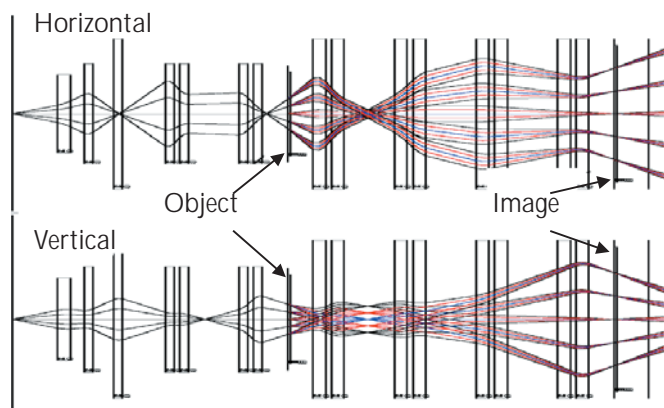
↑ Fig. 2. *Magnifier setup for three-fold magnetic magnification. The colored trajectories correspond with proton trajectories passing through the radiography system. The trajectories at the image location have been allowed to expand by a factor of 3 while maintaining the focus.*

Research Highlights

Studying the Propagation of Detonation Waves Through Explosive Objects

E.N. Ferm, P. Quintana (DX Division), M.P. Hockaday, G.E. Hogan, N.S. King, F.E. Merrill, K.B. Morley, C. Morris, P.D. Pazuchanics, A. Saunders (P Division), J.D. Zumbro (X Division), S. Baker, R.P. Liljestrand, R. Thompson (Bechtel Nevada)

High explosives (HEs) are energetic materials engineered to release their stored energy when a strong pressure shock propagates across the material. Once the energy is released, the pressure built up by the process supports the propagation of the shock wave. The synergistic combination of the shock-wave stimulus and the subsequent support of the shock from the release of energy is called a detonation wave. We conducted a set of explosive experiments using the multiple-frame capability of proton radiography (pRad) to test simple explosive configurations, to explore the kinematic evolution of the detonation waves, and to obtain density measurements from proton beam attenuation. The explosive systems used in our pRad experiments were detonated in a containment system, which is designed to allow the viewing of the proton-transmission image of the experiment at the scintillator location through a magnetic lens system.[1] The containment system is evacuated to reduce blurring. The static image, the beam profile, and the camera dark current along with the dynamic images are used to obtain normalized images of the proton transmission along its path length. All of the images discussed in this research highlight are of exploding objects that are axially symmetric, allowing us to make density measurements at various stages of the dynamic evolution of the system. In these pRad experiments, we are learning what is required to make the best possible measurements of radiographic transmissions. The results of the density and velocity measurements will be compared to computer-calculated codes.

We have performed several detonation-wave-propagation experiments on three configurations— each one with a different regime of the detonation-wave propagation. The first configuration, known as the "rate-stick experiment," is the steady propagation of a detonation wave through a cylindrical charge in which this wave reaches a steady state that only depends on the diameter and material of the charge. The second configuration, the "wave-collider experiment," involves the head-on collision of two detonation waves in which strong shock waves

are reflected back into the explosive products. The third configuration, the "corner-turner experiment," examines the propagation of a steady detonation wave down a small-diameter charge entering a larger-diameter charge. Ultimately, the detonation wave in the larger-diameter charge travels faster than in the small-diameter charge. Upon initial entry into the large charge, however, the wave has insufficient energy support to initiate the explosive, leaving behind a shocked, but mostly unreacted, explosive.

Rate-Stick Experiment

Rate-stick charges are used for the measurement of the steady detonation velocity in cylindrical charges and its variation with charge radius and initial conditions.[2] We have used PBX9501 and PBX9502 rate-stick charges in the pRad 0079 and pRad 0080 experiments. The detonation wave shown in Fig. 1b has already reached steady propagation, having traveled more than 10 cm before the wave had entered the field of view. By measuring the positions of the initial wave front at different times, we found that the detonation wave was propagating at a constant velocity of 8.83 mm/μs. We can make better density estimates of the explosive products by averaging translated images and subsequently reducing the radiographic noise in the images as is shown in Fig 1b. Ultimately, this information will be compared to computer-calculated kinematics of the wave propagation. Also, the experimental density, as obtained from the attenuation of the proton beam, will be compared to the computer-calculated density.

A simplified thermodynamic view of this experiment is shown in Fig. 1c. The initial material state, **O**, is shocked to state **A** on the Hugoniot curve of the unreacted material. (A Hugoniot is the locus of thermodynamic states achievable behind a shock wave from a given initial state **O** without reactions taking place.) The reaction then takes place from state A to state B. From state B, the reaction products expand along what is called the release isentrope in which the hydrodynamic flow proceeds at constant entropy. Although we have no direct measurement of the pressure in this experiment, we can validate the thermodynamic relations used in the calculations by comparing the calculated densities to the experimental ones.

(a)

pRad 5" x 5" field of view

PBX 9501
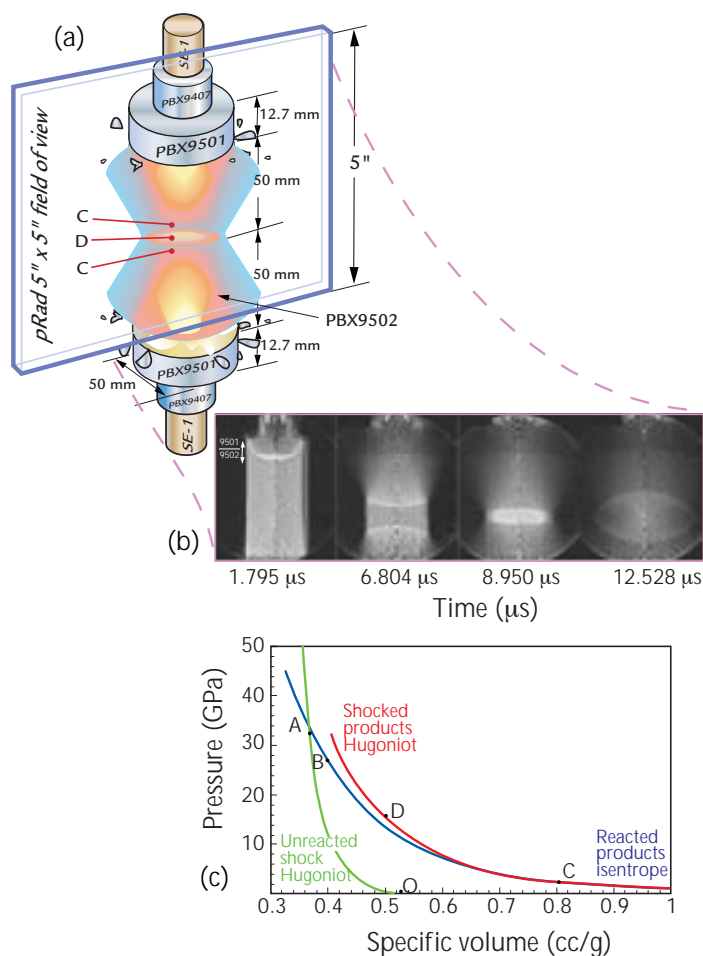
O
A
B

C

SE-1

5"

(b)

(c)
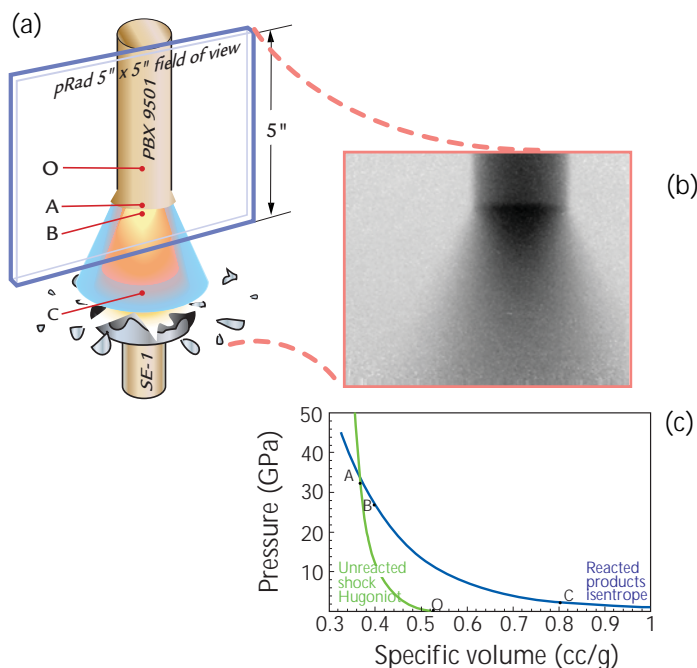
← **Fig. 1.** (a) Artist's rendering of the rate-stick experiment. The SE-1 is a detonator used to initiate the explosive (PBX9501) under study. The PBX9501 cylinder was 8 in. long and 0.5 in. in diameter, although the experiment view encompassed only the last 4.5 in. of the dynamic event. (b) The average of seven translated radiographs results in a sharper image over a limited region. The image darkness is proportional to the length of material the proton beam had to pass through. The dark band propagating along the charge is the detonation wave, and the conical structure that follows is the release of high-pressure reaction products. (c) A simplified thermodynamic view of the pressure-volume processes going on in the rate-stick experiment: initial state material, O, is shocked to state A on the Hugoniot curve, which initiates a reaction that occurs between states A and B. The hot products then expand taking materials to lower density (at C) along the isentrope.

Although the release isentrope reveals much information about the thermodynamics of the reaction products, it is insufficient to specify its equation of state. To describe the products at any accessible pressure and volume, we must determine what happens to them as they deviate from the isentrope. We accomplished this in the wave-collider experiment described in the next section.
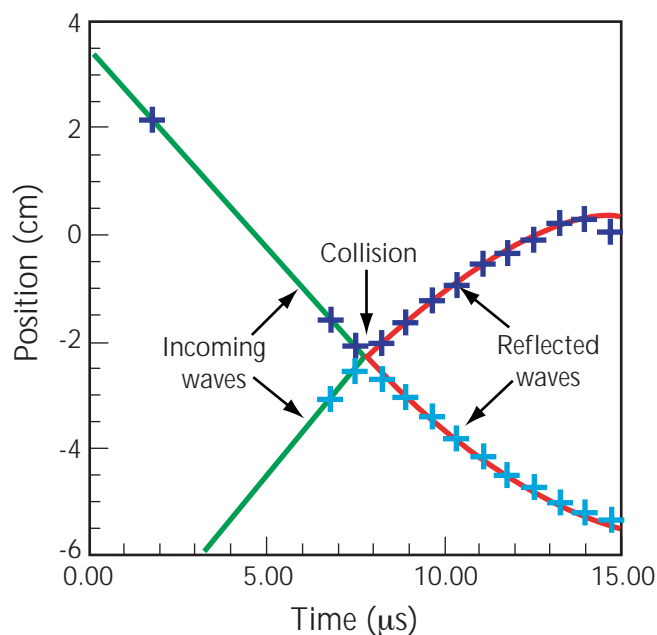
Wave-Collider Experiment

The wave-collider experiment (Fig. 2) allowed us to examine the shocked reaction products at various densities on the release isentrope. In this experiment, we examined one detonation wave in PBX9502 running into an identical detonation wave propagating in the opposite direction. Like the rate-stick experiments, these results are also cylindrically symmetric; however, in this experiment, the speed of the steady detonation wave is not achieved, the wave not having traveled a sufficient number of diameters in length. Furthermore, because the reflected shock waves do not propagate into a uniform

(a)

pRad 5" x 5" field of view

SE-1
PBX9407
PBX9501

12.7 mm
50 mm
5"
50 mm

C
D
C

PBX9502

12.7 mm
50 mm
PBX9501
PBX9407
SE-1

9501
9502

(b)

1.795 µs   6.804 µs   8.950 µs   12.528 µs
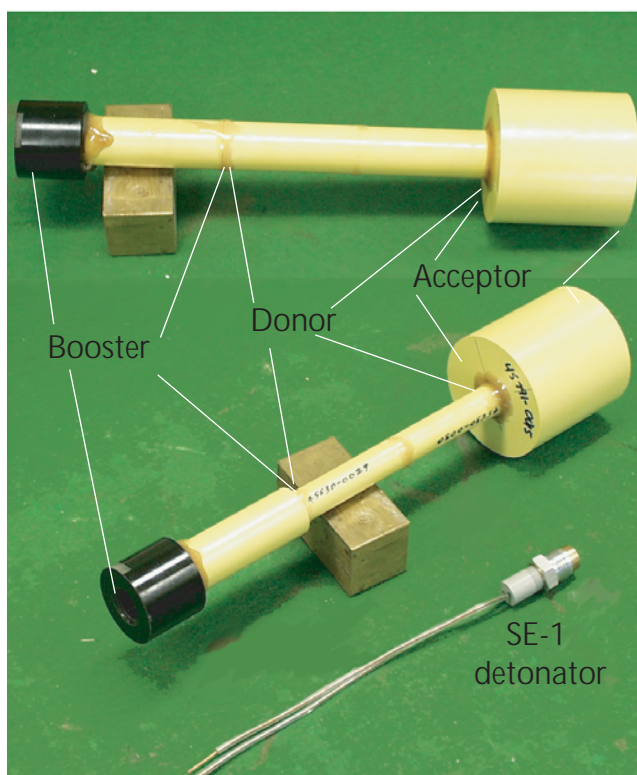
Time (µs)

← **Fig. 2.** (a) Artist's rendering of the wave-collider experiment. The wave collision occurs within the PBX9502 charges. The PBX9501 and PBX9407 charges are booster charges required to efficiently initiate the less-sensitive explosive. (b) Volume-density images found from the radiographs taken of the experiment (assuming that the exploding objects are axially symmetric). (c) Thermodynamic states reached in the wave-collider experiment. State D lies on the shocked products Hugoniot for state C. Each image after the reflection reveals a different pair of C and D states lying on distinct Hugoniot curves.

(c)

↑ **Fig. 3.** *Shock-wave trajectories from the wave-collider experiment. The two incoming shock waves have velocities of 7.2 and 7.4 mm/µs. The reflected shocks rebound out into the products, initially at nearly 7 mm/µs but less than 5 mm/µs after 2 µs.*

↑ **Fig. 4.** *Corner-turning charges made from PBX9502.*

state, their subsequent propagation into the reflected products is not steady state. Four of the analyzed radiographs are shown in Fig. 2b. Assuming that the exploding objects are axially symmetric, our analysis resulted in a measurement of the material density behind the shock waves. In Fig. 3, the leading edge of the detonation wave is examined. The waves approach the center at about 7.3 mm/µs. The shock waves then reflect outward initially at almost 7 mm/µs but then quickly slow down to 5 mm/µs after 2 µs. By the end of the observation, the shock velocity is down to 2 mm/µs. The wave positions plotted in Fig. 3 are measurements made in the experimental frame of reference, so the shock waves that have material movement ahead or behind them may be stronger than the velocity might indicate. The pressure-volume diagram (Fig. 2c) adds a new curve, the *shocked products Hugoniot*, indicating that expanded products at state C are shocked without reactions, thus taking them to a new state D. Initial estimates on shock-wave compressions would indicate about a 15% volume compression in the incoming detonation wave, which takes unreacted explosives from an initial density of 1.9 g/cc (state O) to about 2.2 g/cc (state A) of reaction products. As the wave travels away from the center where the products have been allowed to expand for a longer period of time, the density ahead of the shock is reduced to 0.8 g/cc, and the density behind the shock is reduced to about 1.1 g/cc, or 30% compression at the end of the experiment.

Corner-Turning Experiments

The goal of the PBX9502 corner-turning experiments is to study the initiation and boosting requirements of insensitive explosives. Previous uses of this experiment have identified differences in materials with subtle changes in their microstructures. The experimental configurations in Fig. 4 show two of the charges used for this work. The charges consist of three sections: an initiation/booster charge, a smaller-diameter donor charge, and a larger-diameter acceptor charge. Earlier experiments observed the time of first arrival of the shock along the cylindrical surface of the acceptor charge.[3] With an ideal HE, the detonation wave will reach the outside cylindrical surface at the donor-acceptor plane. The further away the first arrival is from the acceptor donor plane, the more difficulty the donor charge has initiating the acceptor and the less ideal the explosive behaves. In Fig. 5a, the density image shows the detonation wave front having propagated well into the large section of the charge. In our case, the detonation-wave front breaks out at the side of the charge near the point marked "corner-turning distance," thus demonstrating the non-ideal behavior of PBX9502. Also seen in the image is a high-density region in the acceptor, which the detonation wave apparently had to travel around.

(a)

(b)
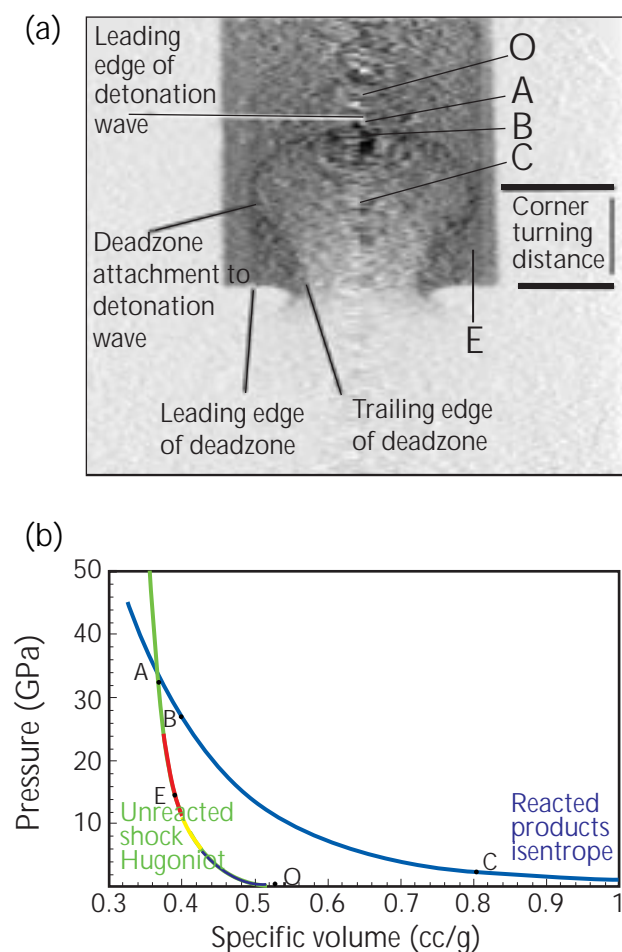
↑ **Fig. 5.** (a) Volume-density image of the 12-mm corner-turner experiment at 25.3 μs. The regions called out in the image identify the deadzone. (b) Representative states in the radiograph have been identified in our thermodynamic pressure-volume description. State E in the deadzone region has not been shocked sufficiently to cause a fast reaction. Material shocked into the red portion of the unreacted shock Hugoniot will accelerate to state A in 0.25 μs to 1.0 μs, assuming a well-supported one-dimensional shock wave. In this case, the support is not sufficient and the reaction falters.

The high-density region is denser than the initial HE material and persists in the later images. This region where the shock is not strong enough to initiate the material is called a deadzone. The leading edge of the deadzone expanded radially at about 3.3 mm/μs, whereas the trailing edge expanded about 0.9 mm/μs. As the wave enters the larger-diameter acceptor charge, the surface area of the detonation wave increases rapidly at the corner, resulting in a pressure drop in the divergent flow. With the lack of support, the detonation wave fails to maintain the reaction resulting in material that is shocked but does not react.[4] In Fig. 5b, we see that two very different regions occur. The first is a successful detonation like in the rate-stick experiment—the shock and reaction move the system from state O to A, then to state B, and finally releases to state C. The second region, the deadzone, is quite different because the divergent flow in the corner cannot support a strong enough shock, resulting in a shock taking the system from state O to state E well below state A and resulting in a region of nearly no reaction.

Conclusion

We have studied three facets of detonation-wave propagation using pRad to examine the kinematic evolution and density distributions of the flow. The rate-stick experiment resulted in a steady detonation wave and the reacted material occurring on the release isentrope. The wave-collider experiment examined fully detonated material off of the release isentrope by reflecting a shock wave back into the products. The corner-turning experiment examined some material shocked so weakly that the reaction failed to proceed. Although simple in configuration, these experiments show the synergistic relations between the release of chemical energy in the explosive and the shock waves, which trigger chemical reaction.

References

1. N.S.P. King *et al.*, "An 800-MeV Proton Radiographic Facility for Dynamic Experiments," *Nuclear Instruments and Methods* **424**, 84-91 (1999).
2. L.G. Hill, J.B. Bdzil, and T.D. Aslam, "Front Curvature Rate Stick Measurements and Detonation Shock Dynamics Calibration for PBX9502 over a Wide Temperature Range," in *Proceedings of the 11th Symposium on Detonation* (1998).
3. M. Cox and A.W. Campbell, "Corner-Turning in TATB," in *Proceedings of the 7th International Symposium on Detonation* (1981).
4. E.N. Ferm, C.L. Morris, J.P. Quintana, P. Pazuchanic, H. Stacy, J.D. Zumbro, G. Hogan, and N.S.P. King, "Proton Radiography Examination of Unburned Regions in PBX9502 Corner-Turning Experiments," in *Proceedings of the 12th American Physics Society Topical Conference on Shock Compression in Condensed Matter* (2001).

Research Highlights

## Proton Radiography of High-Explosive Spall in Selected Metals

D.B. Holtkamp, D.A. Clark, D. Martinez, K.C. Forman, R.A Gallegos, V.H. Holmes, K.B. Morley, P.D. Pazuchanics, A. Saunders, G.E. Hogan, F.E. Merrill, C. Morris, M.M. Murray (P Division), M. Garcia, H.L. Stacy, E.N. Ferm, W.F. Hemsing, K.P. Prestridge, M.A. Shinas, R.P. Lopez, (DX Division), R. Liljestrand, T. Schafer (Bechtel Nevada)

When a pressure wave produced by a high-explosive (HE) detonation reaches the free surface of most metals, two different phenomena can occur: (1) one or more layers of solid material is produced from the fracture of the metal and accelerated "spall" or (2) the metal is melted and accelerated to fairly high velocities (1 to 2 km/s). The detailed understanding of spall phenomena in metals is an active area of research in shock physics but also in materials science and microstructural modeling and is of significant interest to both applied and basic science. We undertook a series of proton radiography (pRad) experiments at the Los Alamos Neutron Science Center (LANSCE) in the summer of 2001 to study HE-induced spall in several metals, including copper, aluminum 6061, tantalum, and tin. These experiments used the pRad Facility in Area C.[1] Analysis of the imagery obtained continues, but several important observations can be deduced from the data: (a) it appears that the pRad technique can produce data on the thickness and velocity of multiple layers of spall (up to 8 layers deep in copper); (b) although the first few layers appear to be quite reproducible, as one goes deeper into the damaged metal the phenomenology becomes "noisier" with a more statistical nature to the layering, at least in this HE/target geometry; and (c) when material is melted on shock, it is readily visible in the proton radiographs (e.g., tin) and information can be obtained on the velocity distribution of the melted material.

Results of the pRad Study

The basic configuration of the experiment is shown in Fig. 1. A 2-in.-diam, 0.5-in.-thick cylinder of HE (PBX9501) is initiated with an SE-1 detonator centered on the charge. Because the HE is point initiated, the shock wave has significant curvature. This "curved" geometry may be advantageous in pRad experiments since the integral of the proton path length is often shorter, and resolution and contrast may be improved, as compared to a pure "planar" geometry. The axial
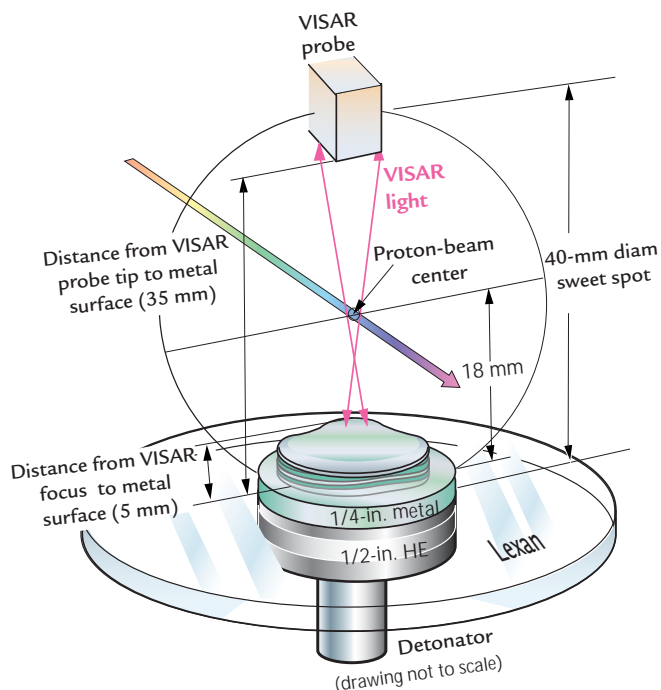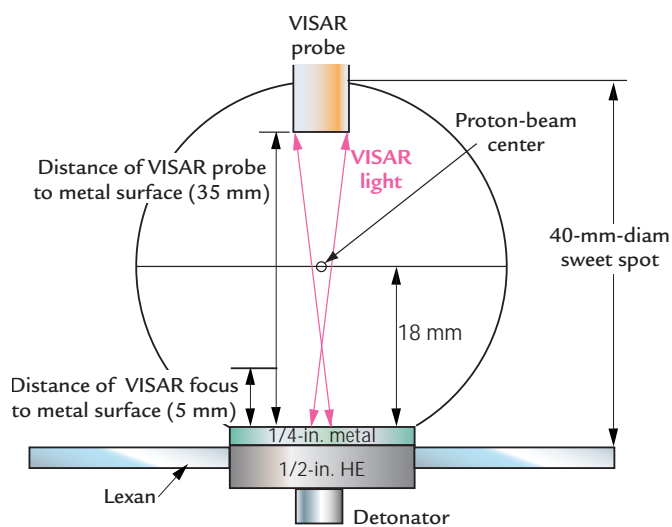

↑ **Fig. 1.** *Schematic and three-dimensional rendering of HE spall experiment.*

symmetry of the experiment is retained, however, which makes other advanced image processing possible (e.g., Abel inversions[2] used to produce "volume" density images). A velocity laser interferometer (VISAR) is also used to measure the time history of the surface during the experiment. Excellent agreement between VISAR and radiography results was obtained in all experiments to date. The "shutter time" of these proton radiographs is determined by the pulse width of protons that are used to produce each image frame. In these cases, the pulse width was typically ~ 50 ns, a short enough time to produce minimal motion blur ($\approx$ 100 μm) even for the highest material velocity (aluminum at ~ 2 km/s).

Fig. 2 shows a series of 16 images of tantalum spall. This material has one of the highest spall strength of any material (~ 50 kbars). Spall strength is a measure of the strength of a tensile wave (in kbars) needed for the material to separate into layers. This strength is reflected in the exceptionally well-defined layers (and the small number of layers) visible. The times in Fig. 2 are relative to the time the detonator is initiated with a "fire" pulse. Note the curvature of the spall material and the complete separation of the material into layers. This can be observed even more vividly in "movies" produced from the 16 images.

Copper provides an example of a material with an intermediate spall strength (~ 15 kbars). Fig. 3 shows a single image from two separate experiments at a comparable time (33.4 μs) after HE initiation. These images have been Abel[2] inverted to produce "volume" density images. Multiple spall layers are evident with the best-defined layers nearest the metal surface. As many as eight distinct layers are present in these images with defined velocities, although the layers become more "noisy," or chaotic, as one views deeper into the metal sample. It appears in Fig. 3 that the first few layers tear away smoothly as compared to the deeper layers. The more layers that tear away, the rougher, or "noisier" the spall phenomena becomes—a phenomenology we hope to one day understand. It is worth noting that these images, taken at nearly identical times, show quite good reproducibility, at least on the outermost layers. The VISAR optical probe is visible near the top of the frames.

Fig. 4 shows a similar pair of experiments for aluminum 6061 at 19.0 μs. Because the atomic number of aluminum is low, the resolution and contrast of the radiographs are improved as compared to the copper and tantalum targets. Note the details of the VISAR optical probe that are visible in Fig. 4. The spall
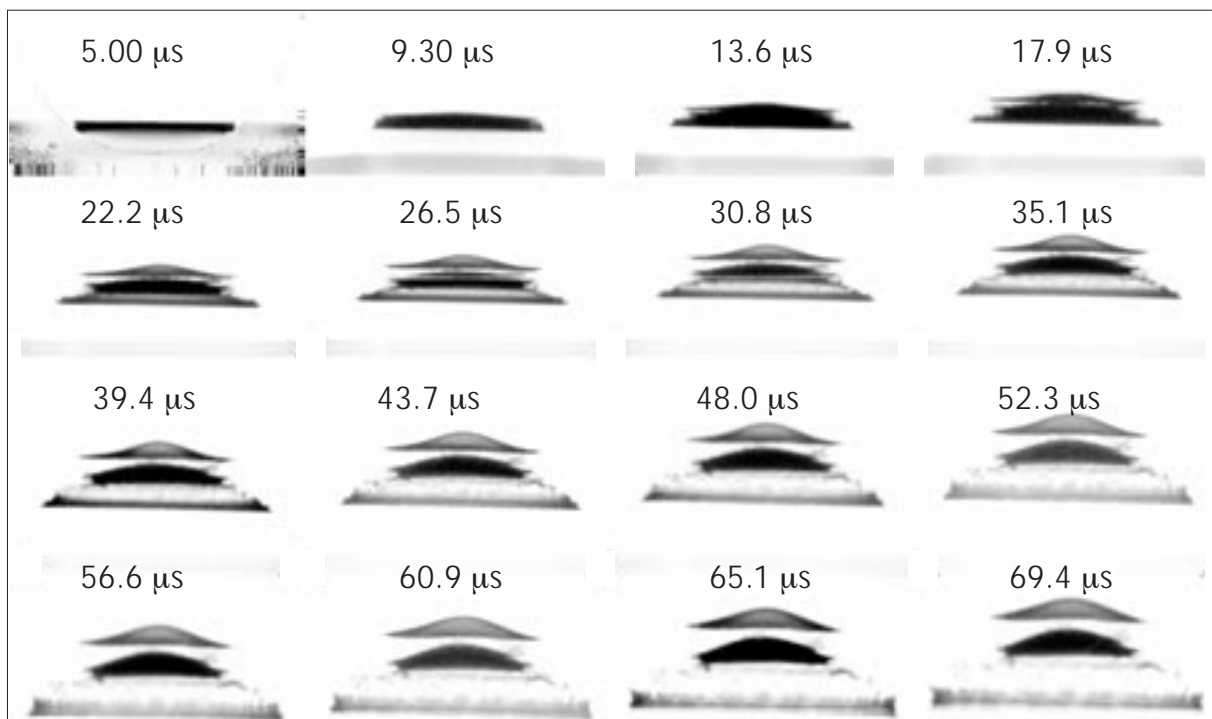
↑ Fig. 2. *Proton radiography images of HE-driven tantalum spall (areal densities), showing the evolution of the spall beginning with the top static image on the left and progressing to the right and down.*

VISAR

Noisy, chaotic phenomena
deeper within the sample

Distinct initial layers
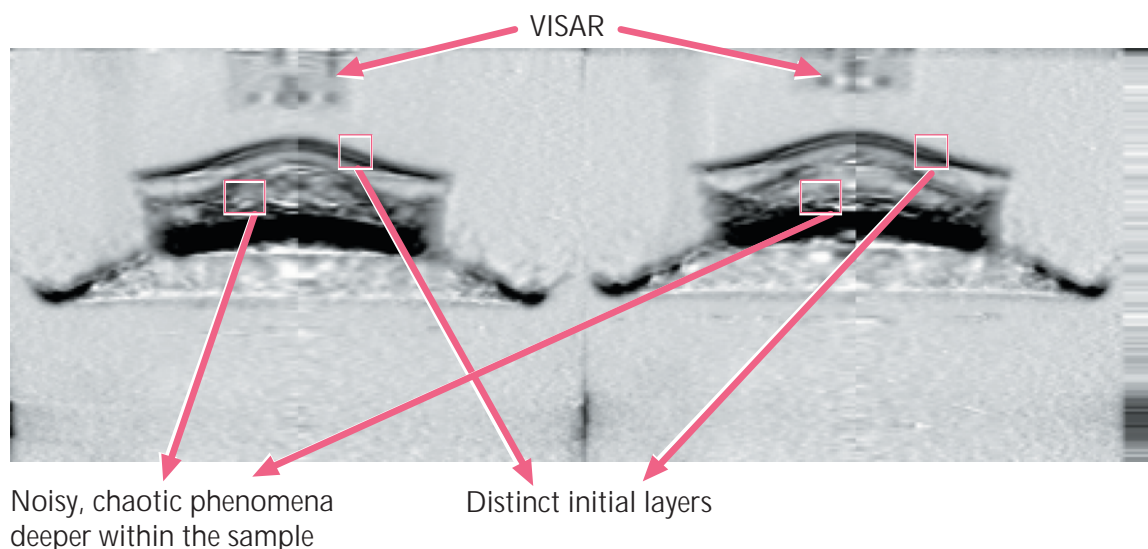
↑ **Fig. 3.** *Abel-inverted "volume" images of copper spall from two separate pRad experiments at 33.4 μs. The VISAR optical probe, seen near the top of each frame, tracks the surface velocity of the first spall layer as it moves in response to the HE-induced shock wave.*
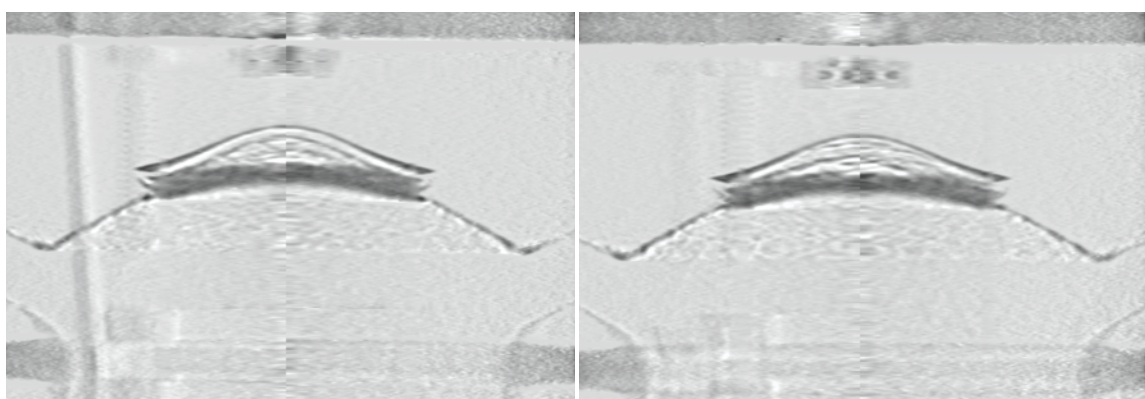
↑ **Fig. 4.** *Abel-inverted images of aluminum 6061 spall from two separate experiments at 19.0 μs after HE initiation.*

phenomenology in aluminum, however, is not as well behaved as in copper. The "turbulent" character of the deeper spall layers is visible after the first spall layer.

When the shock pressure is high, the material is melted after the shock wave reflects from the free surface of the metal target. Fig. 5 shows two frames at different times from an experiment on tin with the same HE configuration as the other experiments. The left-hand frame (at 19.3 μs) shows both ejecta produced when the shock reaches the metal surface. In the central region, the metal is melted (liquefied) upon the release and subsequent reflection of the shock wave at the surface, which appears more dramatically in the later image on the right (at 42.2 μs). The velocity of the melted material is substantially higher than the solid

remnant left behind. This produces the dispersion of material observed.

Conclusion

Further analysis of these (and other) experiments is continuing. Our analysis is concentrating on how well we can measure the velocities, thickness, and other parameters of multiple spall layers with pRad and compare these results to both two-dimensional calculations and other non-radiographic spall diagnostics, such as the Assay Window.[3] We plan future experiments using higher magnification of the radiography to explore finer resolution details of the HE spall phenomenology.
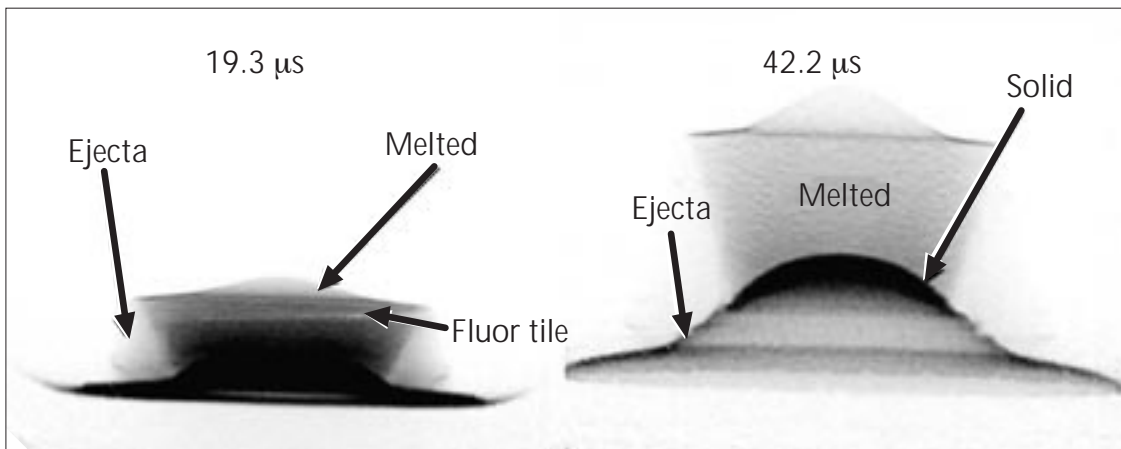
↑ Fig. 5. *Proton radiography images of shock-melted tin at 19.3 μs (left) and 42.2 μs (right); an artifact of the tiled fluor appears at the same image location in both.*

References

1. K.B. Morley *et al.*, "Proof-of-Principle Demonstration of Proton Radiography on a Dynamic Object," in *Proceedings of the 11th Biennial Nuclear Explosives Design Physics Conference* (1997); Los Alamos National Laboratory report LA-CP-98-6; and H.-J. Ziock *et al.*, "Using Proton Beams as a Radiographic Probe," Los Alamos National Laboratory report LA-UR-98-2660.
2. C. Morris, private communication (2001).
3. D.B. Holtkamp and W.F. Hemsing, "The Assay Window: Development of a Non-Radiographic Spall Diagnostic," (to be published).

Research Highlights

Combining Cross Correlation and Proton Radiography to Measure Velocity Fields in Explosively Driven Events

K.P. Prestridge (DX Division)

Proton radiography (pRad) is a technique whereby high-energy protons impinge directly on an object that is either imploding or exploding, interact with the material, and are scattered. Protons that exit the material strike a scintillator, which serves as a proton-to-light converter. Images can be taken very quickly at different time intervals to record the motion of the moving components and features. The pulse structure of the proton beam can be tailored to provide many frames (snapshots) to view a dynamic event and thereby produce a kind of "motion picture" of the event over time. The development of pRad at the Los Alamos Neutron Scattering Center (LANSCE) with its multiple-imaging capability has allowed us to adapt a cross-correlation technique, known as particle image velocimetry (PIV), to radiography. PIV tracks the trajectory of particles and other features and compares them from one snapshot to the other to determine an accurate velocity field. Measuring these velocities can provide experimenters with important data needed to validate codes and models for the Stockpile Stewardship program.

The PIV technique that we adapted for our experiments at LANSCE had been used for more than a decade to measure the two-dimensional (2-D) velocity fields of "low-speed" flows[1] (typically 10m/s). This same technique had recently been used in high-speed shock-accelerated fluid instability[2,3] experiments that required multiple images to determine the displacement of particles or other features in a flow field over time. Our goal is to develop a velocimetry diagnostic that combines PIV with pRad techniques to accurately measure two-dimensional velocity fields in explosively driven dynamic events. In pursuit of this goal, we have performed parallel sets of experiments designed to test the cross-correlation technique on pRad images of an explosively driven silver-liner jet of molten metal and of ejecta (i.e., metal ejected from the far side of a shocked metal surface) from tin and aluminum disks.
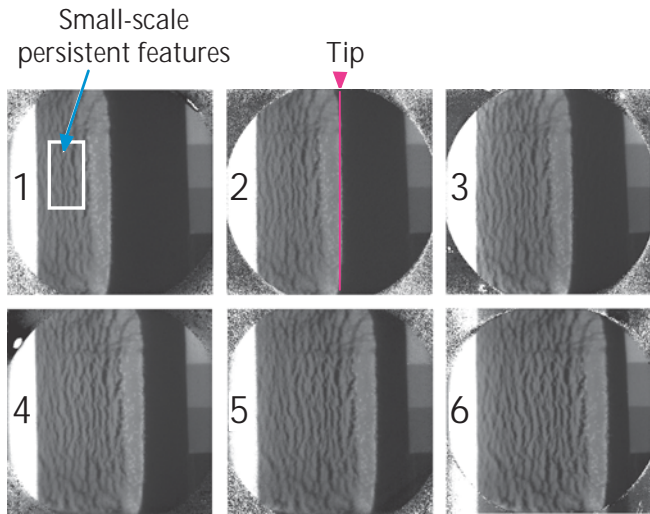
Silver-Liner Experiment

The silver-liner experiment, shown in Fig. 1, provides multiple images of a 2-D sheet of silver. The sheet is created by the geometry of the explosives and the location of the detonator. The explosive, PBX9501, is a

shaped charge in the form of a wedge (Fig. 1), and a thin layer of silver is applied to the inside of the wedge. The explosive is detonated using a line detonator, which keeps the shock wave moving through the silver uniformly across the wedge. The silver in the inner part of the wedge is ejected out of the wedge in the direction shown by the blue arrows in Fig. 1. Fig. 2 shows the images taken using pRad. The approximate field of view of the images is shown as the boxed area in Fig. 1. As the silver sheet jet is formed by the wedge-shaped charge, it is not completely uniform, and this non-uniformity creates small-scale, persistent features in the sheet that can be tracked from frame to frame.
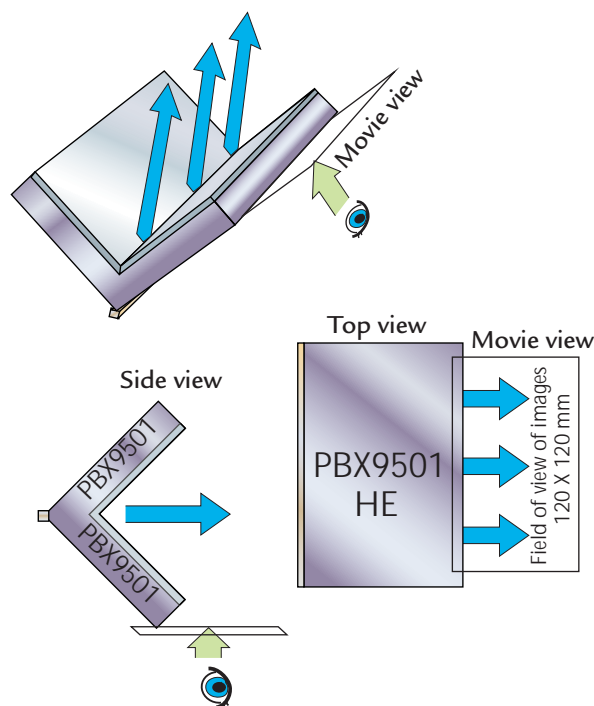
↑ **Fig. 1.** *Side and top view of silver-liner shot setup. The boxed area indicates the field of view of each image in Fig. 2 (which is 120 x 120 mm).*

Cross-correlation techniques can track the trajectory of particles or other persistent features (as shown in Fig. 2). The particles may be embedded tracers or may be produced by the experiment itself. The key is to make sure that the features you are tracking are smaller than the scales of the flow that you wish to measure. Many features are required to correlate between the two images, and each correlation only provides one velocity vector. Therefore, the more small-scale features there are, the denser the vector field will be. In the case

Small-scale
persistent features   Tip

↑ Fig. 2. *Sequence of six images of silver jet using pRad. The time between images is 2.147 μs.*

of the silver-liner experiment, the features in the liner were small enough to obtain a dozen velocity vectors across the sheet. Fig. 3a shows the velocities calculated from cross correlation of images 5 and 6 in Fig. 2. To interpret the accuracy of these velocities, we averaged the vector magnitudes at each *x* (downstream) location; the results (PIV data) are plotted in Fig. 3b using blue tri-angles. You can see from the experiment that the velocity of the sheet increases as one moves downstream towards the tip of the sheet. Across the tip of the sheet (the nar-rower, lighter region) the velocity is constant. The meas-ured tip velocity was 3.0 mm/μs. We compared the experimental results to those done using MESA, a 2-D Eulerian hydrodynamics code, which uses the geometry of the material in the experiment to simulate the detonation of the HE and the propagation of the shock wave through the material. The velocities calculated by MESA are shown in red circles on Fig. 3b. The increase in velocity across the sheet and the leveling off at the tip are confirmed by the calculation. The only difference between calcu-lation and experiment was that the calculation overpredicted the tip velocity to be 3.3 mm/μs. The results of using cross-correlation techniques on the silver-liner experiment show that persistent features in radiographs can be used to determine velocity fields. Using this technique allows us to

determine 2-D velocity fields of flows of materials that cannot be viewed with visible light. The results demon-strate a new standard for code validation because we now have far more confidence in the calculation by virtue of the 2-D velocity data.
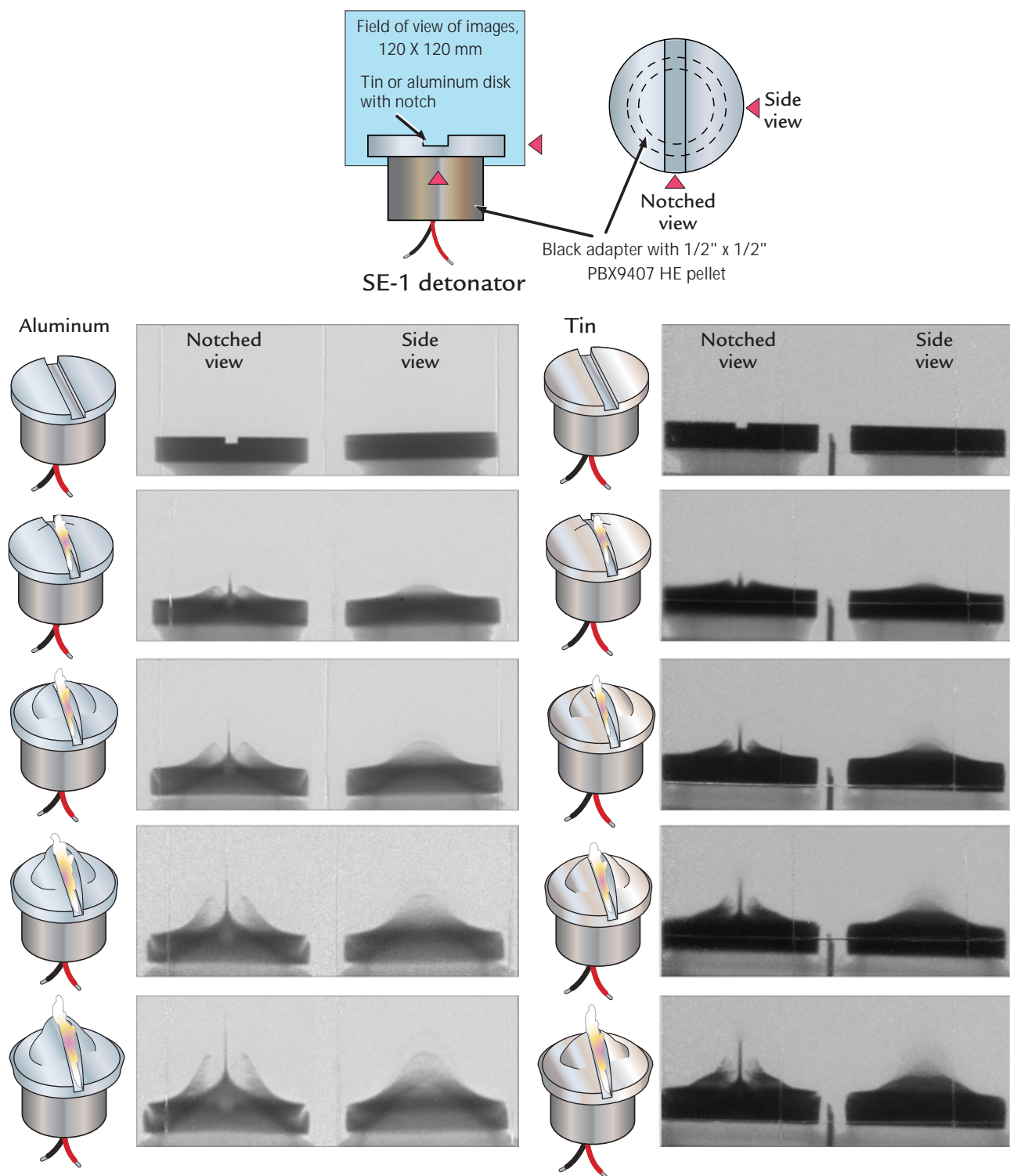
Ejecta Experiments

Our current experiments are designed to develop the cross-correlation technique for studying ejecta. Ejecta are small particles of metal that are ejected from the far side of a shocked metal surface. Fig. 4 shows a three-dimensional rendering and the actual images of the metal disks in our ejecta experiments. They have been performed at Area C, using both aluminum and tin as the disk material. A notch is cut into the 0.25-in.-thick, 1.5-in.-diam disks to ensure reproducibility of the loca-tion of the ejecta particles. In both sets of experiments, the notches were 0.125 in. wide by 0.062 in. deep. A pellet of PBX9407 explosive was used to create the shock wave to drive the metal, and the explosive was initiated using an SE-1 detonator.

Ejecta experiments were performed using pRad. The 120- x 120-mm field of view of the experiments is shown in the light blue boxed area in Fig. 4. The top images are the static images, which show the orienta-tion of the aluminum (left) and tin (right) disks. When the explosive is detonated, a curved shock propagates through the disks, moving from the bottom to the top of the image. This causes metal particles to fly off of the disk. The cloud of particles can be seen fairly well when observed along the notch, since there is more material in this direction. It is more difficult to see the
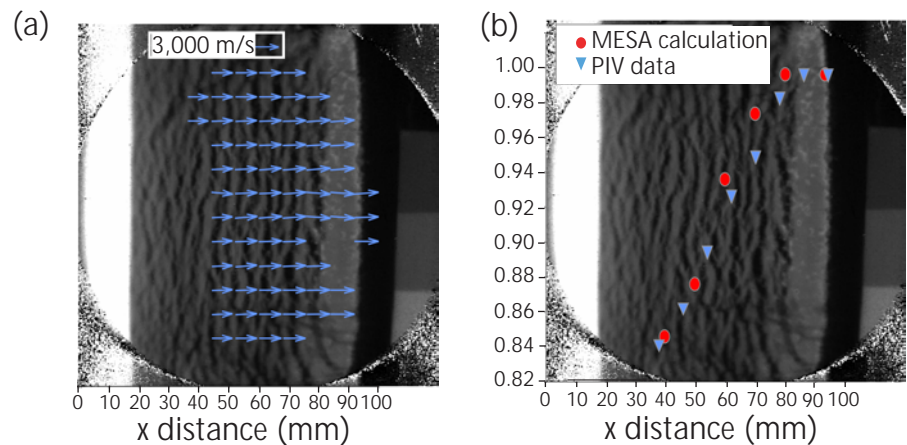
↑ Fig. 3. *(a) Velocity field measured using PIV cross correlation between images 5 and 6 in Fig. 2. (b) Compari-son of average velocity at each downstream (x) location from the experiment and from a MESA calculation (cal-culation courtesy of Eric Ferm, DX-3).*

Field of view of images, 120 X 120 mm

Tin or aluminum disk with notch

Side view

Notched view

Black adapter with 1/2" x 1/2" PBX9407 HE pellet

SE-1 detonator

Aluminum

Notched view

Side view

Tin

Notched view

Side view

↑ **Fig. 4.** *Three-dimensional rendering and actual images of metal disks in the ejecta experiments. The light blue area shows the 120- x 120-mm field of view of the images. Aluminum disks (left) and tin disks (right) are in a time sequence (with a separation between images of 2.14 μs) from top to bottom, starting with the static images.*

edge of the ejecta cloud from the side. Using edge-detection techniques, we determined that the velocity of the edge of the aluminum ejecta cloud is 2.2 mm/μs at late time, whereas the velocity of the tin ejecta cloud is 2.8 mm/μs at late time.

In these experiments, we were unable to resolve the particles inside the ejecta cloud due to limitations of the spatial resolution of pRad to approximately 100 μm per pixel. The particles are approximately 10 μm in diameter. More sets of experiments are being performed in indoor firing chambers to determine how to visualize the ejecta particles so that cross-correlation techniques can be used to determine 2-D particle velocity fields.

Conclusion

We demonstrate a new standard in code validation by performing cross-correlation techniques on pRad images from a silver-liner experiment to determine the velocity field of the liner in a 2-D plane. These correlations reveal velocities up to 3 mm/μs at the leading edge of the liner, and they agree well with numerical predictions of the velocity distribution across the liner. Experiments are currently being designed to employ the cross-correlation technique to ejecta experiments. The experiments will have to be designed so that the small particles can be resolved well enough to provide a pattern for correlation. This work is currently in progress, and we have performed experiments with both tin and aluminum to determine an optimal configuration for studying ejecta transport using the multiple imaging capabilities of pRad.

References

1. R.J. Adrian, "Particle-Imaging Techniques for Experimental Fluid Mechanics," *Annual Review of Fluid Mechanics* **23**, 261 (1991).
2. K.P. Prestridge, P.M. Rightley, P. Vorobieff, R.F. Benjamin, and N.A. Kurnit, "Simultaneous Density Field Visualization and PIV of a Shock-Accelerated Gas Curtain," *Experiments in Fluids* **29**, 339 (2000).
3. K.P. Prestridge, P. Vorobieff, P.M. Rightley, and R.F. Benjamin, "Validation of an Instability Growth Model Using Particle Image Velocimetry Measurements," *Physical Review Letters* **84:19**, 4353 (2000).